[a4]report

Master Thesis

Ring Imaging Cerenkov Counter with Aerogel Radiator for HERMES

Department of Physics
Tokyo Institute of Technology

LinFeng Zhang

February 9, 1999

Abstract

The HERMES experiment is designed to study the spin structure of the nucleon. It is unique among contemporary experimental studies of the spin structure because it can measure pion, kaon and proton and determine semi-inlusive spin asymmetries.

In the past, HERMES used a threshold Cerenkov counter as one of its four particle identification detectors. In order to enhance the particle identification capability, HERMES replaced the threshold Cerenkov counter with a Ring Imaging Cerenkov system(RICH) in 1998, so that it can separate π, k, p in all the HERMES engergy region: 2 GeV to 20 GeV.

The new RICH system uses aerogel and C_4F_{10} gas as its Cerenkov radiator. The refractive index and other properties of all the aerogel tiles were measured at Tokyo Institute of Technology. The new RICH detector has successfully produced rings from Cerenkov photons on a large array of small diameter phototubes.

In order to study the new RICH system, Monte Carlo has been carried out, and has been obtained a satisfatory result comparing with the experiment data.

This thesis describes the new RICH system, in particular the measurement of the aerogel tiles and the Monte Carlo taking aerogel tile effect on the Cerenkov angle into account.

Contents

List of Figures

List of Tables

1 Introduction

We know that there exists four fundamental forces which are called strong and weak interaction, electromagnetism and gravitation. Weak interaction and electromagnetism can be described by the electro-weak theory. Strong interaction is described with the Quantum ChromoDynamics(QCD). Among these four interactions, the strong interaction is not well understood mainly because the gluon field with color is difficult to describe in a perturbative way. However, at large momentum transfer, the perturbative mothed has had some success. It is important to perform experiments of large momentum transfer and establish the perturbative approach of QCD. It will then help also to understand QCD in non-perturbative region.

One of the basic questions of QCD is how spin of the nucleon is built up from its constituents. EMC experiment by using polarized leptons and nucleon targets showed that the quark spin contribution to the nuclean spin is small(so called proton spin crisis)[EMC88]. There is no model or theory yet which describe it satisfactorily. Several experiments are being carried out now in order to solve this problem.

One of these experiments is HERMES which has been designed to meaure the spin structure of nucleon with a high precision and statistics. The HERMES detector is located in DEAY-HERA. HERMES uses two advanced technologies for the experiment:

- A polarised electron storage ring.
- Plarised internal gas targets in a windowless storage cell.

Compared to an ordinary free gas jet target, HERMES has a high density gas target of H, D and ^{3}He. One of the merits of HERMES experiment is that it can detect the generated hadrons together with the scattered electron. One of the Particle Identification Detectors(PID) used in HERMES experiment is a threshold Cerenkov Counter using the principle that if a particle with its speed larger than the light velocity in a radiator emits Cerenkov photons.

In order to enhance the particle identification capability, HERMES has converted its old threshold Cerenkov Counter to a Ring Imaging Cerenkov counter (RICH). The RICH is designed to separate π, k and p in the whole HERMES engery region (2 to

20GeV).

The RICH uses Aerogel and C_4F_{10} as its dual radiator. The refractive index is 1.030 and 1.0014 respectively. With the present technology, it is not possible to produce aerogel of such a large area ($200 \times 50 \times 5\text{cm}^3$). It is commercially possible to produce the aerogel tile with its dimesion about $10 \times 100 \times 100\text{mm}^3$. HERMES RICH thus uses totally 850 aerogle tiles. The RICH has successfully generated a ring with the actual beam in 1998.

These aerogel tiles used for HERMES RICH were produced by Matsushita Electric Works, Japan. From 1997 Nov to 1998 Mar, we measured the properties of all these aerogel tiles and shipped them to DESY for the installation. The second part of work in my graduate course is Monte Carlo simulation of RICH. I have simulated the aerogel radiator taking into the properties of the aerogel tiles measured by myself.

This thesis will focus on the measurement of the aerogel tiles and the HERMES Monte Carlo for the new RICH system.

2 Physics of polarized Deep Inelastic Scattering

In this chapter, a brief description on inclusive and semi-inclusive measurements of the deep inelastic scattering is given.

2.1 Inclusive measurement of deep-inelastic scattering

In a nuclear reaction, if the number or types of the particles in the final state are not the same as in the initial state, it is called inelastic scattering. If the number and type are the same, it is called elastic scattering.
In inclusive measurement, we detect only the scattered lepton:

$$\vec{l} + \vec{N} \rightarrow l' + X. \tag{2.1}$$

where $\vec{l}$ stands for lepton, and $\vec{N}$ stands for the nucleon.

2.1.1 Kinematics of Deep-Inelastic Scattering

A deep inelastic scattering process of the nucleon is shown in Fig2.1. The negative squared four-momentum transfer is defined as

$$\begin{aligned} Q^2 &= -q^2 = -(k-k')^2 \\ &\overset{\text{lab}}{=} 4EE' \sin^2\theta/2, \end{aligned} \tag{2.2}$$

where k and k' are the vector of the lepton before and after the scattering. q is the four-momentum of the virtual photon. θ is the scattering angle. E and E' are the engery of lepton before and after the scattering.

In the lab system the absolute and fractional energy transfers of the lepton, ν and

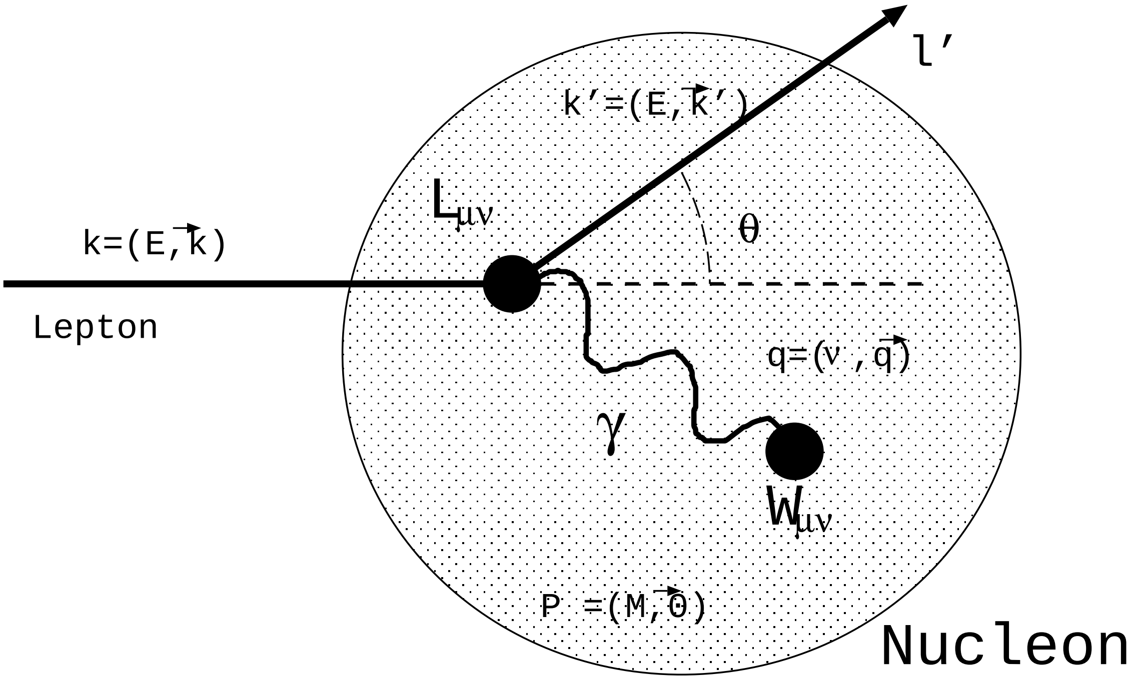

Figure 2.1: Schematic view of an inclusive measurement of Deep Inclusive Scattering (DIS) process.

y, are expressed as

$$\nu = \frac{Pq}{\sqrt{P^2}} \overset{\text{lab}}{=} E - E' \tag{2.3}$$

and

$$y = \frac{Pq}{Pk} = \nu/E \tag{2.4}$$

The invariant mass W of the nucleon fragments is

$$W^2 = (P+q)^2 \overset{\text{lab}}{=} M^2 + 2M\nu - Q^2, \tag{2.5}$$

where $M = \sqrt{P^2}$ is the rest mass of the nucleon.
The Bjorken's scaling variable

$$x = -\frac{q^2}{2Pq} \overset{\text{lab}}{=} \frac{Q^2}{2M\nu} \tag{2.6}$$

is a measure for the inelasticity of the scattering process: for $x = 1$ the squared invariant mass of the nucleon fragments W^2 equals the squared nucleon mass M^2. When $W \geq 2$ GeV, and $Q^2 \geq 1(\text{GeV/c})^2$, the scattering is usually called deep inelastic scattering.[NSa93]

2.1.2 Cross section

In the lowest order Quantum Electrodynamics(QED), the double differential cross section for scattering can be expressed as

$$\frac{d^2\sigma}{dQ^2 d\nu} = \frac{4\pi\alpha^2}{Q^4 E^2} L_{\mu\nu} W^{\mu\nu} \tag{2.7}$$

where $L_{\mu\nu}$ is the leptonic tensor, $W_{\mu\nu}$ is the hadronic tensor, and $\alpha \approx \frac{1}{137}$ is the electromagnetic coupling constant. They are expressed as

$$\begin{aligned} L^{\mu\nu} &= 2(k_i^\mu k_f^\nu + k_f^\mu k_i^\nu - k_i \cdot k_f g^{\mu\nu} - i\epsilon^{\mu\nu\alpha\beta} q_\alpha S_{l\beta}) & (2.8) \\ W_{\mu\nu} &= (-g_{\mu\nu} + \frac{q_\mu q_\nu}{q^2}) W_1(q^2,\nu) + [(p_{i\mu} - \frac{p_i \cdot q}{q^2} q_\mu)(p_{i\nu} - \frac{p_i \cdot q}{q^2} q_\nu)] \frac{W_2(q^2,\nu)}{M^2} \\ &+ i\epsilon_{\mu\nu\alpha\beta} q^\alpha M S_h^\beta G_1(q^2,\nu) + i\epsilon_{\mu\nu\alpha\beta} q^\alpha [(p_i \cdot q) S_h^\beta - (S_h \cdot q) p_i^\beta] \frac{G_2(q^2,\nu}{M} & (2.9) \end{aligned}$$

where S_h is the polarised vector of the spin 1/2 particle. W is the unpolarised part and G is the polarised part.

If we neglect the contribution of weak currents, the leptonic tensor $L_{\mu\nu}$ describes the coupling of the intermediate photon to the point-like lepton. The hadronic tensor $W_{\mu\nu}$ describes the spatially extended nucleon. Requring Lorentz invariance, parity conservation(for non-weak processes), and invariance under time reversal, an expression of $W_{\mu\nu}$ in terms of scalar structure functions is obtained. The cross section (eq2.7) is then expressed as:

$$\frac{d^2\sigma}{dx dQ^2}(x,Q^2) = \frac{4\pi\alpha^2}{xQ^4}(xy^2 F_1(x,Q^2) + (1 - y - \frac{xyM}{s}) F_2(x,Q^2)), \tag{2.10}$$

where

$$\begin{aligned} F_1(x,Q^2) &= MW_1(Q^2,\nu) & (2.11) \\ F_2(x,Q^2) &= \nu W_2(Q^2,\nu) & (2.12) \end{aligned}$$

are the dimensionless structure functions of the nucleon.

We define the function $R(x,Q^2)$:

$$R(x,Q^2) = (1+\gamma^2)\frac{F_2(x,Q^2}{2xF_1(x,Q^2} - 1, \tag{2.13}$$

where γ^2 is the kinematical factor defined by

$$\gamma^2 = \frac{Q^2}{\nu^2} = \frac{4M^2x^2}{Q^2}. \tag{2.14}$$

In the Bjorken limit, γ^2 becomes zero. $R(x,Q^2)$ is interpreted as the ratio of the absorption cross section of longitudinally (σ_L) and transversely (σ_T) polarised virtual photons by the nucleon:

$$\begin{aligned} R(x,Q^2) &= \frac{\sigma_L}{\sigma_T}, \\ \sigma &= \Gamma_T(\sigma_T + \varepsilon\sigma_L), \end{aligned} \tag{2.15}$$

where σ is the total cross section, Γ_T is the total flux of transversely polarised virtual photons and ε is the ratio of probabilitites that the lepton emits a longitudinally or transversely polarised photon (which is calculable in QED):

$$\begin{aligned} \varepsilon &= \frac{\Gamma_L}{\Gamma_T} \\ &= \frac{1-y}{1-y+\frac{1}{2}y^2}, \end{aligned} \tag{2.16}$$

$$\tag{2.17}$$

2.1.3 Polarised Deep-Inelastic Scattering

Fig.2.2 shows angles of the polarised scattering process. Besides the scattering angle θ the angle between the direction of the target polarization $\vec{S}$ and the incident electron beam $\vec{k}$ is named α while φ denotes the angle between the scattering plane and the target polarization. The cross section difference for right- and left-handed incident leptons can then be calculated as

$$\begin{aligned} &\frac{d^3\sigma(\alpha) - d^3\sigma(\alpha+180)}{dx\,dy\,d\varphi} = \\ &\frac{e^4}{4\pi^2Q^2}\{[(1-\frac{y}{2}-\frac{y^2}{4}\gamma^2)g_1(x,Q^2) - \frac{y}{2}\gamma^2 g_2(x,Q^2)]\cos\alpha \\ &-\sqrt{\gamma^2(1-y-\frac{y^2}{4}\gamma^2}[\frac{y}{2}g_1(x,Q^2) + g_2(x,Q^2)]\sin\alpha\cos\varphi\} \end{aligned} \tag{2.18}$$

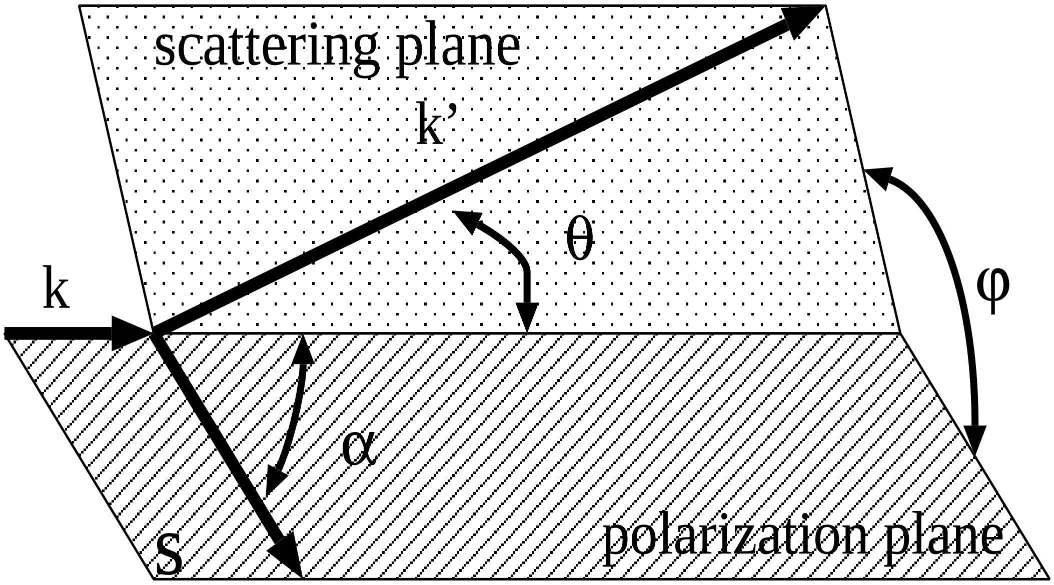

Figure 2.2: Definition of scattering angles in polarised DIS.

where $g_{1/2}(x, Q^2)$ are the structure functions.

2.1.4 Determination of g_1, g_2

The spin structure functions can be determined experimentally by measuring the cross sections of the scattered leptons. The structure functions scale like:

$$M^2 \nu G_1(Q^2, \nu) \rightarrow g_1(x)$$
$$M \nu^2 G_2(Q^2, \nu) \rightarrow g_2(x)$$

when $\nu \rightarrow \infty$ and $Q^2 \rightarrow \infty$.

In Quark Parton Model, the quark distribution function $q(x)$ and quark spin distribution function $\Delta q(x)$ are written as

$$\begin{aligned} q(x) &= q^+(x) + q^-(x), \\ \Delta q(x) &= q^+(x) - q^-(x); \end{aligned} \tag{2.19}$$

where $q^{+(-)}(x)$ is the density of quarks with flavour q and momentum fraction x with the helicity parallel(anti-parallel) to the nucleon spin.

For high Q^2 and ν, the structure function $g_1(x)$ can be

$$g_1(x) = \frac{1}{2}\sum_q (e_q^2 \Delta q(x)) \tag{2.20}$$

while $\Delta q(x) = q^+(x) - q^-(x)$. By using the ^{3}He and H target, HERMES has measured $g_1^n(x)$ and $g_1^p(x)$.

2.2 Semi-Inclusive Measurement of deep-inelastic scattering

Semi-inclusive measurement of DIS reaction is expressed as

$$\vec{l} + \vec{N} \to l' + h + X, \tag{2.21}$$

We can see a new part, h, appears in the final state together with the scattered lepton l'.

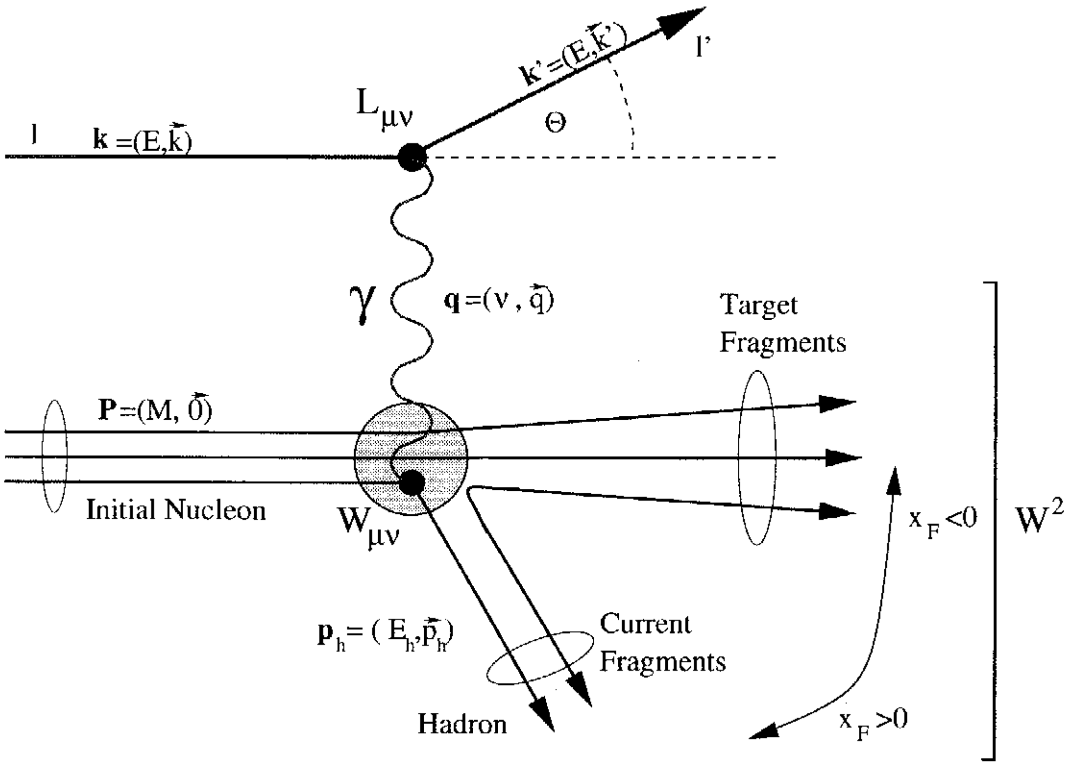

Figure 2.3: Schematic view of a semi-inclusive measurement of DIS process

2.2.1 Cross section

Fig2.3 shows the semi-inclusive measurement of DIS process. The cross-section of the semi-inclusive measurement with a hadron h in the final state is given by

$$\frac{d^3\sigma_h}{dxdQ^2dz}(x,Q^2,z) = \frac{\sum_q e_q^2 q(x) D_q^h(z)}{\sum_q e_q^2 q(x)} \cdot \frac{d^2\sigma}{dxdQ^2}(x,Q^2) = C(x,Q^2)\cdot \sum_q e_q^2 q(x) D_q^h(z); \tag{2.22}$$

where $D_q^h(z)$ is the fragmentation function defined as the number density to produce a hadron with the energy $z \overset{\text{lab}}{=} E_h/\nu$ after a quark of flavour q was struck.

The number of types of fragmentation functions $D_q^h(z)$ can be reduced significantly by applying of iso-spin and charge symmetry. In this approximation only three functions are necessary to parameterize the generation of pions, for example:

$$D^-(z) = D_d^{\pi^+}(z) = D_u^{\pi^-}(z) = D_{\bar{u}}^{\pi^+} = D_{\bar{d}}^{\pi^-}(z), \tag{2.23}$$

$$\begin{aligned} D^+(z) &= D_u^{\pi^+}(z) = D_d^{\pi^-}(z) = D_{\bar{d}}^{\pi^+} = D_{\bar{u}}^{\pi^-}(z),\\ D_s(z) &= D_s^{\pi^+}(z) = D_s^{\pi^-}(z) = D_{\bar{s}}^{\pi^+} = D_{\bar{s}}^{\pi^-}(z), \end{aligned} \tag{2.24}$$

$D^+(z)$ and $D^-(z)$ are so called favoured and unfavoured fragmentation functions.

2.2.2 Hardon Asymmetries

The measured semi-inclusive asymmetry of a hadron h is defined as

$$A_{\parallel}^h = \frac{\sigma_h(180^\circ) - \sigma_h(0^\circ)}{\sigma_h(180^\circ) + \sigma_h(0^\circ)} \tag{2.25}$$

Furthermore, we define

$$g_1^h(x,z) = \frac{1}{2}\sum_q e_q^2 D_q^h(z)\Delta q(x), \text{and} \tag{2.26}$$

$$F_2^h(x,z) = 2x\frac{1}{2}\sum_q e_q^2 D_q^h(z)\Delta q(x); \tag{2.27}$$

in order to express the following relation between the polarised and unpolarised parton density functions, the fragmentation functions and $A_{\parallel}^h(x,z)$:

$$\frac{\sum_q e_q^2 D_q^h(z)\Delta q(x)}{\sum_{q'} e_{q'}^2 D_{q'}^h(z)\Delta q'(x)}[1+R(x,Q^2)] = \frac{A_{\parallel}^h(x,z)}{D} \tag{2.28}$$

where we assumed $A^h = 0$ as in the inclusive case. The measured longitudinal asymmetries corrected with the depolarisation factor D is written as

$$A^h(x,z) = \frac{A_{\parallel}^h(x,z)}{D}; \tag{2.29}$$

In the quark parton model, the hadron spin asymmetries do not depend on Q^2.

3 HERMES Experiment

HERMES experiment was designed to study completely and precisely the structure of spin effect by use of spin-dependent deep inelastic scattering of positrons off polarized nucleons. HERMES uses HERA electron beam. HERMES uses new techniques in its experiment : polarised electron storage ring and polarised internal gas targets. Fig3.1 shows the HERMES in the HERA storage ring.

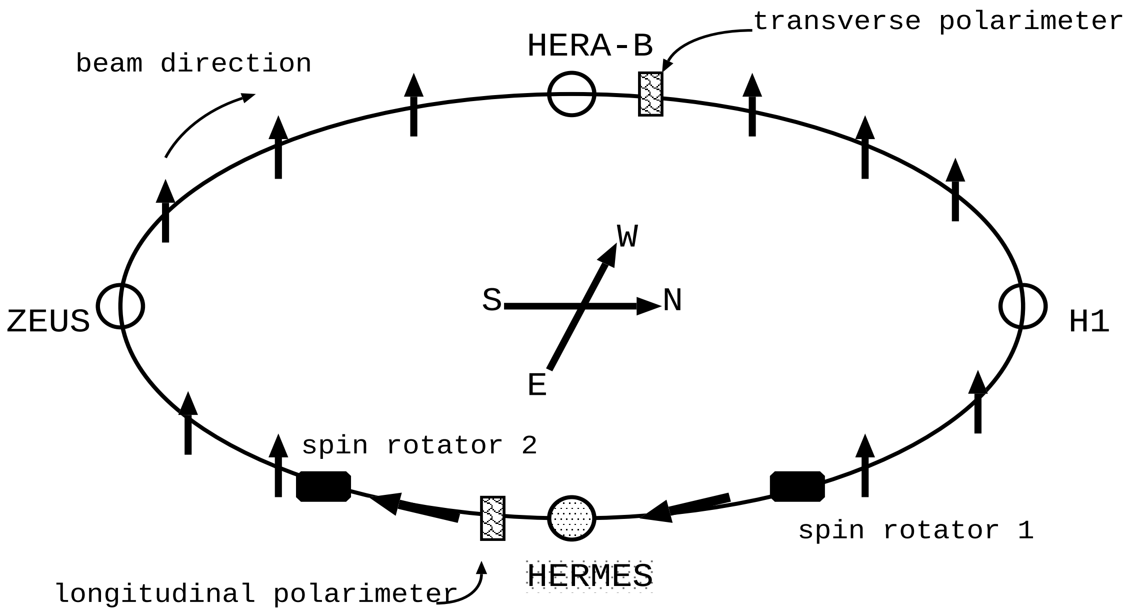

Figure 3.1: Schematic view of the HERA at DESY. Over the storage ring, four experiments are now being carried on: H1, ZEUS, HERMES, and HERA-B.

3.1 The Polarized Beam of HERA

The HERA has a 6.3km long beam storage at DESY. The energy of the electron beam is 27.5GeV. HERMES experiment uses electron beam with its detector located in the East-Hall. The positron beam becomes transversely polarized by the Sokolov-Ternov effect. Two spin rotators are installed up and downstream of HERMES to turn the transverse polarization of the positron beam into the longitudinal direction. HERMES beam polarization grows asymptotically in 30 minutes after the beam injection into HERA. The typical beam current is 35 mA.

3.2 Targets

It is technically impossible to polarize the nucleons of a pure solid material to a high degree and use them as a target in a lepton beam. HERMES uses gas internal targets. HERMES uses storage cell technique to enhance the target density. Now the target thickness achieved is $7 \cdot 10^{13}$atoms/cm^2, which is more than two orders of magnitude higher compared to the target thickness by a free jet target, usually $2 \cdot 10^{11}$atoms/cm^2.

Fig3.2 shows the HERMES target. From one side, the gas atoms are injected into a thin-walled, T-shaped tube which is called "storage cell". The target atoms remain inside the cell for typicall 3ms and cross the interaction region many times. When the target atoms are in the target cell, the following interactions are assumed:

- Recombination: the atoms inside the target cell hit the cell walls and form molecules.
- Wall depolarization: the atoms attached to the wall by collision lead to a relaxation of the atom polarization by the interaction with surface magnetic fields.
- Spin exchange collisions: a collision of the atoms may lead to a spin exchange between the hyperfine states of the atoms and cause exchange of electron and proton polarization.

The storage cell is made of aluminum with its length of 400mm and its wall thickness of 0.125mm.

3.3 The HERMES Spectrometer

The purpose of the HERMES spectrometer is to determine the momentum of particles after the interactions in the target. The HERMES spectrometer consists of two identically constructed halves, one above and one below, divided along the HERA beam lines. Charged particles travelling through a magentic field are deflected and are detected as they pass through tracking chambers. Also a large magnet in conjunction with tracking chambers in the front and back regions are used to determine the momentum of charged particles. There are four particle identification detectors: a transition radiation detector, a Cerenkov counter, a calorimeter and a preshower detector installed in the spetrometer. Fig3.3 shows the HERMES spectrometer.

HERMES has its own defined coordinate system. The origin of the coordinate system is at the center of the target. The positive $z-$ axis is along the direction of the beam. The $y-$ axis is oriented vertically up and the $x-$ axis is the remaining direction in a right handed coordinate system.

3.4 The Magnetic Spectrometer

In this section an overview of the HERMES spectrometer is given. Fig3.4 shows the side view of the spectrometer.

3.4.1 The Magnetic Spectrometer and Tracking

The HERMES spectrometer magnet deflects charged particles in order to measure their momentum. The dipole magnet provides a vertical field with an integral of $\int Bdl = 1.3T \cdot m$. The fringe fields are protected by the field clamps on both sides of the magnet from the adjacent detectors. The infulence of the magnetic field on the positron beam is compensated additionally by a correction coil.
The HERMES tracking system consists of gas-micro-strip chambers and drift chambers in the front region, proportional chambers in the magnet and two sets of drift chambers in the back region. They are called Vertex Chamber(VC), Front Chamber(FC), Magnet Chamber(MC) and Back Chamber(BC).
The parameters of the Tracking Chambers are show in (Table 3.1).

Vertex and Front Chambers

The micro-strip gas counter called Vertex Chambers(VC 1/2) are located just behind the target exit window in order to measure the scattering angle of the scattered particles. Each Chamber consists of three planes with the orientations vux and xvu, respectively. Each plane is assembled out of 300 μm thick glass substratums which are covered with 7μm aluminium strips separated by 193μm and are mounted in 3 mm distance to a cathode plane. The high number of channels leads to a good resolution even with digital readout and reduces the sensitivity of the track reconstruction to low energy background hits. The spatial resolution of each module is 57 μm.

The Front Chambers(FC 1/2) are installed behind the Vertex Chamber and just before the magnet in order to measure the angles of the track precisely. The Front

	Vertex	Front	Magnet	Back
Detector	VC1 / VC2	FC1 / FC2	MC1/ MC2/ MC3	BC1,2/ BC3,4
Type	micro-strip gas	hor. drift	proportional	hor. drift
Num. of planes	3/3	6/6	3/3/3	6,6/6,6
z-Pos.(mm)	727/927	1526/1637	2655/3060/3423	4150/5900
Active hor.(mm)	420/420	680/680	966/1216/1424	1888/2890
Active vert.(mm)	137/145	220/220	263/306/347	520/710
Cell size	193 μm	7 mm	2 mm	15mm
Resolution(nom.)	57μm	150 μm	577 μm	150μm
Chamber gas	DME-CO_2	Ar-CF_4-CO_2	Ar-CF_4-CO_2	Ar-CF_4-CO_2
Gas mix	60:40%	90:5:5%	65:5:30%	90:5:5%
High Voltage	2kV	1.4kV	2.8kV	1.75kV
Readout	digital(APC)	TDC	digital(PCOS)	TDC
Channels(x)	1674/2046	96/96	496/608/720	120/192
Channels(μ/v)	2170/2170	96/96	512/608/720	118/186
Rad.length	1.2%	0.20%	0.29%	0.26%

Table 3.1: Design parameters of the tracking chambers

Chambers consist of two drift chambers with its resolution 150 μm.

Magnet Chambers

The Magnet Chambers are three wire chambers, installed in the rear part of the magnet where most of the low energetic backgound is deflected into the magnet yoke. Each module consists of one x, u and v plane which are built by two cathode foils enclosing a plane of anode wires with a wire distance of 2 mm. The Magnet Chambers set has a resolution of about 577 μm.

Back Chambers

The Back Chambers(BC1,2,3,4) are installed behind the magnet. BC1,2 are before the Cerenkov Counter while BC3,4 are behind the Cerenkov Counter to fulfill the whole tracking. The set of Back Chambers has a spatial resolution of about 150 μm.

3.4.2 Particle Identification Detectors

One major issue of HERMES is the identification of the scattered and other particles (pions, kaons, protons, etc.). HEREMS uses four PID detectors now.

Calorimeter

The HERMES Calorimeter consists of two halves of 42 x 10 blocks of F101 lead glass for each. The cross section and depth is 9 x 9 cm^2, 50 cm, respectively. The purpose of the calorimeter is to provide a trigger for positrons with a positron identification against hadrons, and to measure the energy of the positrons and the photons from radiative processes or from π^0 and η decays. The energy resolution for electric-magnetic showers induced by scattered positrons is energy dependent as follows:

$$\frac{\Delta E}{E} = 1.47\% + \frac{5.14\%}{\sqrt{E/(GeV)}} \tag{3.1}$$

Because the depth of a F101 glass block is about 18 radiation lengths, the eletrons will lose all their energy in the calorimeter. Hadrons only deposit a fraction of their energy in this counter because of their longer nuclear interaction length in the F101 lead glass. The calorimeter is used to separate hadrons and charged leptons.

Hodoscopes

HERMES has two hodoscope walls which are installed before and behind TRD (Transition Radiation Detector). The first one (H1) which is instlled before the TRD consists of 2 x 42 scintillator paddles with attached photomultipliers. It serves as trigger on charged particles. The other hodoscope befind the TRD is called Preshower, which consists of 1.1cm lead layer in front of a hodoscope plane identical to H1. Because the longitudinal shower of positrons and pions are different, they can be separated by the amplitude of the preshower signal to that of calorimeter.

Transition Radiation Detector

If a charged particle crosses the boundary of materials with different dielectric constants, transition radiation is emitted. A high energy particle with a larger γ factor will emit several KeV photons , while a small γ factor particle just emit lower energy photons. By using this principle, electrons and hadrons can be separated because for the same energy, their γ factor differs a lot. The HERMES TRD consists of 6 consequent modules per detector half, each built of a 6.3cm thick radiator and a 2.54 cm thick X-ray detector.

The previous Cerenkov Detector

The HERMES Cerenkov Detector is installed between BC1/2 and BC3/4 in order to identify the hadrons such π, k, p and μ. This detector uses the principle that if a charged particle is passing a medium with a velocity larger than the speed of light in that medium, it will emit Cerenkov radiation. The previous threshold Cerenkov Detector has just been replaced with a Ring Imaging Cerenkov counter which can separate pions, kaons and proton in an energy range between 2 GeV to 20 GeV. This will be described in the following chapter in detail.
Fig3.7 shows the previous threshold Cerecnkov detector. Fig3.8 is schematic view of the converted Ring Imaging Cerenkov counter.

The Trigger

The purpose of the trigger is to signal the readout electronics of the detectors when an event of interest occurs. In HERMES, it is the detection of a positron from a deep inelastic scattering event. The HERMES first level trigger is operated in a flexible way by using programmable logic units(PLUs). It is a coincidence of hits in the two hodoscopes, the Cerenkov counter and column-wise summed calorimeter signals. The trigger uses the HERA electron bunch timing as its clock.
For the HERMES 30 mA positron beam current, the trigger rate is 65Hz, depending on the target gas density. The typical background trigger rate is about 4Hz.

The Luminosity Monitor

The HERMES Luminosity Monitor is installed in the back region of the HERMES spectrometer. The luminosity is monitored by two 3 x 4 arrays of radiation hard $NaBi(WO_4)_2$ crystal located on opposite sides and close to the positron beam pipe at the position of the electromagnetic calorimeter. Each block has dimensions of 22 mm x 22 mm x 200 mm with a photomultiplier mounted on its back part. A diagram of the luminosity monitor is shown in Fig 3.8 .

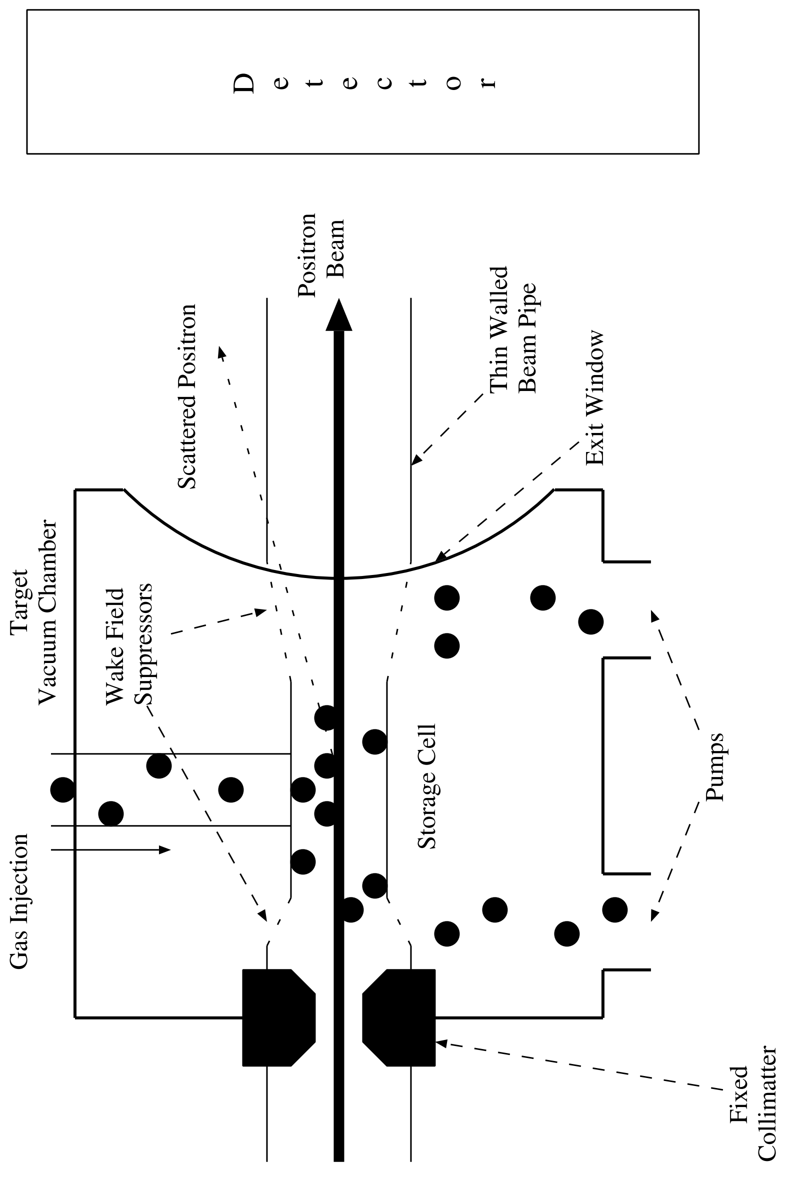

Figure 3.2: Schematic side view of the target chamber with storage cell

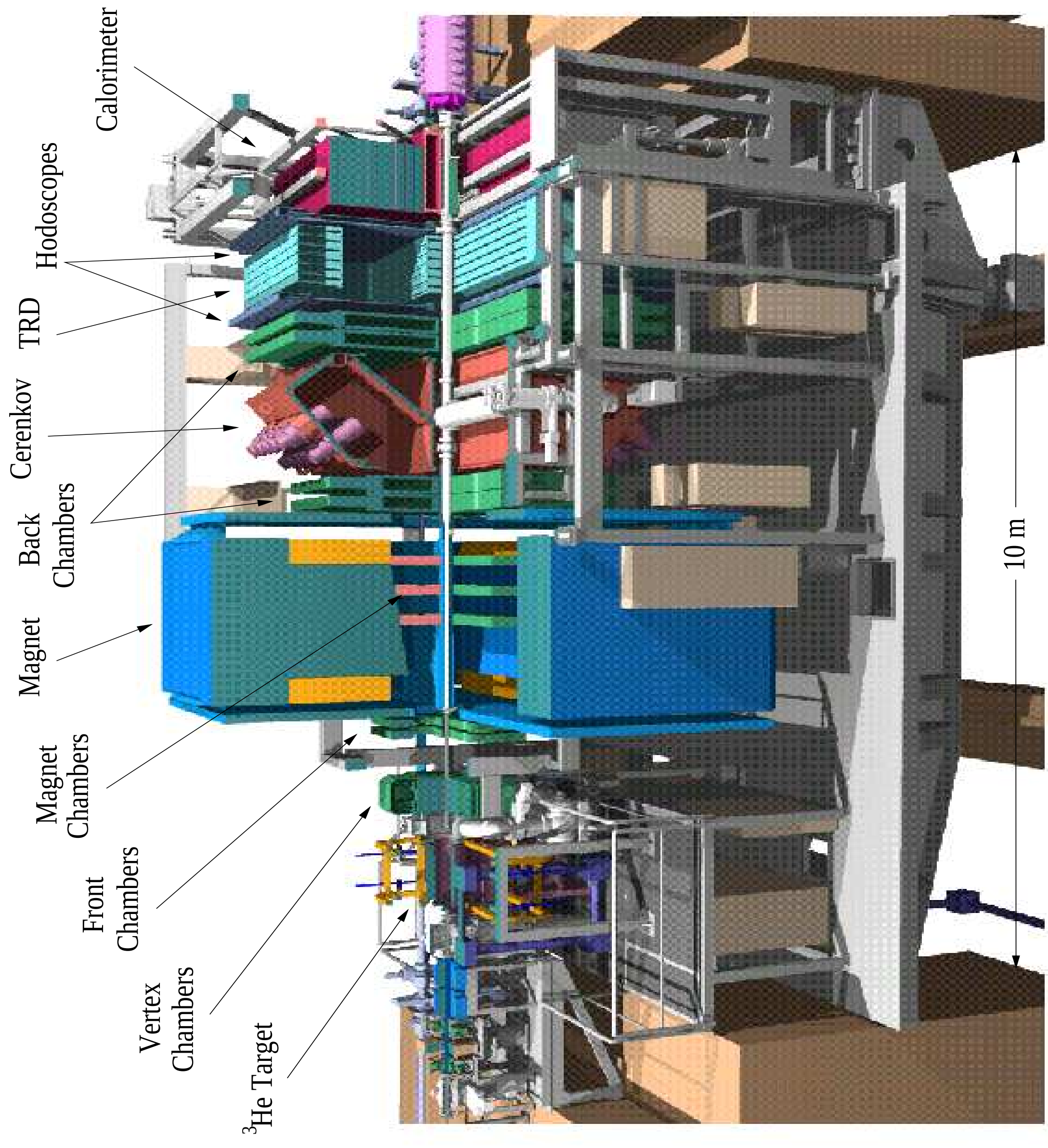

Figure 3.3: Side view of the HERMES spectrometer

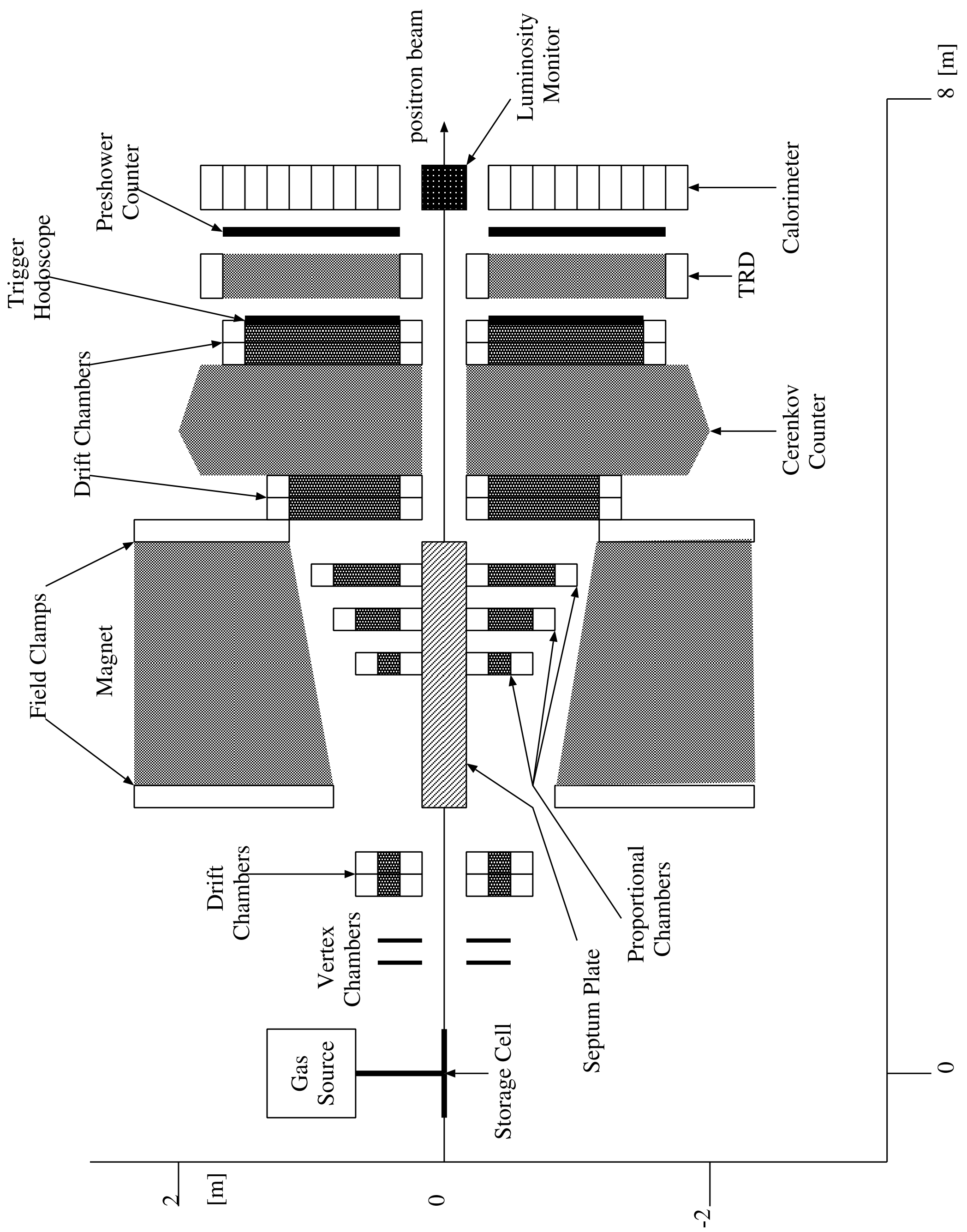

Figure 3.4: Schematic side view of the HERMES spectrometer

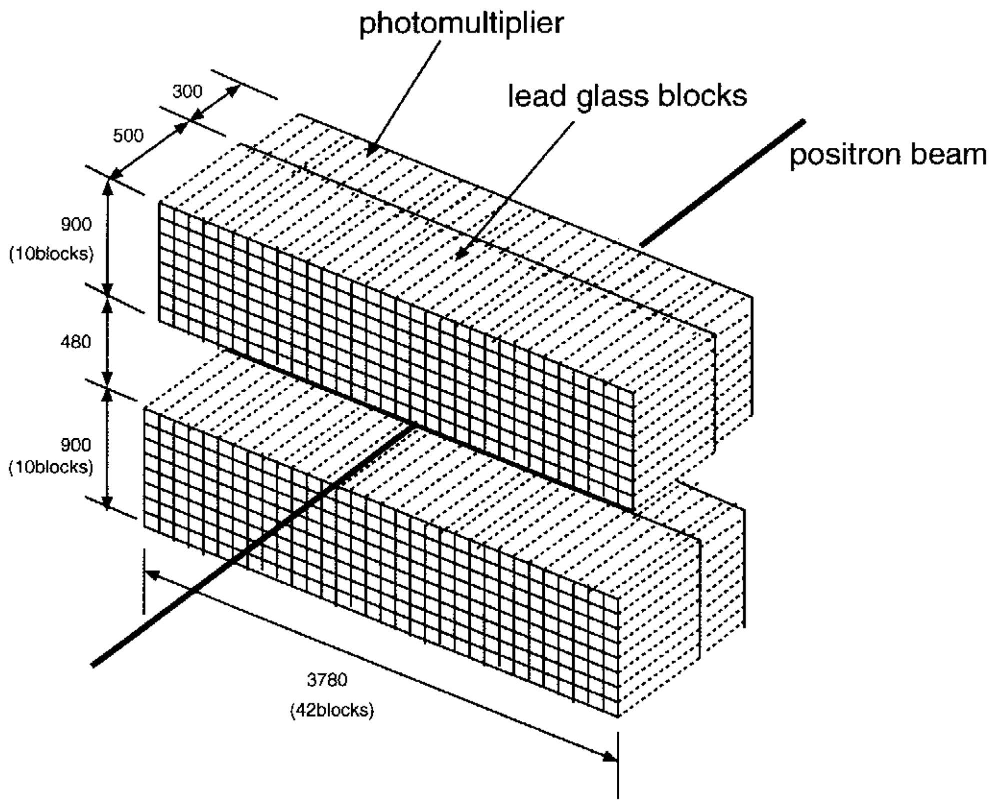

Figure 3.5: Schematic view of the calorimeter

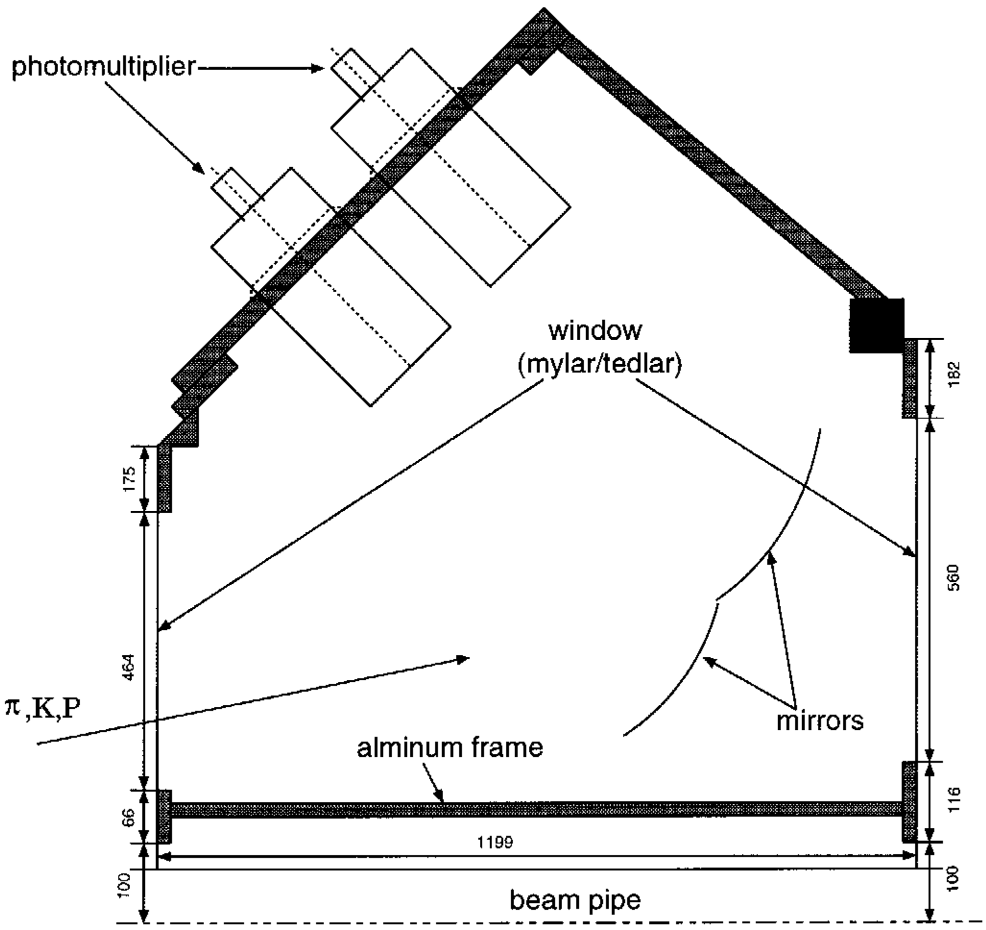

Figure 3.6: Schematic view of the previous Cerenkov counter.

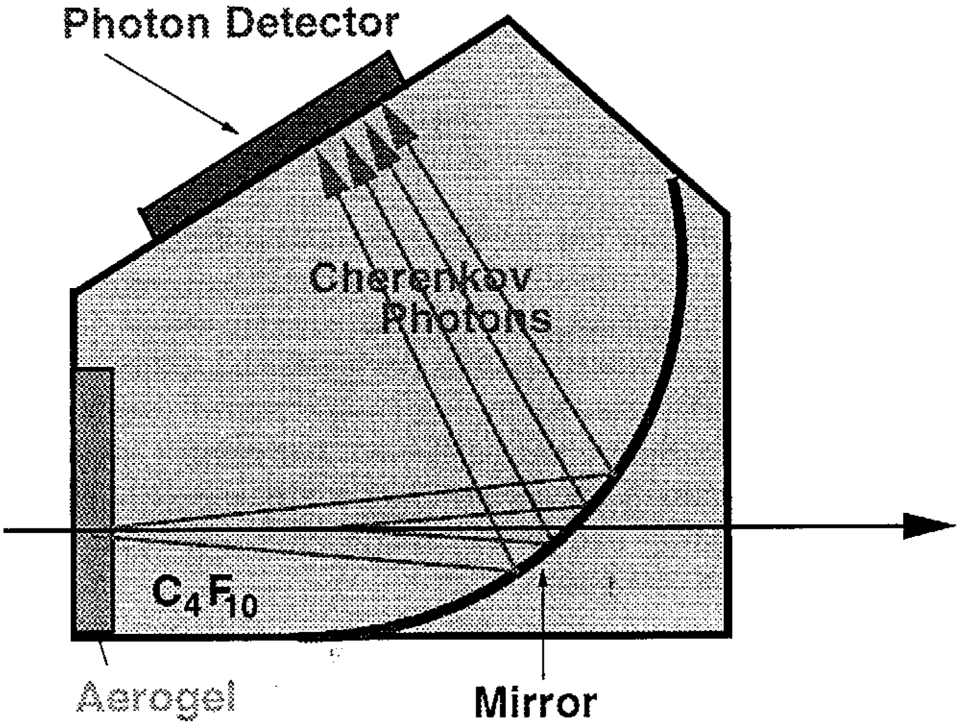

Figure 3.7: Schematic view of the new Ring Imaging Cerenkov Counter.

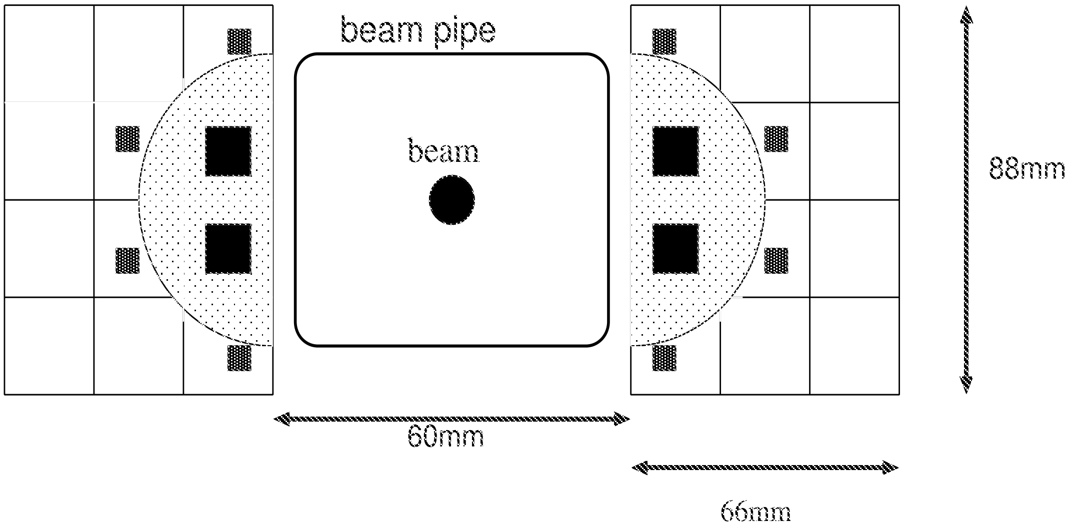

Figure 3.8: Schematic front view of the luminosity monitor. The size of the boxes represents the number of hits in each block. The shaded area shows the beam pipe acceptance.

4 Ring Imaging Cerenkov Counter (RICH) for HERMES

As mentioned in the previous chapter, the threshold Cerenkov counter has been replaced with a Ring Imaging Cerenkov counter in order to enhance the particle identification capability [RICH97].

4.1 Physics Motivation

First, we will describe the principle of Cerenkov radiation[KATO94].
Suppose a charged particle is passing in a radiator with refractive index n, its electromagnetic potential can be written as :

$$\begin{aligned} \phi &= \frac{q}{4\pi\epsilon}\frac{1}{s}, \\ \vec{A} &= \frac{q\mu}{4\pi}\frac{\vec{v}}{s}, \\ s &= r - (\vec{v}\cdot\vec{r})\frac{n}{c} \end{aligned} \tag{4.1}$$

where c is the speed of light in vacuum. Then the electric and magnetic field can be expressed as:

$$\vec{E} = \frac{q}{4\pi\epsilon s^3}[1-(\frac{nv}{c})^2][\vec{r}-\frac{rn\vec{v}}{c}], \tag{4.2}$$

$$\vec{B} = \frac{n(\vec{r}\times\vec{E})}{rc} \tag{4.3}$$

In vacuum, if the speed of the particle keeps the same, the field will become close to zero where r has a large value. While in radiator, when $r - rn(v/c)\cos\theta = 0$, there is a direction that its field is infinity. It means that there is a radiation with its angle θ. The current of a charged particle can be written as:

$$\vec{j} = q\vec{v}\delta(x'-vt)\delta(y')\delta(z') \tag{4.4}$$

where $\vec{v}$ is the velocity of the particle. By Fourier translation

$$\vec{J}(\omega) = \frac{1}{2\pi}\int \vec{j}\exp(i\omega t)dt = \frac{q}{2\pi}\delta(y')\delta(z')\exp(i\omega x'/v)\vec{x}_0 \tag{4.5}$$

where $\vec{\xi}(x', y', z')$ is the position of the particle. So the radiation energy will be

$$\frac{dW(\omega)}{d\Omega} = \frac{1}{4\pi}(\frac{\mu}{\epsilon})^{1/2} \mid \int (\vec{J}(\omega) \times \vec{k})\exp(-i\vec{k}\cdot\vec{\xi})dV' \mid^2 \tag{4.6}$$

where k is wave vector having a value of $(\omega n/c)$. A vector calculation leads to:

$$\begin{aligned} \frac{dW(\omega)}{d\Omega} &= \frac{q^2\omega^2 n}{16\pi^3\epsilon_0 c^3} \\ &\times \int \mid \int \exp i(\frac{\omega x'}{v} - kx'\cos\theta)dx' \mid^2 \sin^2\theta d\Omega \end{aligned} \tag{4.7}$$

By intergrating over x' from $-x$ to $+x$:

$$W(\omega) = \frac{nq^2\omega^2}{2\pi^2 c^3\epsilon_0} \times \int_{-x}^{x} \sin^2\theta \cdot \frac{\sin^2\theta[\omega(1 - nv\cos\theta/c)(x/v)]}{\omega^2(1 - nv\cos\theta/c)^2/v^2} d(\cos\theta) \tag{4.8}$$

Integrating it from $-\infty$ to ∞, $W(\omega)$ will be

$$\begin{aligned} W(\omega) &= \frac{nq^2\omega^2}{2\pi^2 c^3\epsilon_0}[1 - (c/nv)^2]\frac{cx}{n\omega}\int_{-\infty}^{\infty}\frac{\sin^2 y}{y^2}dy \\ &= \frac{xq^2}{2\pi c^2\epsilon}[1 - (\frac{c}{nv})^2]\omega \end{aligned} \tag{4.9}$$

If the charge of the particle is $q = ze$, the particle will lose the following energy after passing dL in the radiator:

$$\frac{dW}{dL} = \frac{z^2 e^2}{4\pi\epsilon_0 c^2}\int (1 - (\frac{c}{nv})^2)\omega d\omega \tag{4.10}$$

The number of photons is,

$$\frac{d^2N}{dld\lambda} = \frac{2\pi\alpha z^2}{\lambda^2}(1 - \frac{1}{n^2\beta^2}) = \frac{2\pi\alpha z^2}{\lambda^2}\sin^2\theta \tag{4.11}$$

where $\beta = v/c$ and α is the fine structure constant. From Hugens's principle the radiation will have angle θ which is $\cos\theta = \frac{1}{n\beta}$.

The previous threshold Cerenkov counter of HERMES provided the only hadron identification at HERMES (electron/hadron discrimination is provided by the other

PID counters). The raditor was a 30 %/70 % mixture of C_4F_{10} and N_2, with a Cerenkov threshold of $\gamma_t = 27.5$, corresponding to hadron energy threshold of 3.8, 13.6 and 25.8GeV for pions, kaons, and protons. Interesting hadron energies are in the range $2 \le E_h \le 20$GeV. Pions, the most common hadron, can be identified for $3.8 \le E_h \le 13.6$GeV with an extremely small contamination from kaons that generate knock-on electrons (electrons radiate at all energies of interest). Kaons can not be cleanly identified even at $E_h \le 13.6$GeV because of contamination from the few percent of the pions where the detector's inefficiency prevents detection of the pions' Cerenkov light.

Now we use a new Ring Imaging Cerenkov detector. The hadrons can be identified not only by the presence or absence of Cerenkov light, but also by the openning angle of the Cerenkov cone or angle, θ. The energies of the hadrons produced in HERMES are between 2 and 20GeV. Most of them are below 10GeV, a region in which it has not been feasible to sepatate pions, kaons, and nucleons with standard PID techniques. Threshold Cerenkov system using heavy gases, such as C_4F_{10}, at atmospheric pressure is useful only for energies above 10GeV since the kaon threshold for Cerenkov radiation is typically > 9GeV. Use of a high pressure gas system is not technically feasible in HERMES. Clear liquid radiators are useful for hadron identification below $\approx$ 2GeV because of their correspondingly very low Cerenkov light thresholds. Heavy gas-liquid dual radiator RICH detectors have been operated successfully in a number of high energy collider experiments. However, a "blind" region has remained, exactly matching the HERMES energy.

With the recent development of new clear silica aerogels having low index of refraction (from 1.0 to 1.2)[Deleo97], it becomes possible that this difficult energy region can be spanned. Aerogels have long been used in threshold Cerenkov counters[Adachi95], but their use as a radiator in a RICH system is a recent development which has resulted from the availability of material with excellent optical properties. New production techniques have yielded aerogels with much more uniform and smaller colloidal SiO_2 particle structures. The more uniform granular structure suppresses Rayleigh scattering of visible light and greatly enhances its transmission. The HERMES RICH uses aerogels with its average indices of 1.03. For aerogel with n(index) = 1.03, the kaon threshold for Cerenkov radiation is 2 GeV. It is feasible to use such an aerogel for PID in the region between 2 and 10 GeV, and to combine its operation

with that of a heavy gas C_4F_{10}, to generate Cerenkov rings over the full HERMES momentum. The Cerenkov angles produced with this radiator combination for pions, kaons, and protons are plotted in Fig4.1 as a function of particle momentum. Fig4.2 shows the ring of Cerenkov photon from aerogel and gas radiator by Monte Carlo simulation with the energy of π with $p_\pi = 8.75 GeV/c$
Table4.1 shows the engery region of the particle identification.

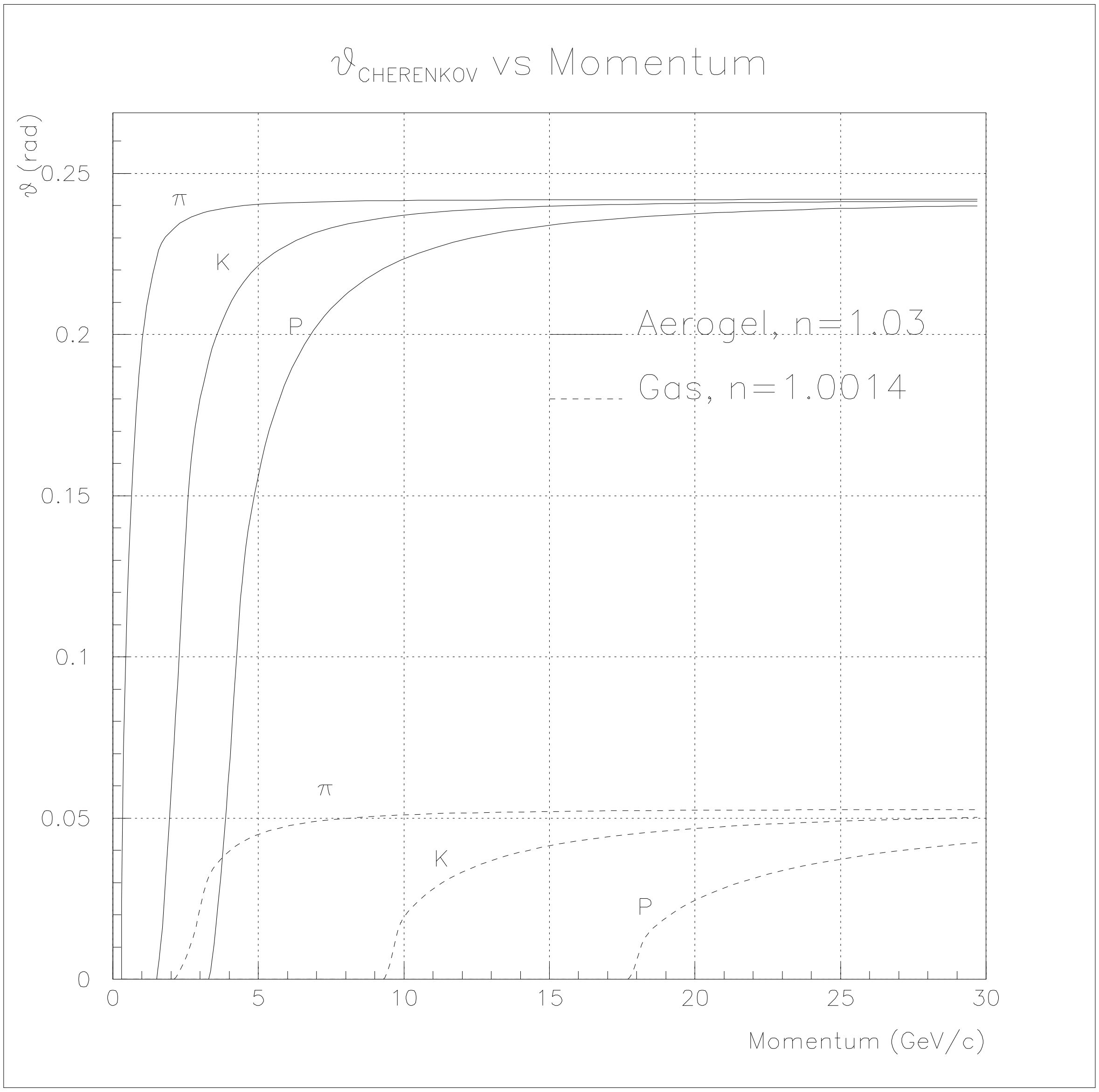

Figure 4.1: The Cerenkov angle versus the hadron momentum for the aerogel and gas radiators.

FIG. 4. The Čerenkov angle versus the hadron momentum for the aerogel and gas radiators.

As described above, a charged particle moving with velocity $v = c\beta$ in an opticle medium of refractive index n will emit Cerenkov radiation when v exceeds the velocity of light in the medium. The Cerenkov emission angle θ relative to the particle

wavelength λ through a thickness L is proportional to e^{-CL/λ^4}, where C characterizes the light attenuation by scattering. Recent samples have $C \approx 0.01\,\mu m^4/cm$ and lower. Such material has high transmission above 400 nm

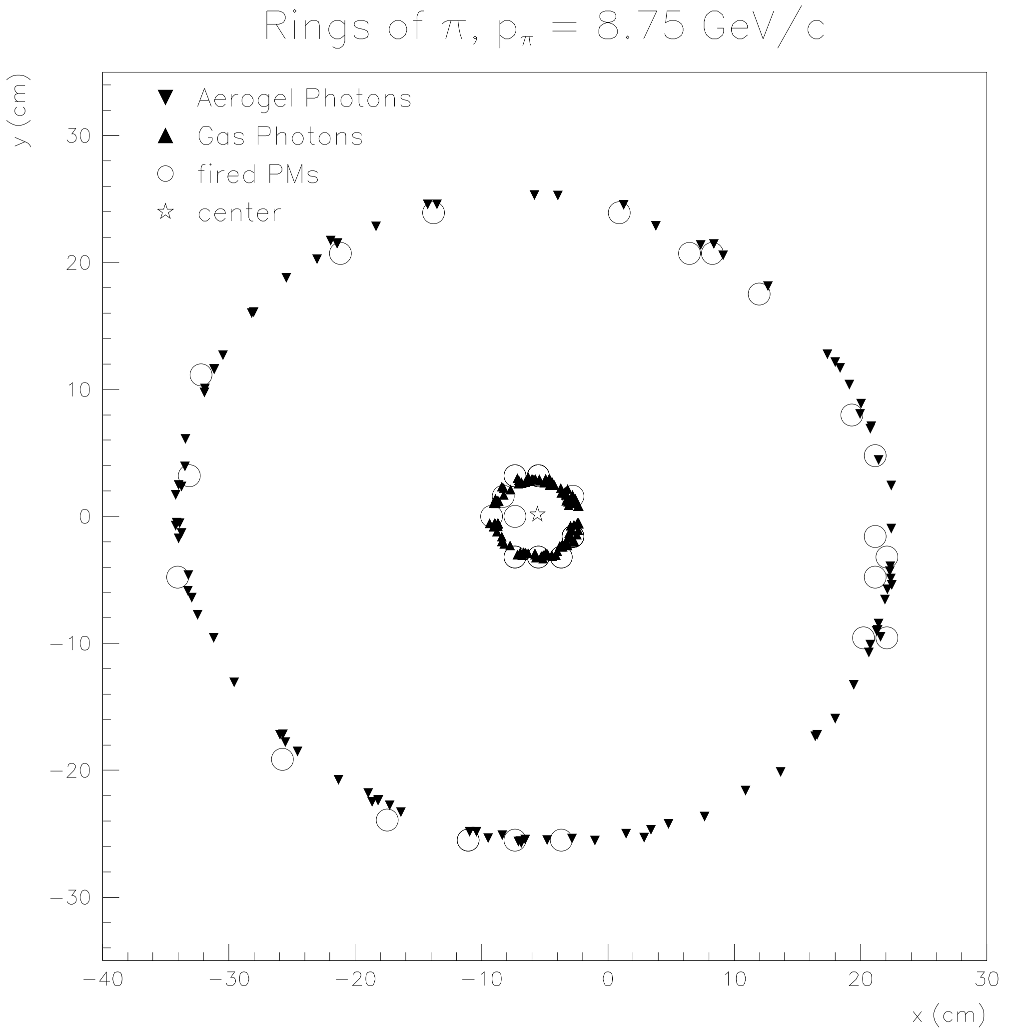

Figure 4.2: Ring of Cerenkov photons from the aerogel and gas radiators

FIG. 13. Čerenkov photons and PM's response.

direction is

$$\cos\theta = 1/(n\beta) \tag{4.12}$$

then

$$\sigma_\theta = \frac{\sigma_\beta \cot\theta}{\beta} \tag{4.13}$$

The number of photons is

$$N = N_0 Z^2 L \sin^2\theta, \tag{4.14}$$

then

$$\frac{\sigma_N}{N} = \frac{1}{\sqrt{N}} = 2\sigma_\theta \cot\theta, \tag{4.15}$$

PMs with radius r. The vector $\vec{t}_{ij} = a_i\vec{u} + b_j\vec{v}$ points to the center of the cell ij; $\vec{u} \doteq (r, 0)$ and $\vec{v} \doteq (\sqrt{3}r, r/2)$ respect to the cartesian coordinate system. Fig 13 shows the typical rings produced by the photons emitted in the aerogel and in the gas and their digitization: the small circles represent the size (active and non active area) of the fired PMs; the hexagonal cells are not drawn.

A. Status of the HPD development

The HPD is a photosensitive device with a number of features that perfectly match with the requirements of the dual radiator RICH envisaged in HERMES. Indeed its major merit is the combination of a good position

mercial
are not
In fact
unit, w
tive sur
their p
conveni
diamete
means
sands [2
system,
cuit mu
This ap
an activ
of the e
of such
Two

1. a
d
P

2. a
m
[2

The
compar
CERN,
ing resu
[27,28]
attemp
LHC-B
to the
ized an
In the
ity will
INFN
produc
the pro

Particle	Momentum[GeV]	Signature	Main Contamination
p	$2.0 - 3.5$	no aerogel ring	–
	$3.5 - 10.0$	emission angle of aerogel ring	K
	$10.0 - 17.5$	no gas ring	–
	$17.5 - 20.0$	emission angle of gas ring	–
K	$2.5 - 9.0$	no gas ring and emission angle of aerogel ring	p
	$10.0 - 20.0$	emission angle of gas ring	π
π	$0.5 - 2.5$	aerogel ring	μ
	$2.5 - 10.0$	gas ring	μ
	$10.0 - 20.0$	emission angle of gas ring	μ
μ	$2.0 - 4.0$	emission angle of gas ring	π
e	$0 - 2.0$	aerogel and gas ring	π
	$2.0 - 8.0$	emission angle of gas ring	π

Table 4.1: Particle type signatures. Electrons and positrons are assumed to be identified by the preshower, calorimeter and TRD

Then the resolution of a RICH detector for a single photoelectron becomes

$$\frac{\sigma_\beta}{\beta} = \tan\theta \frac{\sigma_\theta}{\sqrt{N}} \tag{4.16}$$

The particle identification capability of a RICH counter can be obtained by considering the variable $u = \sin^2\theta$, which can be written as

$$u = 1 - (1/n)^2 - (m/pn)^2 \tag{4.17}$$

where p and m are the particle momentum and mass. The number of standard deviation n_σ to discriminate mass m_2 from m_1 is then obtained

$$n_\sigma = \frac{u_2 - u_1}{\sigma_u/\sqrt{N}} = \frac{m_2^2 - m_1^2}{p^2 n^2}\left(\frac{\sqrt{N}}{\sigma_u}\right) \tag{4.18}$$

where σ_u is the error in u per single photoelectron and $\sigma/\sqrt{N}$ is the error for N photoelectrons. For a given design, of the maximm momentum p_{max} for which the discrimination of particle with masses m_2 and m_1 can be obtained with a separation of the two relative distributions by a number of standard deviations n_σ:

$$p_{max} = \sqrt{\frac{m_2^2 - m_1^2}{2k_f n_\sigma}} \tag{4.19}$$

where $k_f = \tan\theta\sigma_\theta/\sqrt{N}$ is the RICH detector constant, and N is the number of fired photonmultipliers, θ is the Cerenkov angle and σ_θ the standard deviation of its distribution[TYps94].

The effect on the resolution can be estimated as follows. The average angular deflection from multiple scattering for a fully relativistic particle of unit charge is given by:

$$\Delta\Phi = \frac{1}{\sqrt{3}}\frac{0.0136GeV}{P}\frac{t}{X_0}[1 + 0.038ln\frac{t}{X_0}] \tag{4.20}$$

where t/X_0 is the thickness in radiation lengths and P is the momentum of the particle. The smearing of the reconstructed emission angle θ arising from multiple scattering is then:

$$\Delta\theta \sim \Delta\Phi\frac{l_C}{l_{BC}} \tag{4.21}$$

where l_C = 1.5m is the separation between the front of the Cerenkov counter and $BC3/4$ and l_{BC} = 1.8m is the separation between $BC1/2$ and $BC3/4$. For the HERMES magnet

$$\theta \sim \frac{0.4GeV}{P} \tag{4.22}$$

Thus the effect on the resolution can be estimated as :

$$\frac{\Delta P}{P} \sim \frac{\Delta\theta}{\theta} \sim 0.5\% \tag{4.23}$$

for RICH.

Component	Thickness(X_0)
Aerogel	0.020
C_4F_{10}	0.042
Mirror	0.012
Aluminum windows	0.034
Total	0.018

Table 4.2: Thickness of materials in the RICH detector in units of radiation length

4.2 RICH Setup

The previous threshold Cerenkov counter is shown in Fig3.6. The radiator boxes, which are 1.26m in depth, are located in the HERMES spectrometer between the rear tracking chambers $BC1/2$ and $BC3/4$(see also Fig3.3). The previous radiator was a mixture of dry nitrogen and perfluorobutance gas C_4F_{10} at atmospheric pressure. The body of the counter is constructed of aluminum, with entrance and exit windows each consisting of dual foils of 100μm of mylar and 30μm of tedlar. The volume of each half is approximately 4000 l.

Next, we will describe the new RICH of HERMES. The new parts are aerogel widow, mirror system, photon detector and data taking system.

4.2.1 Aerogel Wall

Aerogel tiles play a very important role in the RICH system, as it is the radiator for Cerenkov photons.

Fig3.7 shows the schematic view of the RICH. Here the aerogel radiator is an assembly of about 11cm$\times$11cm$\times$1cm tiles configured to fill the entrance of the detector. Five tiles are stacked in so that the thickness becomes 5 cm. We used $17 \times 5 \times 5$ aerogel tiles to make this aerogel wall which has a space size of 202.0 cm $\times$ 55.0 cm $\times$ 5.0 cm. Totally we uesed 850 tiles to make the two halves (as mentioned upper and lower). The container which holds the aerogel tiles consists of an aluminum frame with a 1mm aluminum entrance window and 3.2mm lucite exit window transparent to wavelengths above 290nm. The lucite exit window material was chosen primarily for its transmission properties. At low wavelengths, it selectively absorbs Rayleigh-sacattered radiation and reduces the effects of a rapid change in the refractive index of aerogel. The background from lucite-generated Cerenkov radiation has been calculated to be small compared with the background expected from Rayleigh-scattered aerogel radiation and other effects.

4.2.2 Mirror System

As shown in Fig4.3, the mirror system is used to reflect the Cerenkov photons into the photon detector. It consists of two large pieces of mirror, each for one of the halves. Each large mirror consists of 8 pieces of small mirrors with the centers of their curves focusing on the same point. Their diameter is 440cm.

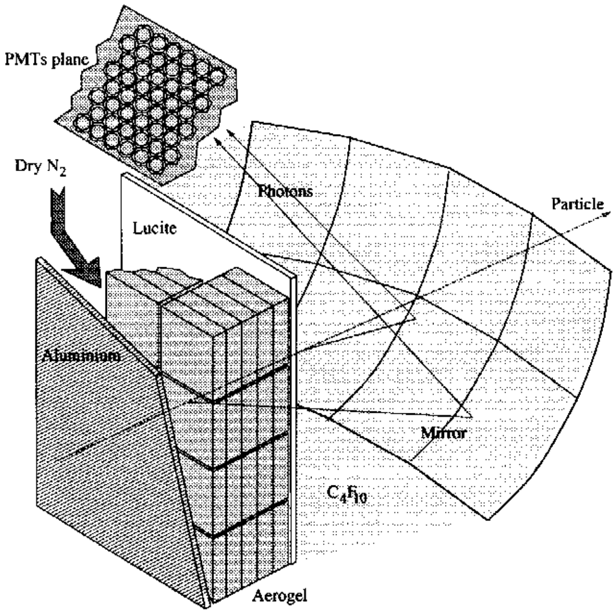

Figure 4.3: Schematic view of the HERMES RICH[Cart98]

4.2.3 Photon Detector and Readout System

The Cerenkov photons generated by the aerogle and gas radiators, reflected by the Cerenkov mirror finally reach to the photonmultiplier.

The photon detector array consists of 1008 soft steel honeycomb matrix that mounts 21 mm diamter PMTs(Philips XP1911 PM). The hexagonal closet packing has a center to center distance between the PMTs of 23.27 mm. The PMTs has a sensitive circle area of about 177 mm^2. In order to cover the focal surface as much as possible, and to increase the light gathering capability, a conical funnel is inserted in front of the PMT.

Fig4.4 is the schematic view of the PMTs. The PM array has 73 columns of 26 or 27 rows as shown in Fig4.4 . LeCroy PCOS4 system is used to be the readout system of the RICH detector. The PMT has therefore only two states: ON or OFF.

The resulting matrix holds 1934 PMTs in a hexagonal grid with 73 columns of 26 or 27 PMTs each, as shown in figure 4. Aerogel rings from a kaon and a pion are schematically indicated. The RICH detector is read out using the LeCroy PCOS4 system, originally developed for proportional chambers. The PMT response information is therefore strictly digital: on or off.

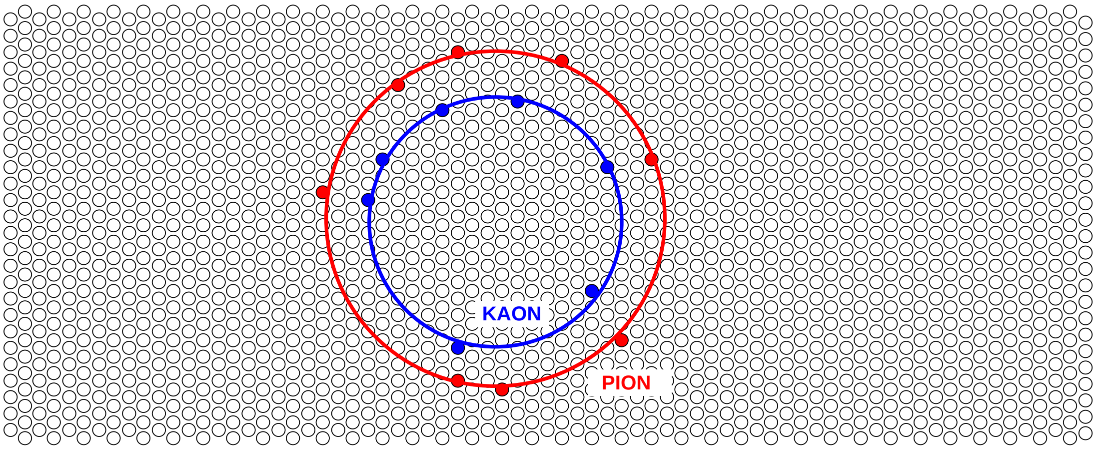

Figure 4: Schematic view of the photon detector array for one half of the RICH detector.

Figure 4.4: Schematic view of PMTs for the half of the RICH[Ral98]

1.1.2 Expected performance

Aerogel photons are produced only over the few centimeters of the aerogel, while gas photons are produced all the way to the mirror. Due to this production geometry aerogel rings are much thinner than the fairly broad gas rings. However, since the aerogel rings are much larger than the gas rings, they still contain many more PMTs (about 3 to 4 times more). Although the number of Čerenkov photons that are produced in the two radiators is comparable, there are more loss mechanisms for the aerogel photons, resulting in fewer aerogel photons hitting the detector. The combination of less photons being spread over more PMTs results in an average number of incident photons per PMT that is much smaller than 1 for the aerogel ring, whereas it is about 2 for gas rings.

If the PMT is read out through an ADC, the number of photoelectrons (and hence the number of incident photons) can be determined from the pulse height. As mentioned previously, the readout of the HERMES RICH is digital. This means that the information on the number of photoelectrons is lost. The only information available to the reconstruction programs is which PMTs *fired* (or *activated*), i.e. their pulse height exceeded a predetermined threshold. For the aerogel rings it is clear that the number of activated PMTs equals the number of photoelectrons, whereas it is considerably smaller for gas rings.

5 Measurement of Aerogel properties

The first Aerogel was made in 1931 by Steven.S. Kistler of the College of the Pacific in Stockton, California. The key aspect of aerogel production is : replace the liquid with air by some means in which the surface of the liquid is never permitted to recede within the gel. If a liquid is held under pressure always greater than the vapor pressure, and the temperature is raised, it will be transformed at the critical temperature into a gas without two phases having been present at any time.

The formation of aerogels, in general, involves two major steps, the formation of a wet gel, and the drying of the wet gel to form an aerogel. Originally, wet gels were made by the aqueous condensation of sodium silicate, or a similar material. While this process worked well, the reaction fromed salts within the gel that needed to be removed by many repetitive washings(a long, laborious procedure). The most common aerogels are tetramethyl orthosilicate (TMOS,$Si(OCH_3)_4$) which we have used for HERMES, and tetraethyl orthosilicate (TEOS,$Si(OCH_2CH_3)_4$).

Though aerogel have fascinating properties, there are some obstacle to its wide usage. A major obstacle is that the structure of aerogel collapses due to the absorption of water. The refractive index will change if the density of the aerogel changes due the absorption of water. By using a new technique called hexamethyldisilazane, the water absorption was prevented and keeps the refractive index remains the same. This is a tenchnique developed by Matsushita Electric Works[Yoko95]. Fig5.1 shows the aerogle tile. Fig5.2 shows the molecule of aerogel[Sumi97]. Fig5.3 shows the hexamethyldisilazane process.

Figure 5.1: Aerogel tile on newspaper. We can see that the aerogel has a good transparency.

5.1 Measurement of aerogel properties

140ℓ (about 1120 pieces) of Aerogel tiles were produced by Matsushita Electric Works for the HERMES RICH. The refractive index and other optical properties of these aerogels were measured in Shibata Lab. Tokyo Institute of Technology as is described in this thesis.

5.1.1 Measurement of refractive index and tile dimension

If the refractive index is different from tile to tile, the determination of Cerenkov angle becomes inaccurate. The relationship between the Cerenkov angle resolution and refractive index is

$$\frac{d\theta}{\theta} = \frac{1}{2}\frac{d\tilde{n}}{\tilde{n}} \tag{5.1}$$

where $\tilde{n} \equiv (n-1)$. Tile-to-tile difference of the refractive index can arise both from density fluctuations and optical dispersion. It is important to know the refractive

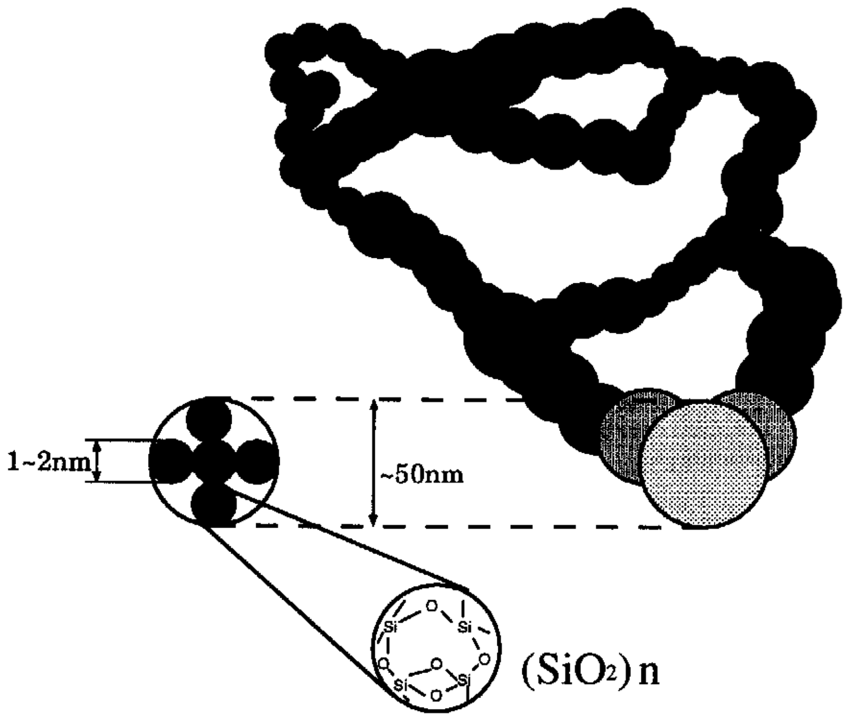

Figure 5.2: View of aerogel molucule[Sumi97]

index of all the aerogel tiles. We used a red(633nm) He-Ne laser as a light source to do this measurement. Fig5.4 shows the setup for this measurement.

By using Snell's law of refraction, assuming we have angle of incidence ξ, we can calculate θ to be

$$\theta = \xi + \arcsin(n \sin(\phi - \arcsin \frac{\sin \xi}{n})) - \phi \tag{5.2}$$

Here θ is function of ξ. If we want to get the minimum value of θ, we can differentiate ξ as

$$\frac{d\theta}{d\xi} = 1 + (\frac{\cos \xi}{n})(-\sqrt{1 - (\frac{\sin \xi}{n})^2})^{-1}(n \cos(\phi - \arcsin(\frac{\sin \xi}{n}))) \\ (\sqrt{1 - (n \sin(\phi - \arcsin(\frac{\sin \xi}{n})))^2})^{-1} = 0 \tag{5.3}$$

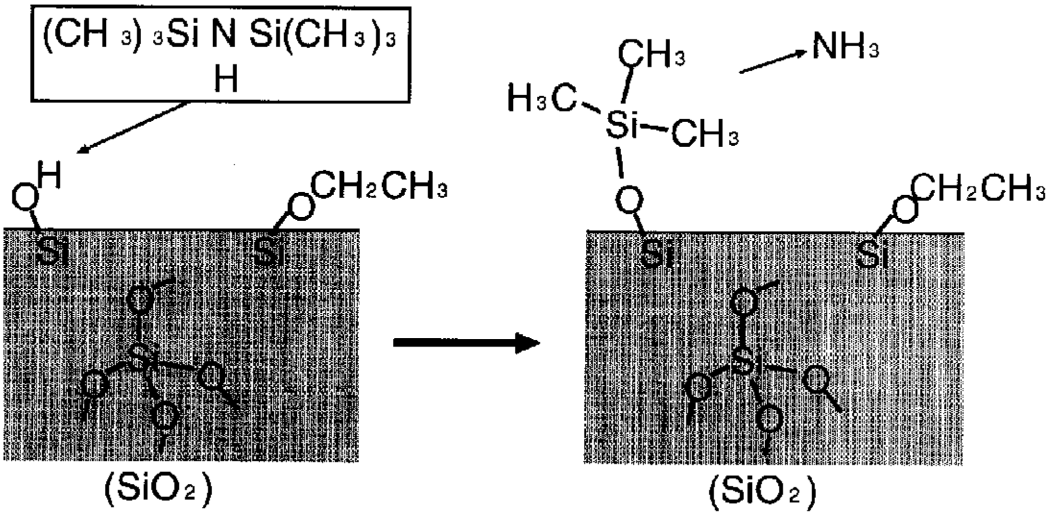

Figure 5.3: The TMS(trimethylsilyl) of the SiO_2 surface of gel using hexamethyldisilazane

from equation 5.3, we have

$$\xi = \arcsin(n \sin \frac{\phi}{2}) \tag{5.4}$$

then θ becomes

$$\theta = 2 \arcsin(n \sin \frac{\phi}{2}) - \phi \tag{5.5}$$

finally

$$n = \frac{\sin \frac{\theta+\phi}{2}}{\sin \frac{\phi}{2}} \tag{5.6}$$

θ can be calculated as

$$\theta = \arctan(\frac{X}{L}) \tag{5.7}$$

For the aerogel tiles, we have $\phi = \pi/2$. Then the refractive index is

$$n = \frac{\sin\frac{\theta+\pi/2}{2}}{\sin\frac{\pi}{4}}. \tag{5.8}$$

We can evaluate the errors δn as

$$\delta n = \frac{\partial n}{\partial \theta}\delta\theta + \frac{\partial n}{\partial \phi}\delta\phi. \tag{5.9}$$

For $\delta\theta$, we can derive it from $\theta = \arctan(X/L)$:

$$\delta\theta = \frac{\partial \theta}{\partial X}\delta X + \frac{\partial \theta}{\partial L}\delta L. \tag{5.10}$$

The measure on the screen has a resolution of ± 0.5mm. For the L, we have a value of 2789 mm with a precision of ± 1mm. For the refractive index n, we calculated the error $\delta n = 1.6 \times 10^{-4}$. Fig5.4 shows the experiment setup for measuring the refractive index.

The following environment for the measurement was prepared:

- The measurement was done in a clean room.
- The surrounding wall of the room was dust-prevented vinyl.
- Sunlight was shutted out from all the windows and entrance door.
- Air flow was prevented in the room.

The reason of measuring aerogel tiles in a clean room is that dust grains are easily attached to the aerogel tiles.

Methods of handling the aerogel tiles are:

- Use cotton gloves to pick up the aerogel tiles.
- For the measurement, aerogel tiles were placed on a plastic sheet. The sheet is envelopped by paper in order to prevent static electricity.

Aerogel tile is very breakable. We tested the methods of how to handle these aerogel tiles several times and finally the above methods were used.

Instruments which were used in this measurement are:

- He-Ne laser with its wavelength of 633 nm
- Laser beam expander
- Laser beam slit
- Turn tabel
- Plastic plate covered with paper
- Screen with a measure
- Viedo camera
- TV monitor
- A PC equipped with a calculation program

The set up was aligned by an optical instrument called "transitor" and a small reflection mirror attached to the screen. It was so aligned that the laser beam is horizontal while the screen is perpendicular to the laser beam. Since the screen has a distance of 2789 mm from the center of the turn table, the viedo camera monitor is used to take the screen image in front of the operator.

The systematic error of the measurement of the refractive index was checked by measuring the same aerogel many times and was found that it is within 1×10^{-4}.

The aerogel tile's dimensions were also measured by a vernier micrometer with a resolution of 0.5 mm. From all the measured aerogel tiles, 850 tiles were selected to be used in the RICH by their refractive index, size dimension and transparency:

- refractive index between 1.0290 and 1.0313
- dimension 113.1 mm $\leq$ x, y $\leq$ 115.1 mm and 10.25 mm $\leq$ z $\leq$ 12.25 mm

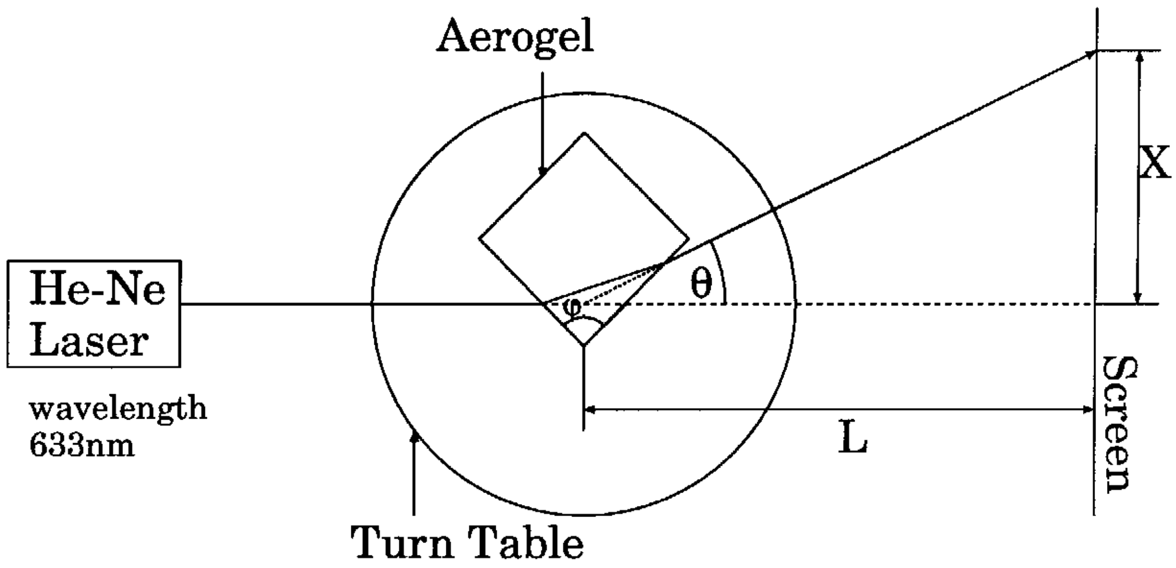

Figure 5.4: Schematic view of setup for measurement refractive index

- good transparency and no visible large cracks
- uniform surface shape

The mean refractive index and deviation for the 850 tiles are shown in Fig5.5. Fig5.6 and Fig5.7 show the mean refractive index and deviation for the tiles installed in the upper and lower halves, respectively.

Fig5.8, Fig5.9 and Fig5.10 show the x, y, z dimensions of the aerogel tiles. All the 850 aerogel tiles' refractive index and dimensions are available also in the form of a table at:
http://www.nucl.phys.titech.ac.jp/ zhang/n4html.txt

5.1.2 Measurement of temperature dependence

Till now, there is no experimental data on temperature dependence of refractive index of aerogel tile. The temperature of the HERMES experiment environment is not constant. It varies from 20°C to 26°C. We measured the correlations between temperature and the refractive index of aerogle by two steps. Fisrt we raised the environment temperature around the aerogle tile slowly, and controlled the environment temperature at a constant value, then measured the refractive index. Second we lowered the environment temperature slowly, using the same method as the above, measured the refractive index.[Kane98]

- The temperature was raised
  - from 23°C to 26°C. The refractive index minus 1 ($n-1$) decreased a little more than 1%.
  - over 26°C. The refractive index did not change.
- The temperature was lowered
  - the refractive index did not change.

The setup is the same as Fig5.4 besides the temperature controller. Fig5.11 shows our experimental data. Fig5.12 is the temperature vs time.

We found that:

- after this temperature change, the weight of the tile decreased a little less than 1%(Before:16.677g, After:15.552g).
- the probable reason of this refractive index decrease is the CO_2 gas and alcohol evaporated off the surfaces of the tiles when the temperature was raised.
- Because the refractive index of almost all the tiles was measured with ten minutes after the plastic box was openned, CO_2 gas and alcohol were most likely still attached to the surface of the tiles. Therefore, there is a probability that the real $n-1$ value is smaller by $1-2\%$ than the refractive index measured at that moment.

This data of refractive index vs temperature will be useful when the aerogel radiator is used for a long term.

5.1.3 Measurement of the surface shape

The surface structure of an aerogel tile is related to the directions of the Cerenkov photons when they are entering this tile. The surface structure was measured by a method of mechanical contact with Surf Tester (Mitutoyo Co.) which has a precision of 0.05μm. Fig5.13 shows the fitted surface structure.

The surface structure of the aerogel tile is fitted by two functions. One function covers the region from the edge to about 5 mm inside. The other function covers the central region of the tile. The functions were determined by the following conditions:

- Use quadratic functions.
- The edge has an angle of 30 degrees.
- The function for the central region has an average angle of 0.5 degree.
- At the point of about 5mm from the edge the two functions are connected smoothly. The edge is higher by 1.9 mm from the average.
- The center of the tile is lower by 0.25 mm from the average.

These two functions are used in HERMES Monte Carlo described later.

5.1.4 Measurement of position dependence of refractive index

It is generally believed that a aerogel tile has a uniform distribution of chemical structure, which means that the refractive index is almost the same at any point in a tile. However, till now there is no experimental report. It is very intresting to check that chemical assumption though it is still technically not possible to measure the absolute value of refractive index at any position of an aerogel tile directly in a very high resolution by optical method. We have measured the refractive index at the four corners of the tiles with a very high precision as discussed in the previous section. We have successed in measuring the relative refractive index by using the setup showed in Fig5.14 .

The followings are the basic points of this measurement.

- The refractive index at the four corners have been measured.

- Using the setup of Fig5.14, we can slide the aerogel tile from the corner to the central part step by step.
- The incident beam is parallel to the final refracted beam, and caused a shift, x, on the screen compared to the position of the beam without the aerogel tile.
- The shift, x is related to the refractive index of the position where the laser beam is passing.
- By measuring the shift x near the corner and other position, we can reconstruct the $\delta n = n_2 - n_1$.

Fig5.15 shows the result of the measurement. We also evaluted the error as 2.3×10^{-3}. This is larger than that of the corner, 1.6×10^{-4}. The conclusion is that the position dependence of the refractive index is not obvious within the errors. Thus we do not include this effect to our Monte Carlo. In fact, if it is included into the Monte Carlo, huge computer resources will be required to carry on the HMC.

5.1.5 Measurement of transmission and reflection

The degree of trasmission of the aerogel tile will influence the photon yield, while the reflection will influence the direction of the generated photons.

We use the setup as shown in Fig5.16 to measure the transmission and reflection. The laser is the same as was used for the measurement of the refractive index, while the screen has been replaced with a CCD camera connected to a computer. This measurement is analysed by using a software package called HALCON. Fig5.17 and Fig5.18 show the result of transimision and reflection. The measured result is analyzed by fitting with functions.

5.2 Summary of the measurements

- All the 1120 aerogel tiles were measured for their refractive idex and dimension.
- The refractive index and dimesion were recorded in a table which was the basis of selecting and installation aerogel tiles for the RICH.
- Reliability check was done for the measurement of the refractive index and dimension.

- The surface shape was measured for sample tiles.
- The measured surface shape was fitted with two functions.
- The position dependence of refractive index was also studied.
- The relationship between refractive index and temperature was also studied.
- The transmission and reflection were measured for sample tiles. The measured value was compared and was found that it is very near to the theoretical value.

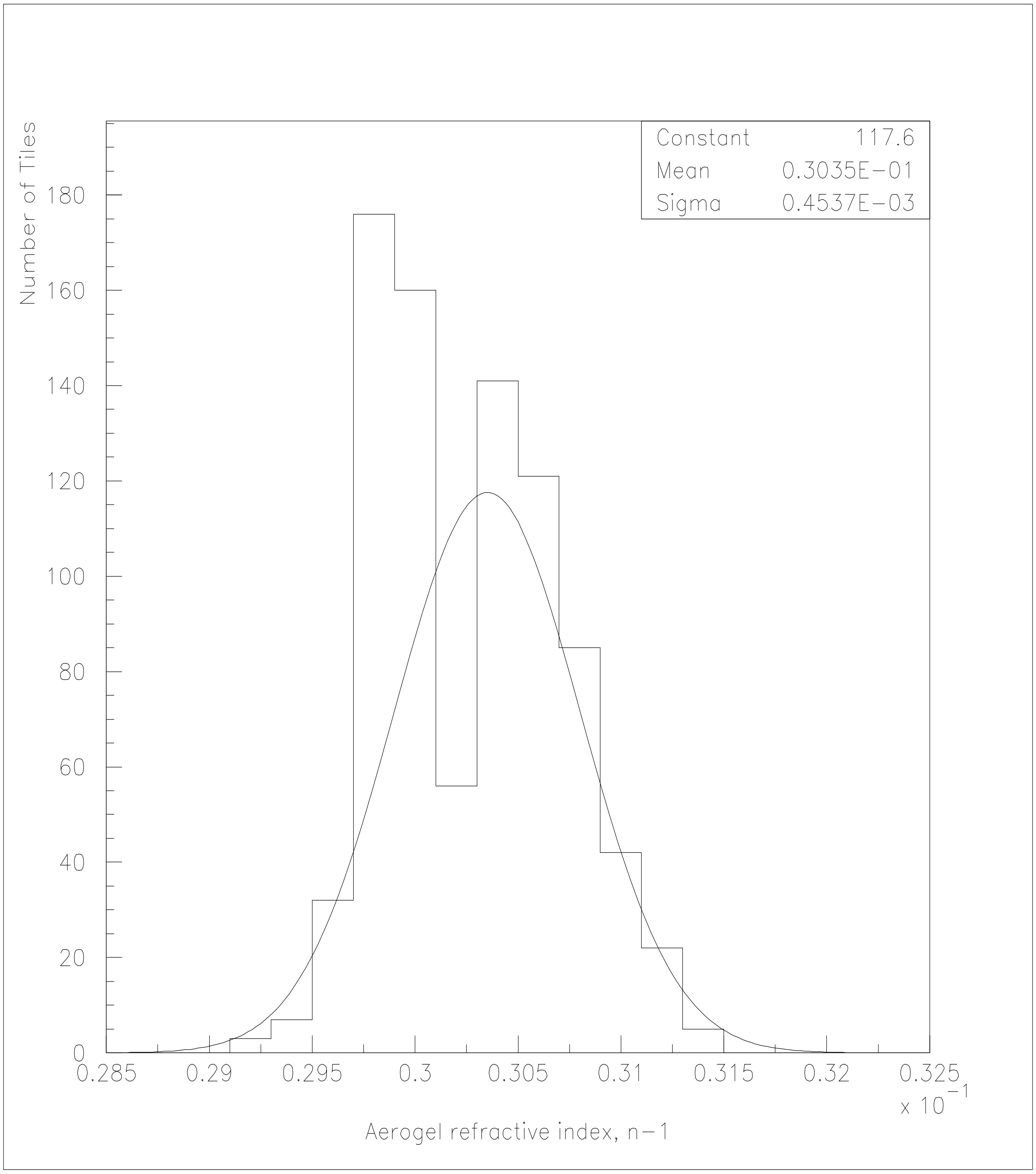

Figure 5.5: Distribution of the refractive index n-1 of the aerogel tiles .

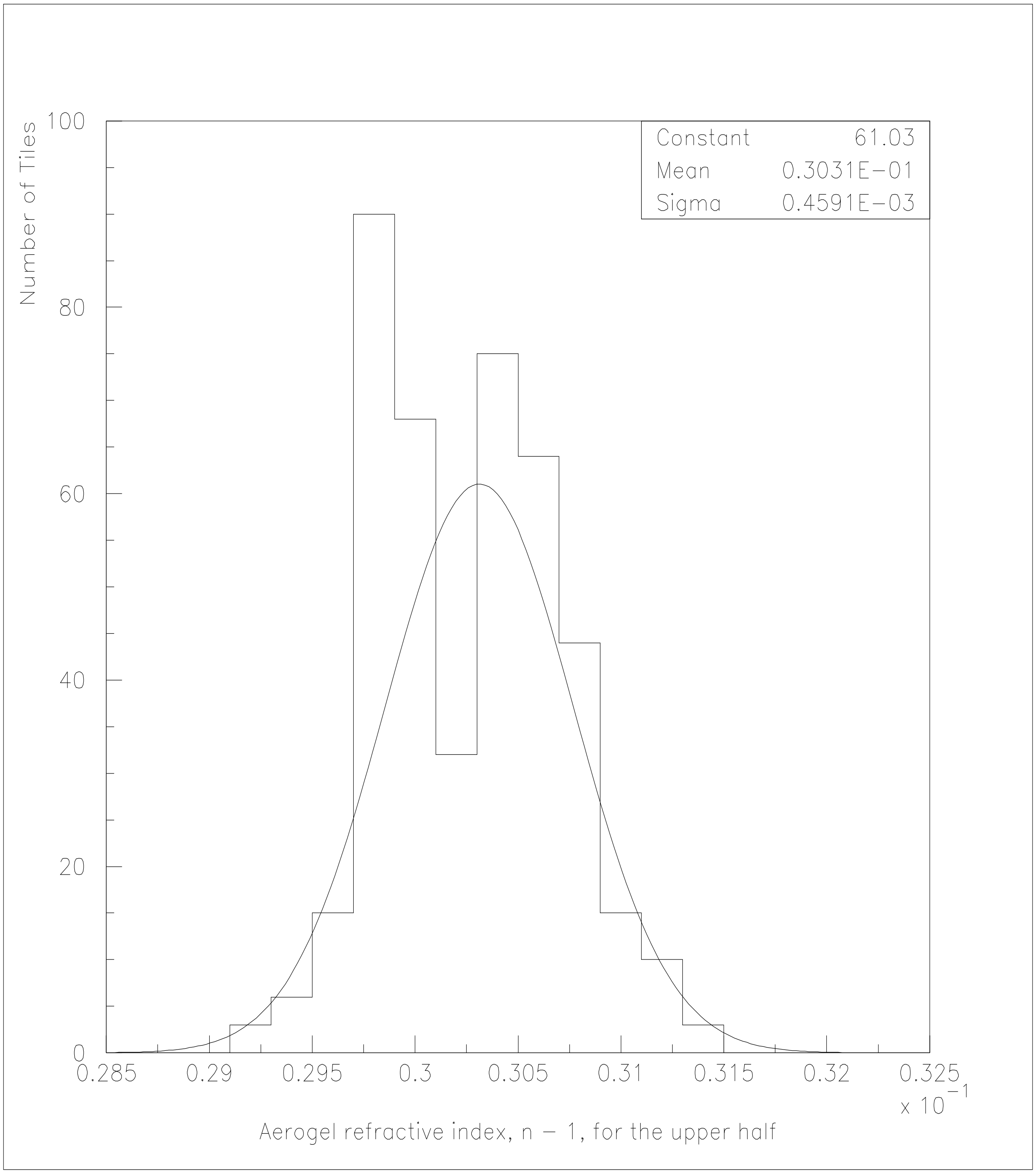

Figure 5.6: Distribution of the refractive index n-1 of the aerogel tiles for the upper half

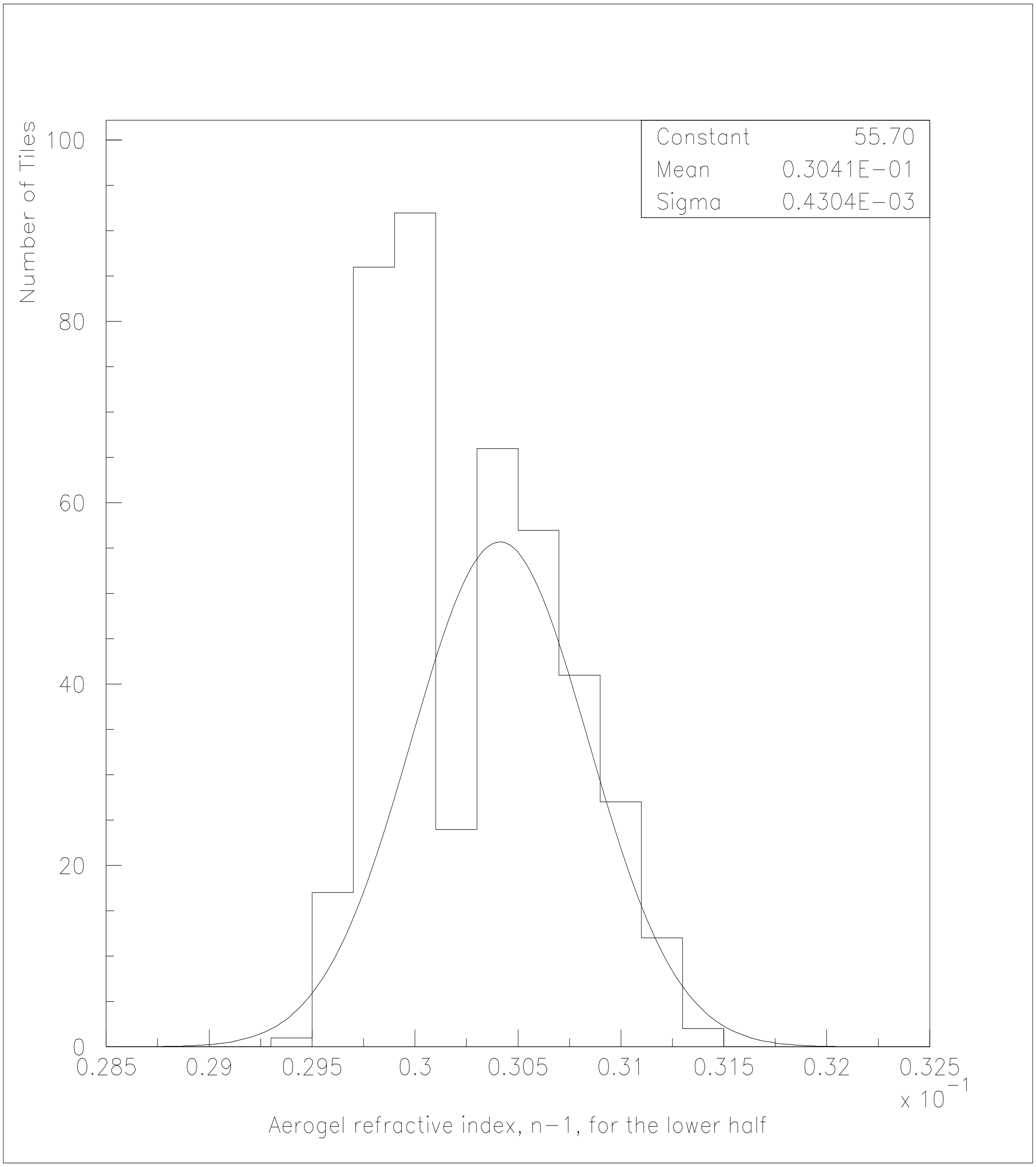

Figure 5.7: Distribution of the refractive index n-1 of the aerogel tiles for the lower half.

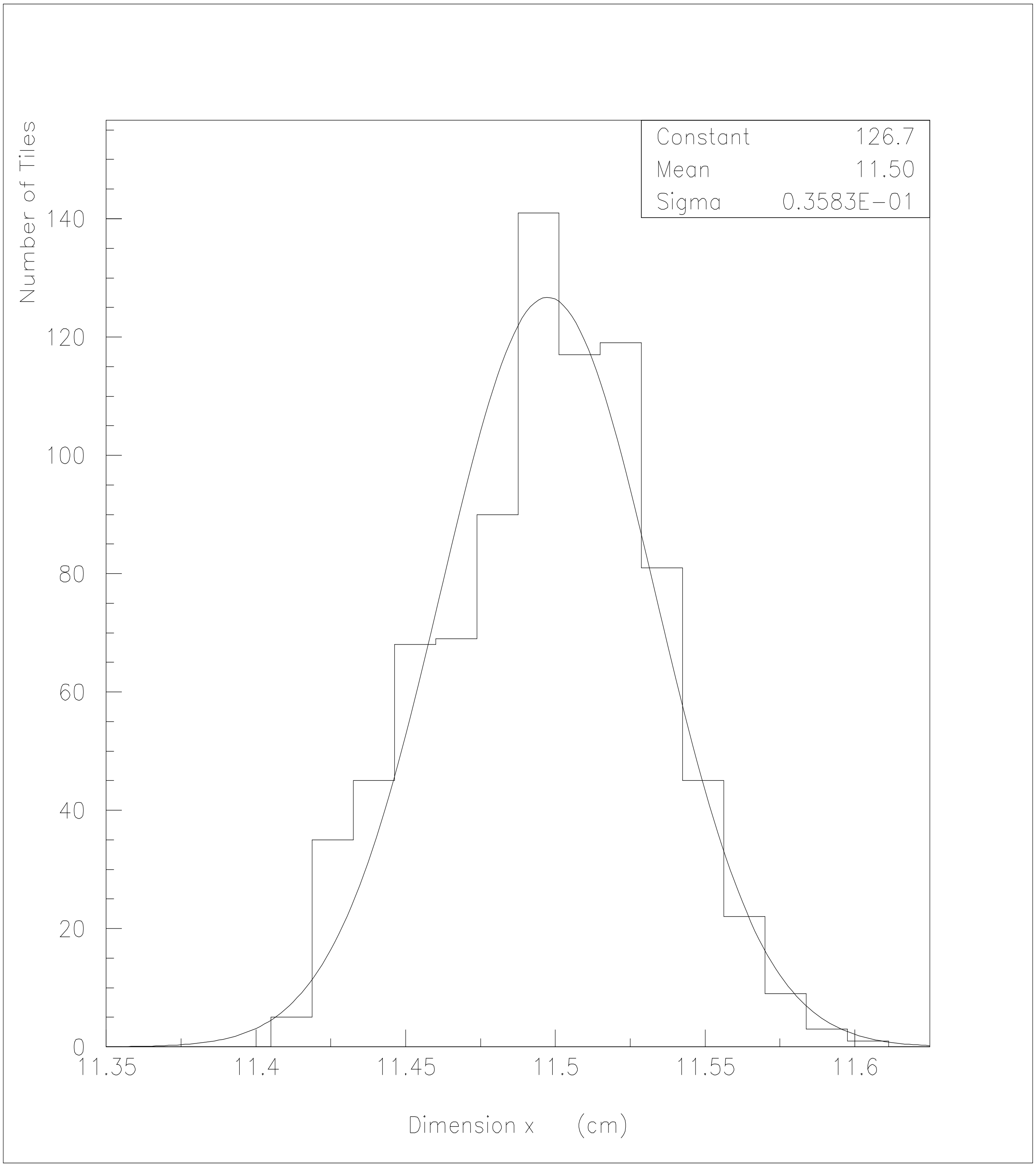

Figure 5.8: Distribution of the x dimension of the aerogel tiles.

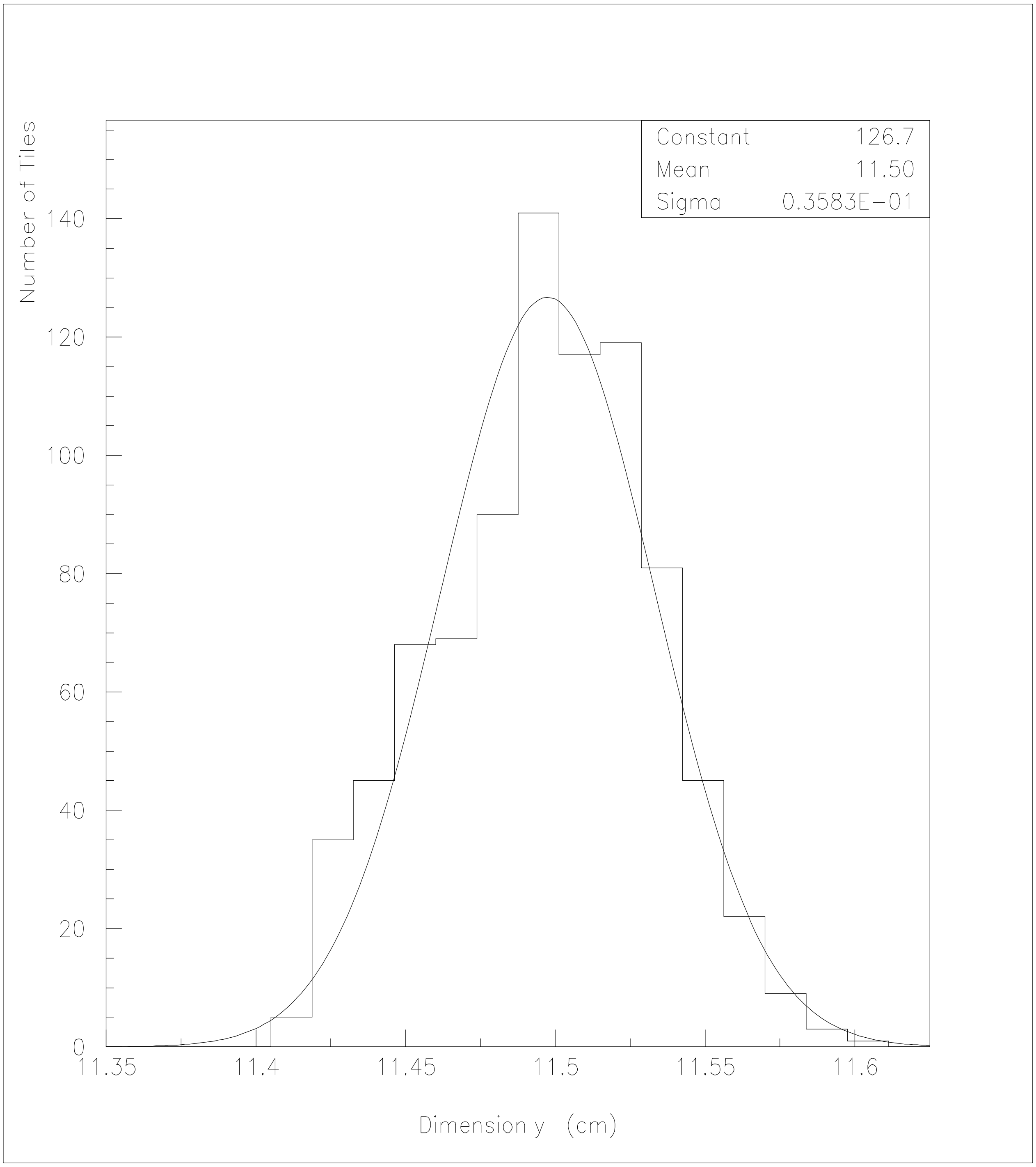

Figure 5.9: Distribution of the y dimension of the aerogel tiles.

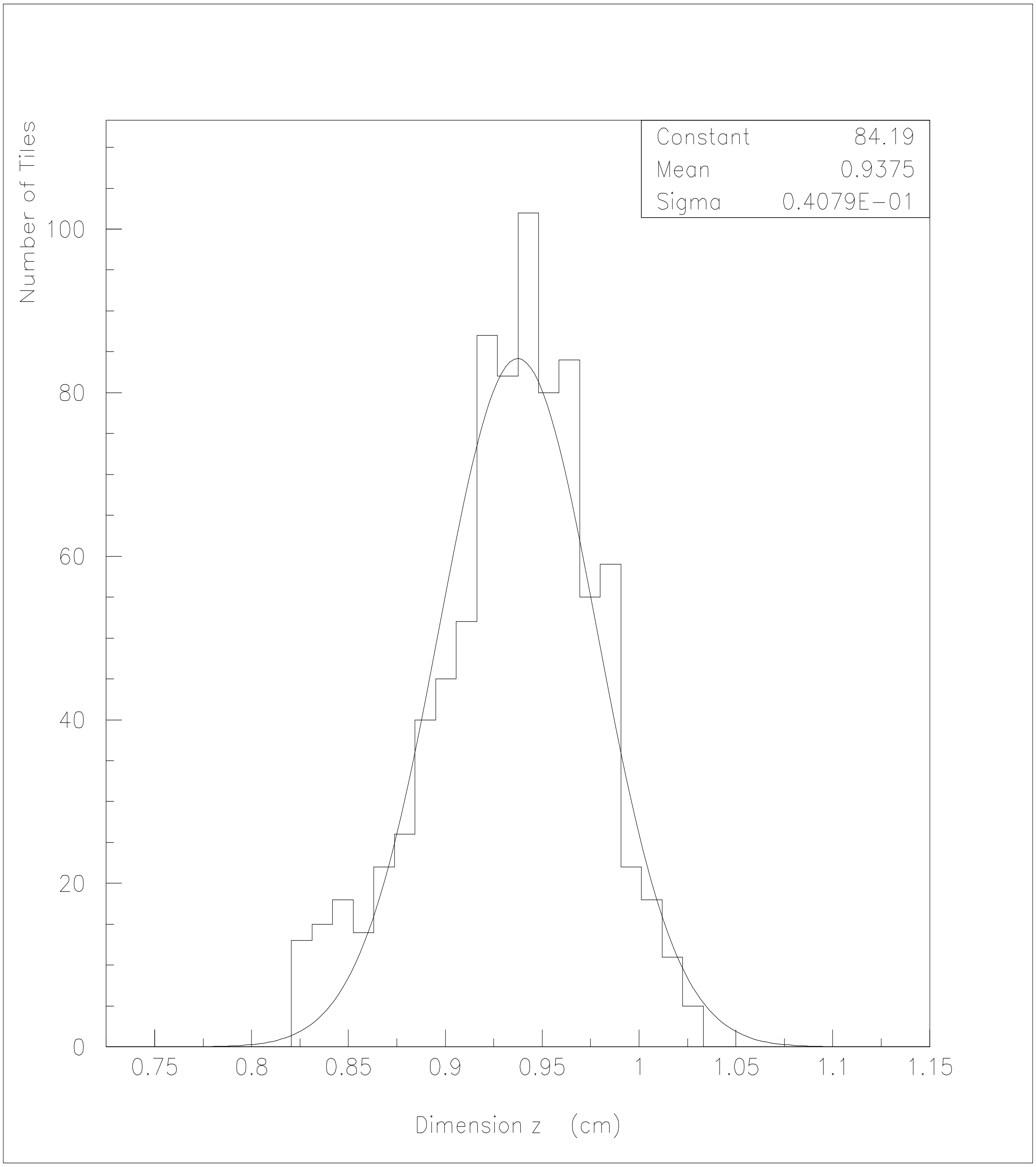

Figure 5.10: Distribution of the z dimension of the aerogel tiles.

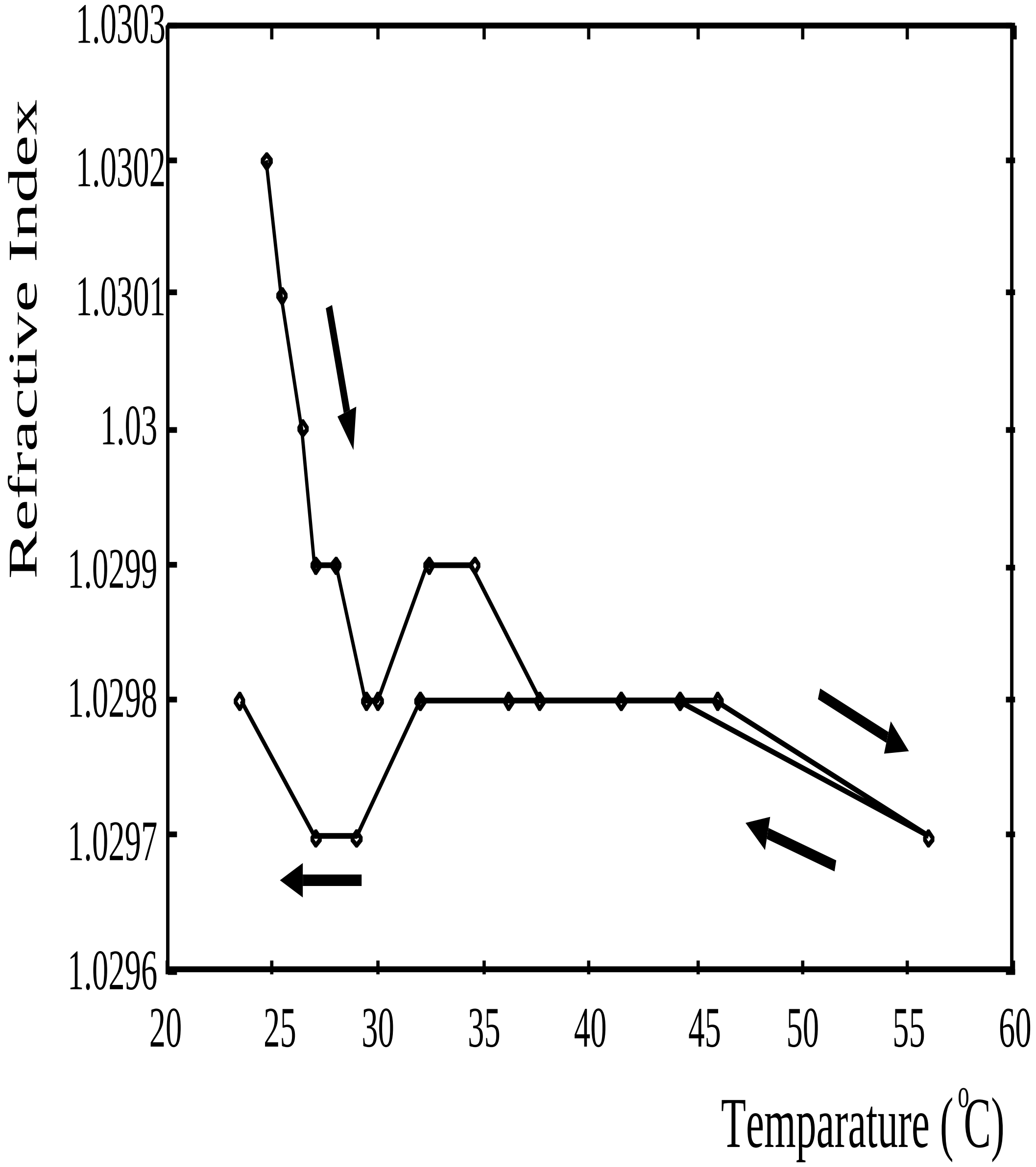

Figure 5.11: Temperature dependence of refractive index.

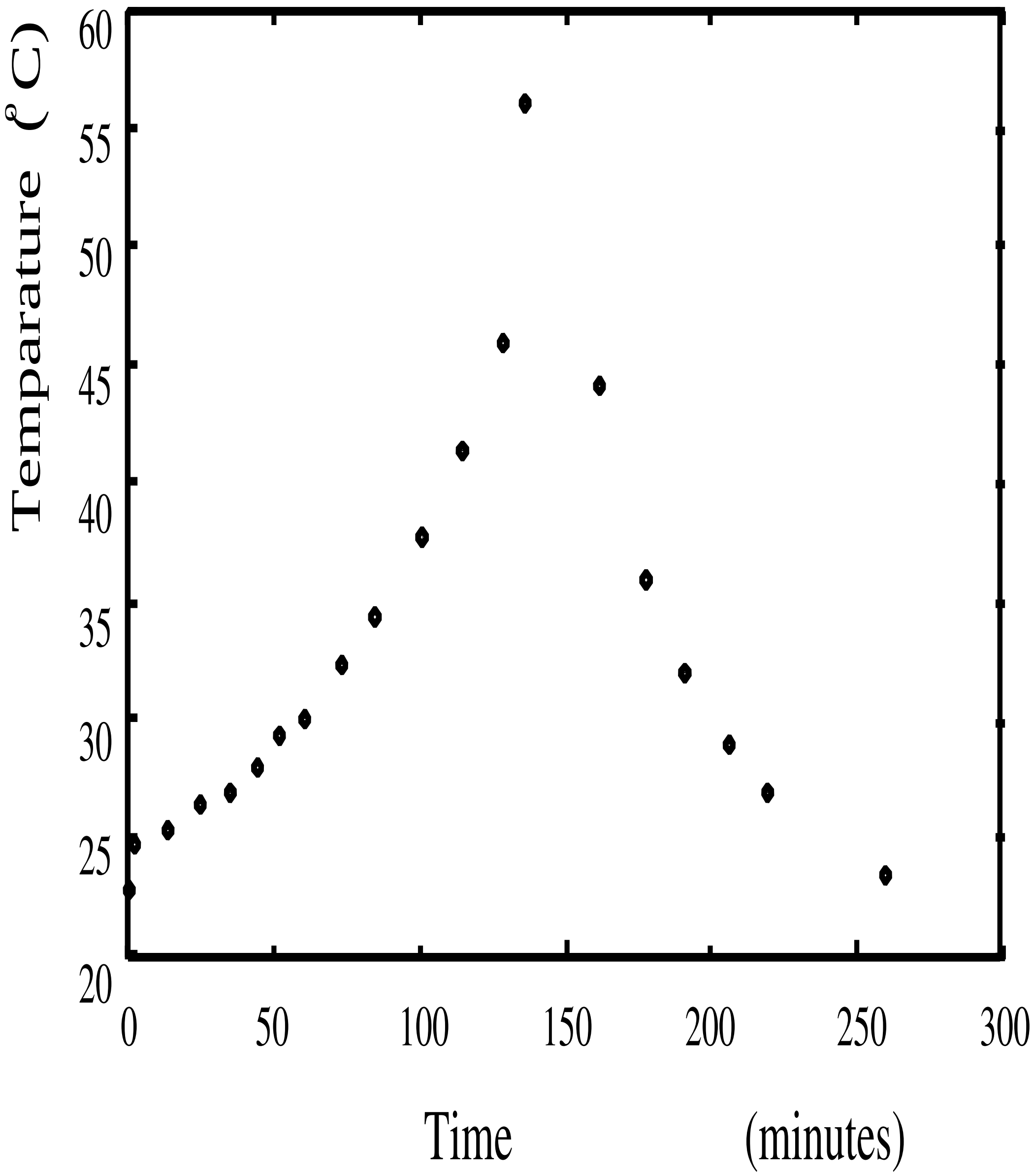

Figure 5.12: Temperature vs time in the measurement of temperature dependence.

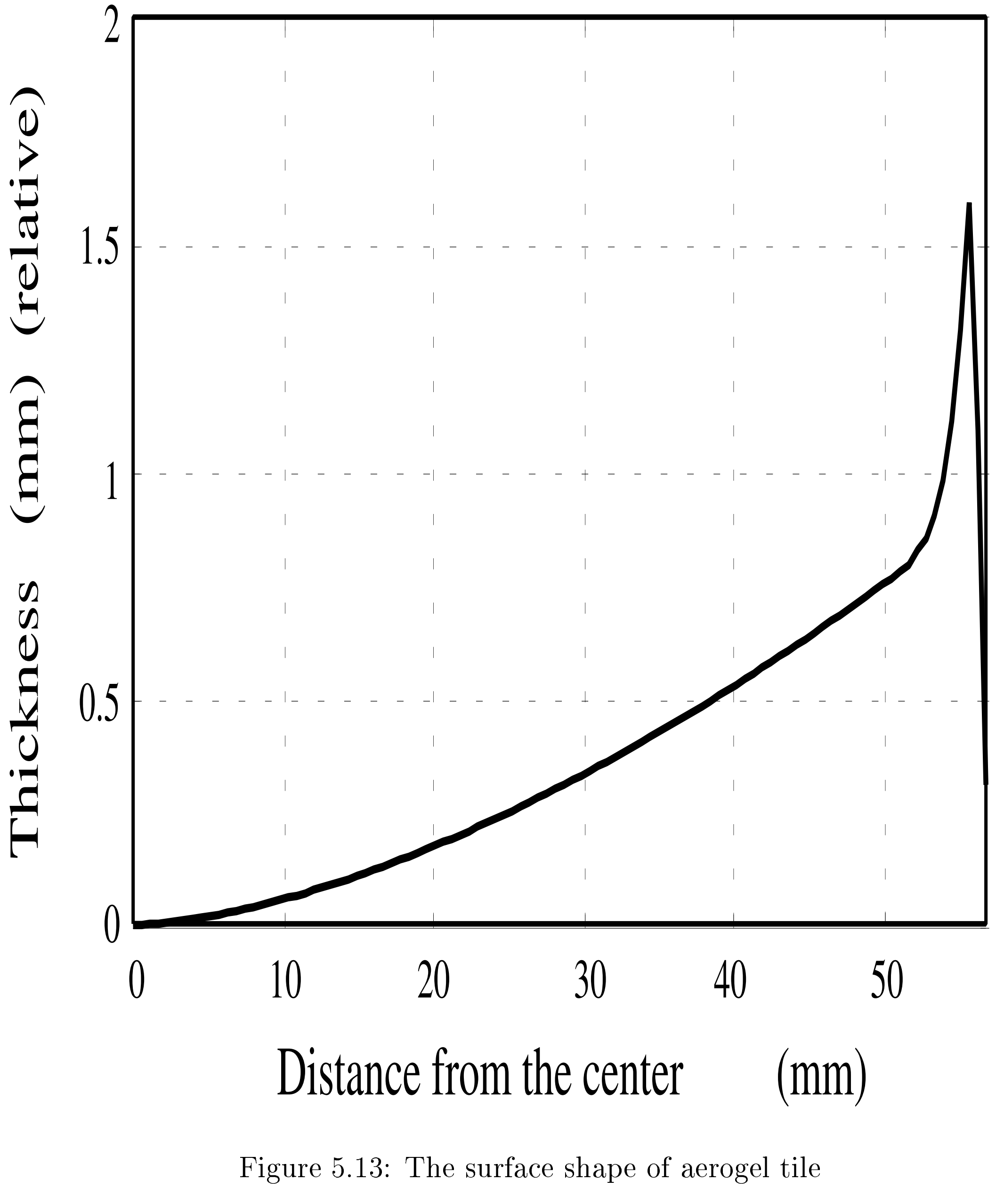

Figure 5.13: The surface shape of aerogel tile

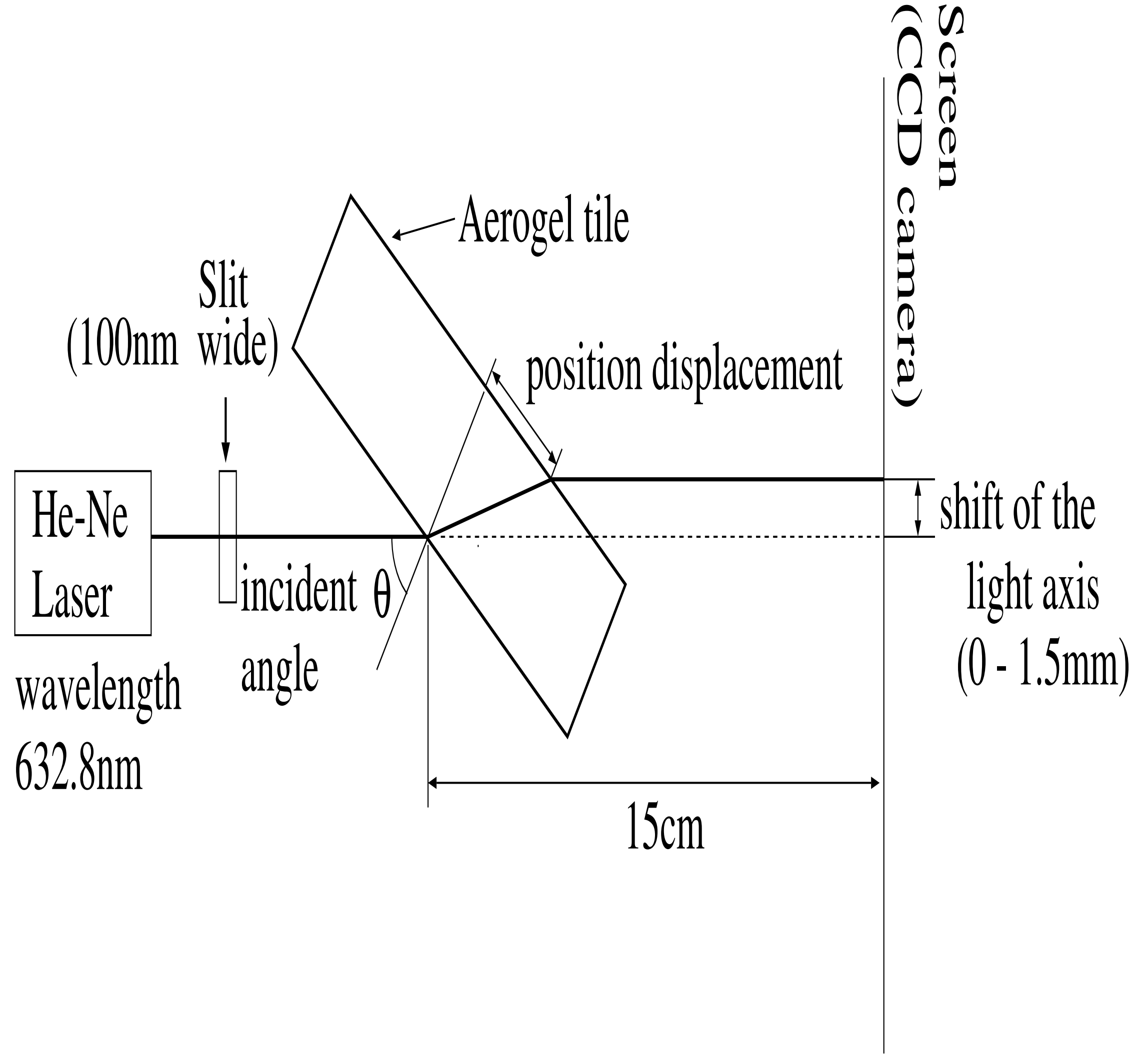

Figure 5.14: Measurement of position dependence for refractive index

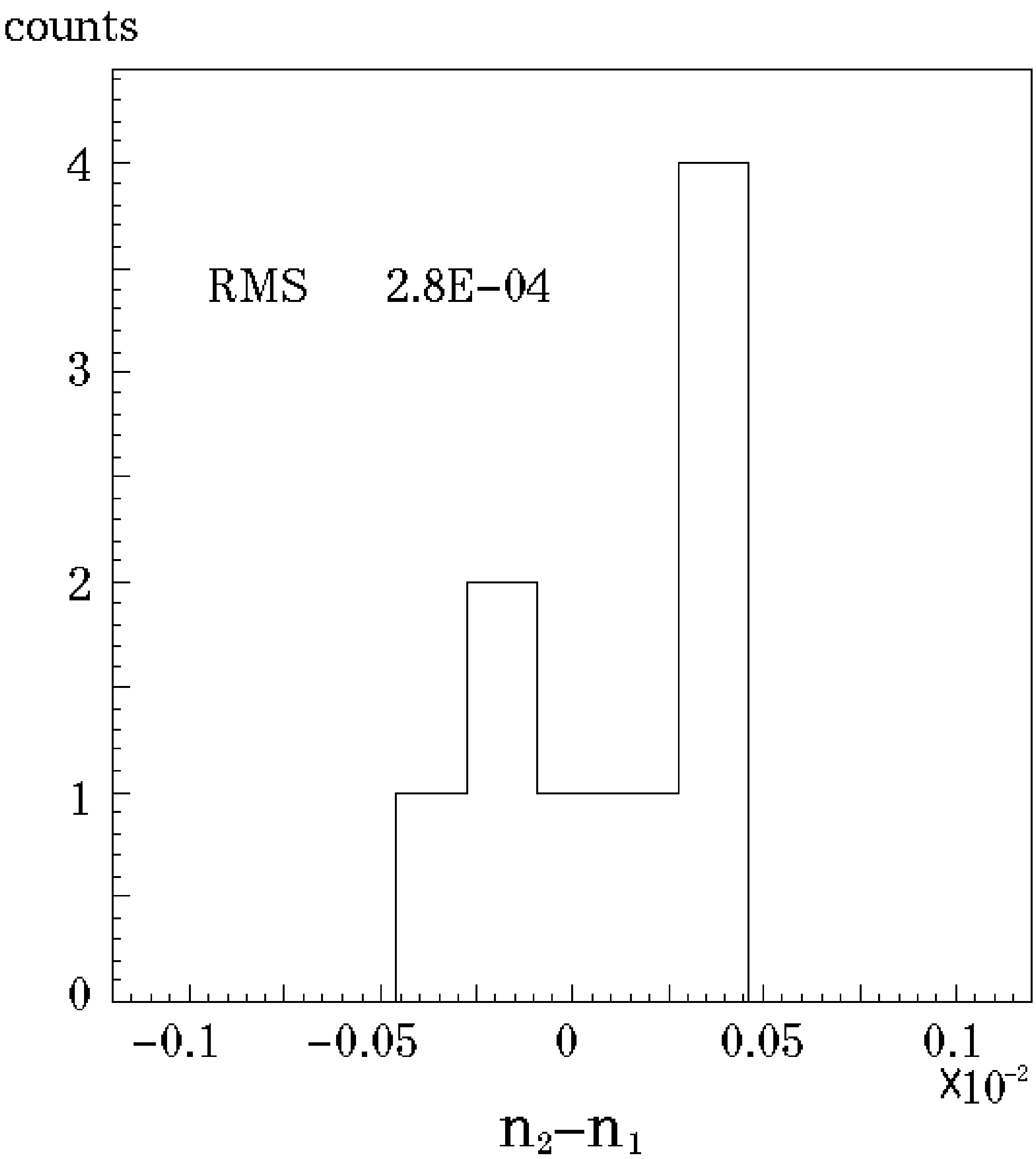

Figure 5.15: Result of position dependence for refractive index

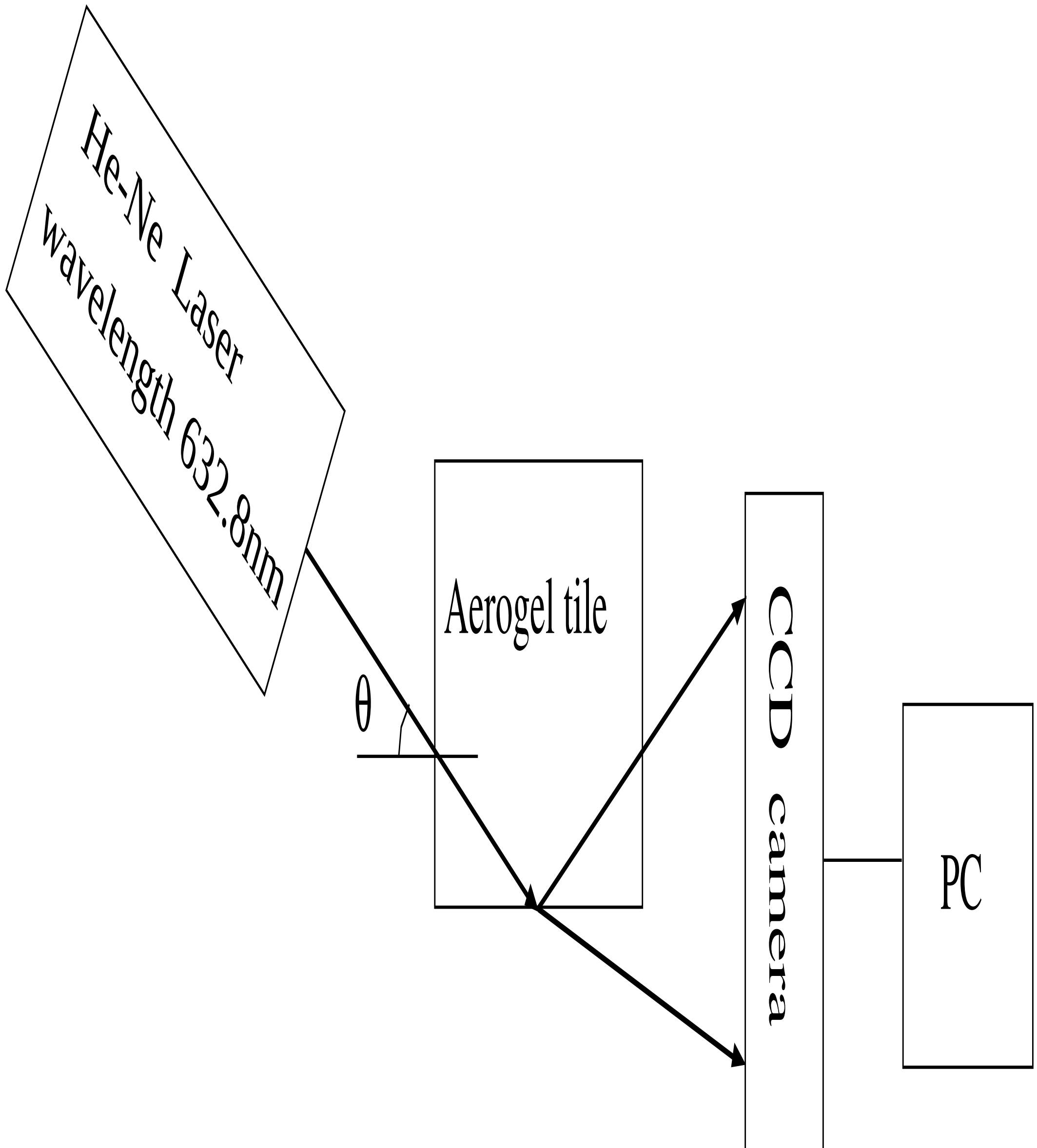

Figure 5.16: Schematic setup of the measurement of inner-side reflection

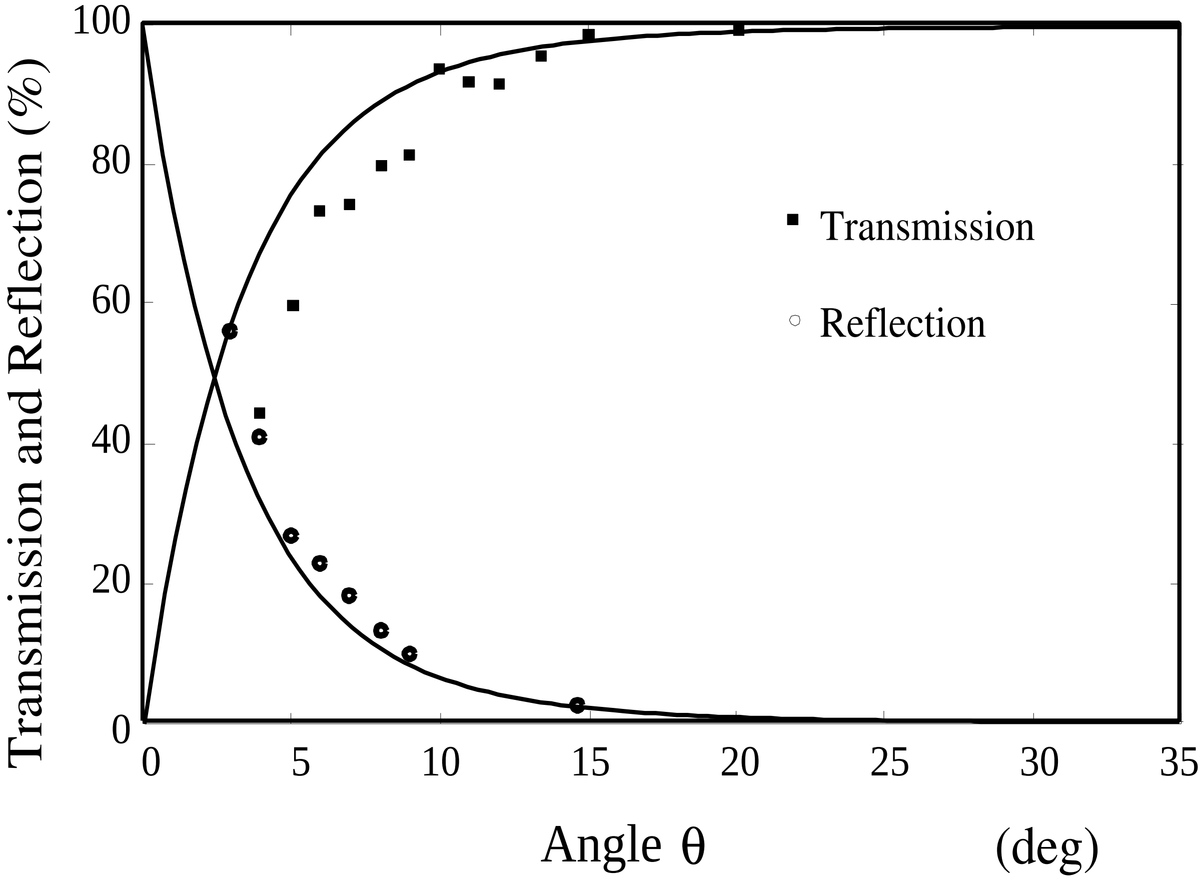

Figure 5.17: Measurement of transmission and outer-side reflection

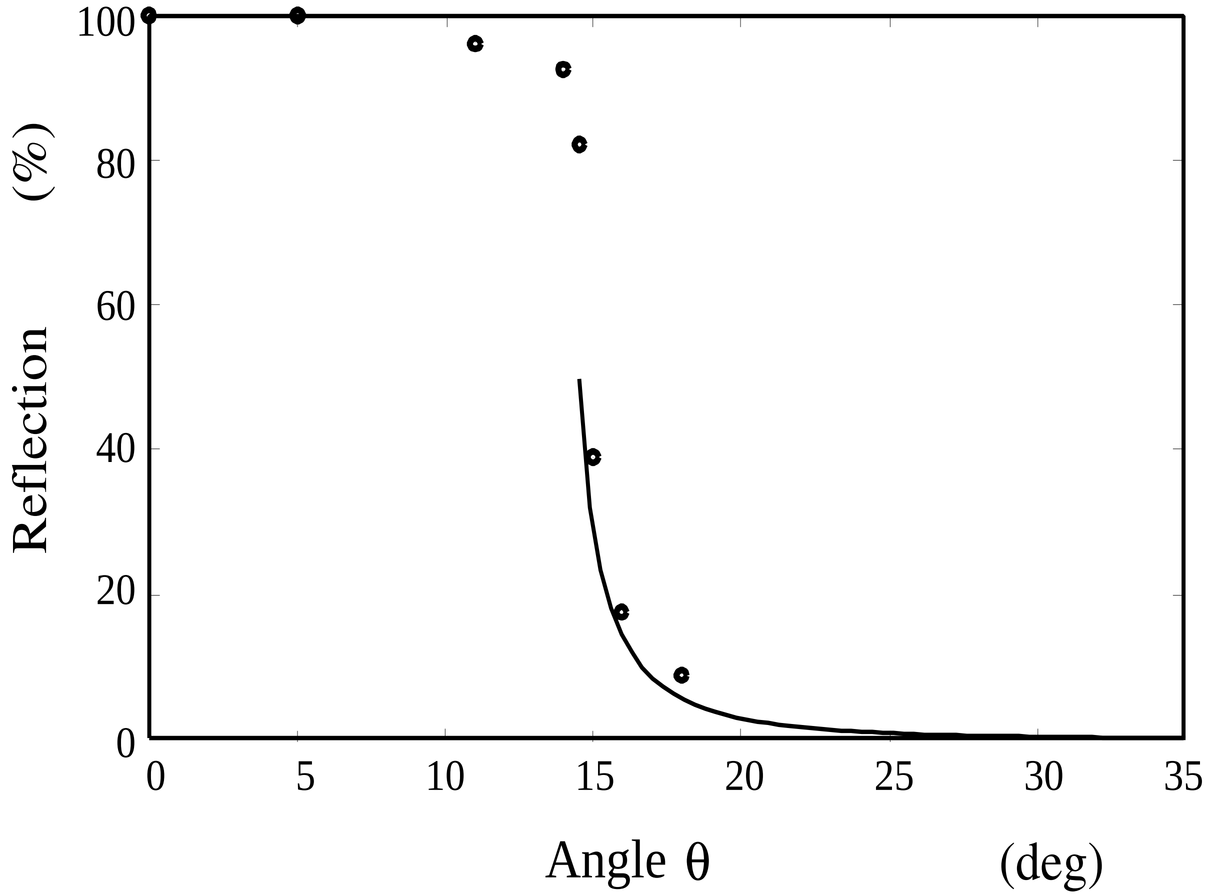

Figure 5.18: Measurement of inner-side reflection

6 Monte Carlo for RICH

The HERMES Monte Carlo(HMC) is based on GEANT[GEANT93], a system of detector and physics simulation routines available from CERN. Like other HERMES software, it also relies on ADAMO, another CERN software package, to supply data structures for the information it reads in and writes out. Most of the input files for HMC are so called ADAMO GAF(Generic Adamo File) format, as are the primary output files. To examine and manipulate the output oof HMC, it needs to read in an ADAMO GAF and translate the information into PAW histograms and ntuples which can be analyzed: placing cuts, making correlations, performing calculations and plotting. This translation service is provided by HEP, the HERMES Event Processor.

This chapter starts with an introduction of HERMES Monte Carlo.

6.1 Introduction of HERMES Monte Carlo

As most of other simulation systems, HMC needs some input files, and run over with some output files which all the simulation results are written in. Here are the list of input and output files of HEREMS Monte Carlo.
The essential input files are:

- hmcdg.ie(GEOM): The geometry GAF, containing a complete description of the detector.
- hfield.bmap: Binary file describing the HERMES magnetic field.
- hmctrspec.ie(TRSP): A GAF containing information specific to the TRD.
- hmcset.rz, hrcnewset.rz: Binary GAF's containing descriptions of the ADAMO data structures used internally by HMC.
- hmc.dic: The ADAMO dictionary file, again containing descriptions of necessary ADAMO data structures. If HMC cannot find the two rz files, it will construct them using the information in hmc.dic.

- SLT.ie(SLTT): An ADAMO GAF containing values needed by the second level trigger.
- hmc.digi(DIGI): This file contains all of the parameters used by the detector digitization routine.

Output files are:

- hmc.events(EVEN): This is the primary output of HMC. It is a GAF file containing data from almost all of the tables used by HMC, for each generated event.
- hmc.hbook(HBOOK): If the HBOOK option is set, this HBOOK file will be written out, containing a number of histograms. The choice of stored histograms is controlled by various other HMC options. This file can be read in and analyed by PAW.
- hmc.tuple(TUPL): A number of options control whether or not an HBOOK file will be booked by HMC, and what information will be stored in the ntuple...if this utility is required, the results are written to the hmc.tuple HBOOK file.
- hmc.ps(META): With the hermes/metafile command, we can open a postscript file of this name to which all displayed graphics will be logged.

Geometry file will be the first file encountered, if we want to simulate some events with HERMES Monte Carlo. In HMC, the geometry is in order. The detector is composed of GEANT volumes, each with its own 4 character name. The volumes themselves are simply geometric objects of a certain shape and size: spheres, boxes, tubes, etc. However, each volume is also associated with a tracking medium. GEANT knows about many materials automatically, also we can define as many more as we want by specifying their density, radiation, length, etc.

We can define mixtures of predefined materials as well. With these materials, we can then define tracking. Volumes, with their associated tracking media, are then positioned somewhere in space, several copies of the same volume can be put in different places. Similarly, GEANT knows automatically about many different particles. We can also define others. For example, we have defined one special particle type : the non-interacting electron. This is a ficitious particle which has the mass and charge of an electron, and will be properly deflected in the magnet. However, it will not interact with any of the materials it encounters. It won't lose energy, produce secondary particles, or be deflected by multiple scattering.

With the geometry and particles being defined, we can define a generator. This routine is user written. For every event, it randomly generates the kinematics of the primary vertex. HMC has several generators installed, for example deep inelastic scattering(DIS). This routine generates events in the variables Q^2 and ν according to the DIS cross-section, and produces a random azimuthal angle phi. These kinematics are then handed to a LUND program which determines the hadrons produced at the vertex for DIS event, based on models of the parton distribution functions. All of the particles are then handed to the GEANT tracking stack, instructing GEANT to follow these particles cm by cm through the detector and its materials, checking interaction cross-sections at each step to see if the particles lost energy, were scattered, or produced additional particles. If secondary particles are produced, they are also placed on the tracking stack and followed through the detector.

At each step in the tracking, GEANT is able to figure out what volume and material the current particle is passing through. The concept of mother and daughter volumes is essential here. The daughter volume is always in the mather volume and always takes precedence over the mother volume.

Then finally, by declaring some volumes as sensitive detectors. HMC can simulte some detector response. When a particle enters a sensitive detector, the Monte Carlo notes this and keeps track of information such as the total amount of energy it deposits in that volume and the entry and exit position of the track. This information is recorded as a hit in the affected sensitive detector. Sometimes, one hit per track is stored. Sometimes the information from all hits in a single volume is combined into one hit per event.

The following is the basic program list of GEANT.

MAIN	user routine
· GZEBRA	initialization of ZEBRA, dynamic core allocation
· UGINIT	user routine
·· GINIT	initialization of GEANT variables
·· GFFGO	interpretation of data records
·· GZINIT	initialization of ZEBRA core divisions and link areas
·· GPARTGSPART	creation of the *particle* data structure JPART
·· GMATEGSMATE	creation of *materialdata* structure JMATE
·· *usercode*	description of the geometrical setup, of the sensitive detectors,creation of data structures JVOLUM, JTMED, JROTM, JSETS
·· GPHYSI	preparation of cross section and energy loss tables for all used materials
· GRUN	loop over events
·· GTRIGI	initalization for event processing
·· GTRIG	event processing
· · · GUKINE	user generation of event initial kinematics
· · · GUTREV	user define
· · ·· GTREVE	loop over tracks,including any secondaries generated
· · · · · GUTRAK	user define
· · · · ·· GTRACK	control tracking of current track
· · · · · · · GFINDS	find current volume in the geometry tree
· · · · · · · GUSTEP	recording of hits in data structure JHITS and of space points in data structure JXYZ
· · · · · · · GUPARA	called if the particle falls below the tracking threshold
· · · · · · ·· GTGAMA ·	tracking of particle according to type
· · · · · · · GFSTAT	fill banks for volume statistics
· · · · · · · GSTRAC	store information of the current rtrack segment
· · · · · · · GUSTEP	recording of hits in data strure JHITS and of space points in data structure JXYZ
· · · · · · · GTMEDI	finds in which colume medium the current space point is
· · · · · · · GUSTEP	recording of hits in data strure JHITS and of space points in data structure JXYZ
· · · GUDIGI	computation of digitisation and recording in data structure JDIGI
· · · GUOUT	output of current event
·· GTRIGC	clearing of memory for next event
· UGLAST	user define
·· GLAST	standard GEANT termination

6.2 RICH Monte Carlo

The existing HERMES Monte Carlo system(HMC) cannot simulate the new RICH system. It is needed to be updated to a new version of HMC which can simulate the dual aerogel-gas ring imaging system. This section will mainly introduce Monte Carlo of aerogel optical properties and finally, the mirror system. We have measured the properites of the aerogel tiles such as refractive index, size dimensions, transmission and reflection etc. as is described in the previous chapter. The next step is to study these effects by modifying or updating the existing HMC source programs. Here is the overlook of the updated parts for aerogel study in HMC, see also Fig6.1.

6.2.1 Aerogel dimension

A easy way to simulate the aerogel is just to define a very big aerogel wall with its refractive index n = 1.03 in the geometry file. In the Monte Carlo code, we first define the aerogel radiator as a whole piece for simulation. This is the most ideal case in our Monte Carlo process(see Fig6.3).

The second step is to use the actual size of the tiles in the Monte Carlo. As mentioned above, we have the properties of all the tiles. We use the tile dimension to update the HMC code. Fig.6.2 shows this algorithm. By using the RICH-viewer, we can see now the whole aerogel wall has been seperated into many tiles (850 tiles as we installed in the rich box).

Fig6.4, Fig6.5 and Fig6.6 show the aerogel wall before the aerogel tiles geometry is included. Fig6.7, Fig6.8 and Fig6.9 show the aerogel tiles after tile geometry is included in HMC.

6.2.2 Aerogel refractive index

The Aerogel refractive index is directly related to the Cerenkov angle. Since we use 850 aerogel tiles, whose refractive index is between 1.029 to 1.032, it is necessary to include the refractive index to the HMC. By using an inclusive refractive index file in the HMC source code, we include all the refractive index to the program.

We have measured the refractive index of all the aerogel tiles, each tile has its own properties: refractive index, size dimension. We also know where each tile is positioned in the RICH box. By using these two tables, we create a new table corresponding to the actual relationship of the aerogel refractive index and its position in RICH. From this table, depending on the GEANT format, we create an inclusive file for HMC, when the HMC programs want to use the aerogel tile, it will get the properties from the inclusive file and other necessary information from the pre-defined geometry file. In running GEANT based system, we defined 850 volumes for the aerogel tiles in the geometry file.

Fig6.9 and Fig6.10 show the Monte Carlo view of a DIS event of HMC after the tiles geometry is included in the programms.

6.2.3 Light scattering

The ideal aerogel tile has a flat surface. As our aerogel has a non-flat surface, the Cerenkov photon will change its direction when it is passing through the aerogel surface. We have fitted the surface with two functions and create a subroutine called 'ggperp' for this effect, as the following:

- GEANT knows where the track of the photon is now.
- If the track is passing through the surface of aerogel, the default GEANT routin is modified as:
  - calculate the relative position in an aerogel coordinate of the track.
  - call subroutine 'ggperp'. It's parameter is $\vec{x}(x_1, x_2, x_3x_4, x_5, x_6)$. x_1, x_2, x_3 stand for the position, while x_4, x_5, x_6 stand for the direction.
  - the return value $\vec{x}$ from 'ggperp' will be used for the next track.
- If the track is not passing through the surface, go on as default.

6.2.4 Tile side effect and transmission and absorption

The default HMC program cannot simulate the side effect of the aerogel tiles. We measured several aerogel tile samples and, using that results, simulated the transmission and absorption. Here is two functions:

$$R = \frac{1}{2}[(\frac{n_1 \cos\theta_1 - n_2 \cos\theta_2}{n_1 \cos\theta_1 + n_2 \cos\theta_2})_s^2 + (\frac{n1 \cos\theta_1 - n_2 \cos\theta_2}{n1 \cos\theta_1 + n_2 \cos\theta_2})_P^2] \tag{6.1}$$

$$T = \frac{1}{2}[\frac{4(n_1\cos\theta_1)(n_2\cos\theta_2)}{(n_1\cos\theta_1 + n_2\cos\theta_2)^2_s} + \frac{4(n_1\cos\theta_1)(n_2\cos\theta_2)}{(n_1\cos\theta_1 + n_2\cos\theta_2)^2_P}]. \tag{6.2}$$

We used these two functions in the simulation together with the new subroutine 'ggperp'.

As for the Rayleigh Scattering, in the current version of Monte Carlo, we are using the default GEANT subroutine now.

6.2.5 Mirror alignment

The HERMES RICH uses two mirrors to reflect the Cerenkov photons, (see Fig6.10). There are two mirrors called upper mirror and lower mirror, each has eight pieces of small mirrors. These small mirrors constitute as a large sphere of mirror.

We have succeeded in dividing the mirror into 8 pieces of small mirror in the Monte Carlo code. We have also developped an easy program for creating GEANT input file in order to simulate the mirror system. Since the mirror system has several degrees of freedom, a large amount of events and patterns are required.

Here is the process for the simulation:

- 1. Use the program to create input file.
- 2. Run hdb, hmc, hrc one after another.
- 3. Run kumac file to analyze the Monte Carlo result.
- 4. Check the analyzed results, comparing the results by some predefined standards.
- 5. According to the compared result, if not satisfied, adjust the mirror parameters by some defined standards. If satisfied, exit loop.
- 6. Go to 1. to loop.
- As for the comparing standard, one of the selections is to use the experiment data, and checking its reconstructed angle.

6.3 Production of Monte Carlo and Results

Up to now we have discussed that we have modified the default GEANT routines or created new sub routines for the RICH Monte Carlo. We also defined several flags in the Monte Carlo system in order to be able to investigate each effect respectively. By switching ON or OFF these flags, rountines for the responding effect will be used or not used in the Monte Carlo. We have produced the following Monte Carlo data and analysis.

6.3.1 Aerogel wall

This production was done in the following conditions:

- Generator: Background(27.5 GeV electron).
- Aerogel shape : wall.
- Event count : 10000.

As for the analysis, we focused mainly on the Cerenkov angle by the aerogel radiator, and the angle of gas ring. Fig6.12, Fig6.13 and F6.14 are the results of the Monte Carlo production. From Fig6.12, we have the sigma value of 0.6635×10^{-2}. The sigma is the standard deviation of the Cerenkov angle. If we further restrict the particle monentum, we have the sigma value of 0.5575×10^{-2}, from Fig6.13. Fig6.14 is the distribution of Cerenkov angle from the gas. We have the sigma value 0.7328×10^{-2}.

6.3.2 Aerogel tiles with the identical refractive index

This production was done in the following conditions:

- Generator: Background(27.5 GeV electron)
- Aerogel shape: tiles, but with identical refractive index 1.03.
- Event count: 10000.

This production is different from the first one. We have changed the aerogel wall radiator into the 850 tiles of aerogel. In order to investigate the difference from the above one, we set identical refractive index for all the aerogel tiles, that is 1.030.

From Fig6.15 we can find the slight difference of the sigma value from the aerogel wall radiator. The sigma becomes to 0.6691×10^{-2} while for the aerogel wall, 0.6635×10^{-2}.
We can also see the sigma from the gas is almost the same (0.7319×10^{-2} and 0.7328×10^{-2}). We change nothing for the gas radiator.

6.3.3 Aerogel tiles with the identical refractive index and with light scattering

This production was done in the following conditions:

- Generator: Background(27.5 GeV electron)
- Aerogel shape: tiles, with identical refractive index 1.030.
- Light scattering flag: ON.
- Event count: 10000.

The difference between the above one is that we set the light scattering flag ON, which means that the surface structure is consindered in the production.

Fig6.18 and Fig6.19 show the Monte Carlo results. We can see that the sigma is now 1.067×10^{-2}, which is larger than the above one. That is to say, the light scattering has an relatively large impact on the Cerenkov photon path.

6.3.4 Aerogel tiles with the real refractive index and with light scattering

This production was done in the following conditions:

- Generator: Background(27.5 GeV electron)
- Aerogel shape: tiles, with real refractive index.
- Light scattering flag: ON.
- Event count: 10000.

The aerogel tile is separated by a material called tedlar. We simulated the surrounding effect and light scattering effect, and include all the real refractive index in this production which is very near to the real situation of the RICH box.

Fig6.21, Fig6.22 and Fig6.23 show the result where we now have the sigma as 1.082×10^{-2}.

6.3.5 Comparison MC results with experiment data

HERMES has taken real ring from the new RICH, it is reconstructed by the current system. The ring is shown by monitor, another package called "eve", see Fig6.11.

With the progress of Monte Carlo, it becomes possible to compare the Monte Carlo results with the experiment data. First we will compare the photon yield of the aerogel radiator. In Fig6.24, the top-left plot shows the photon yield of the experiment data. The Monte Carlo result is the top-right one. The bottom plot is the ratio of the above two. We can see the ration is very near to 1. That is to say, the Monte Carlo has a good simulation in the photon yield of the aerogel raditor.

Second we will compare the distribution of Cerenkov angle. Fig6.25 shows the comparison. The dash curve is the experiment data while the solid curve is from Monte Carlo. The two curves look very similar. It means that the Monte Carlo has successfully simulated the real RICH environment.

The Experiment data has reached a single photon resolution of 12.6 mrad. As for the ring resolution, the new RICH system has a value of 3.6 mrad.

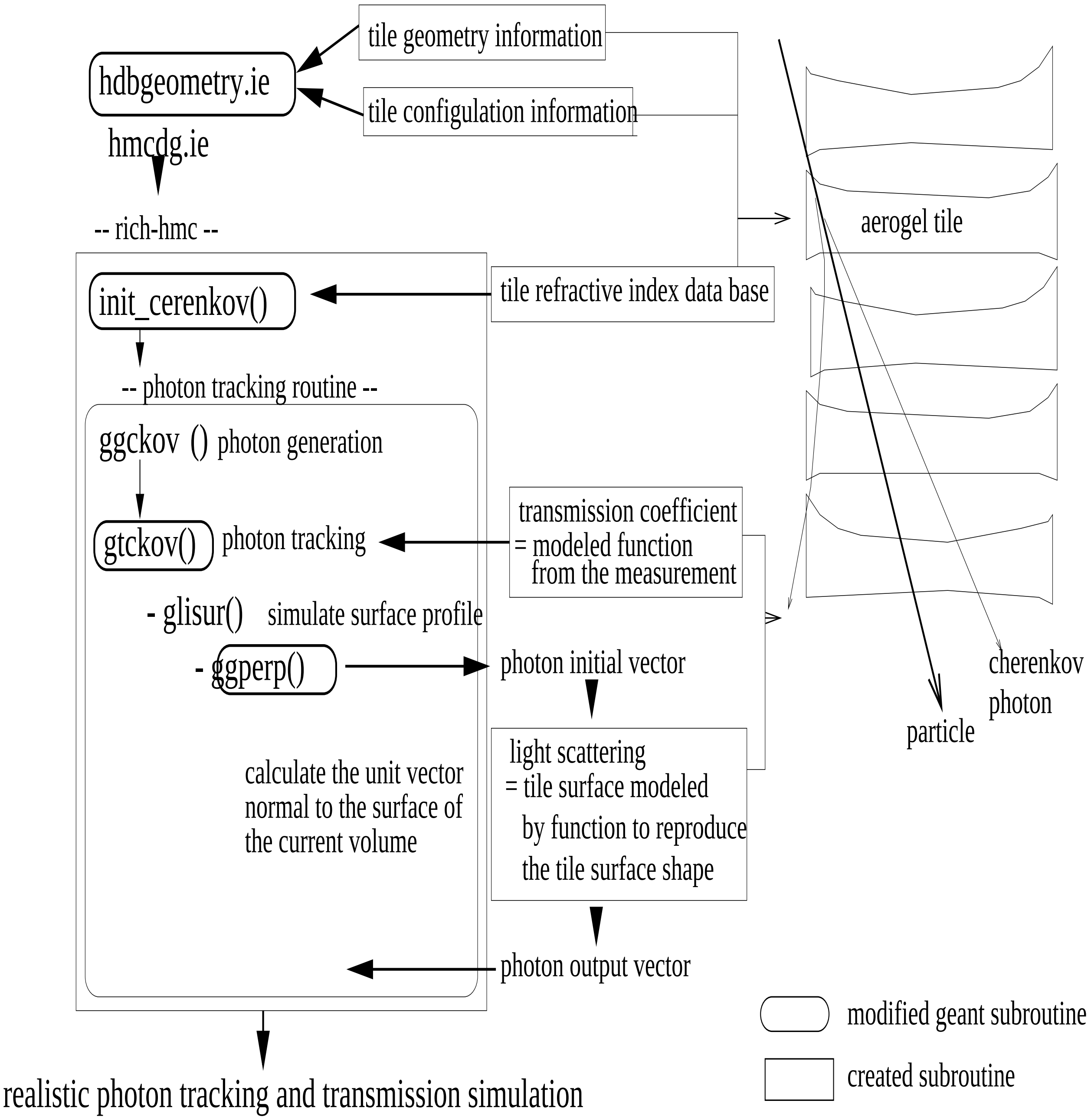

Figure 6.1: RICH-HMC flow chart for aerogel study.

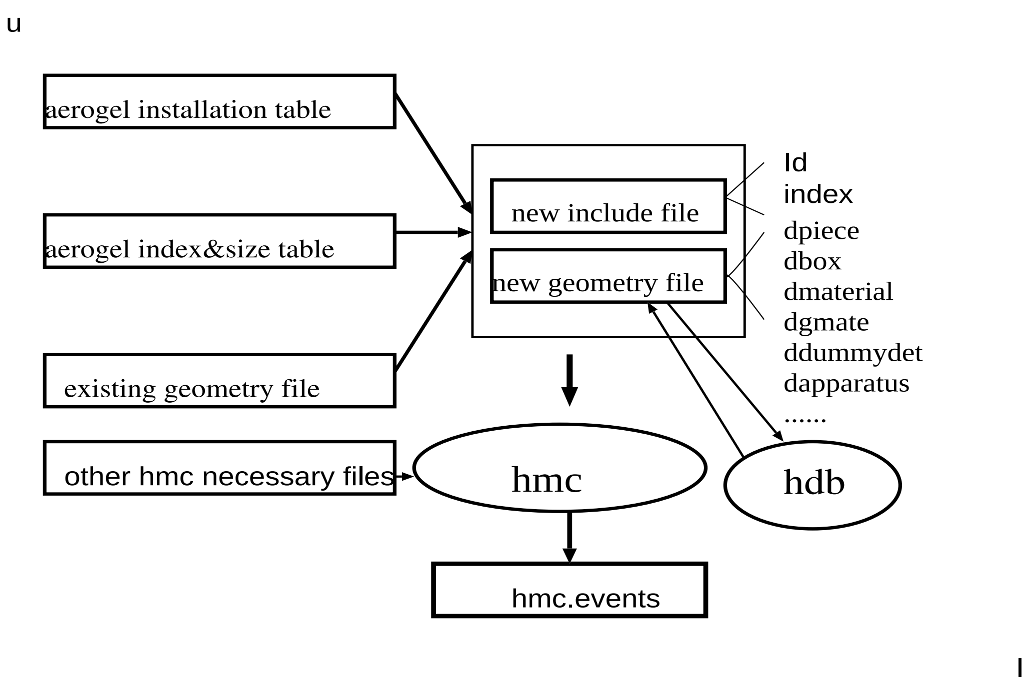

Figure 6.2: HMC flow for refractive index and size.

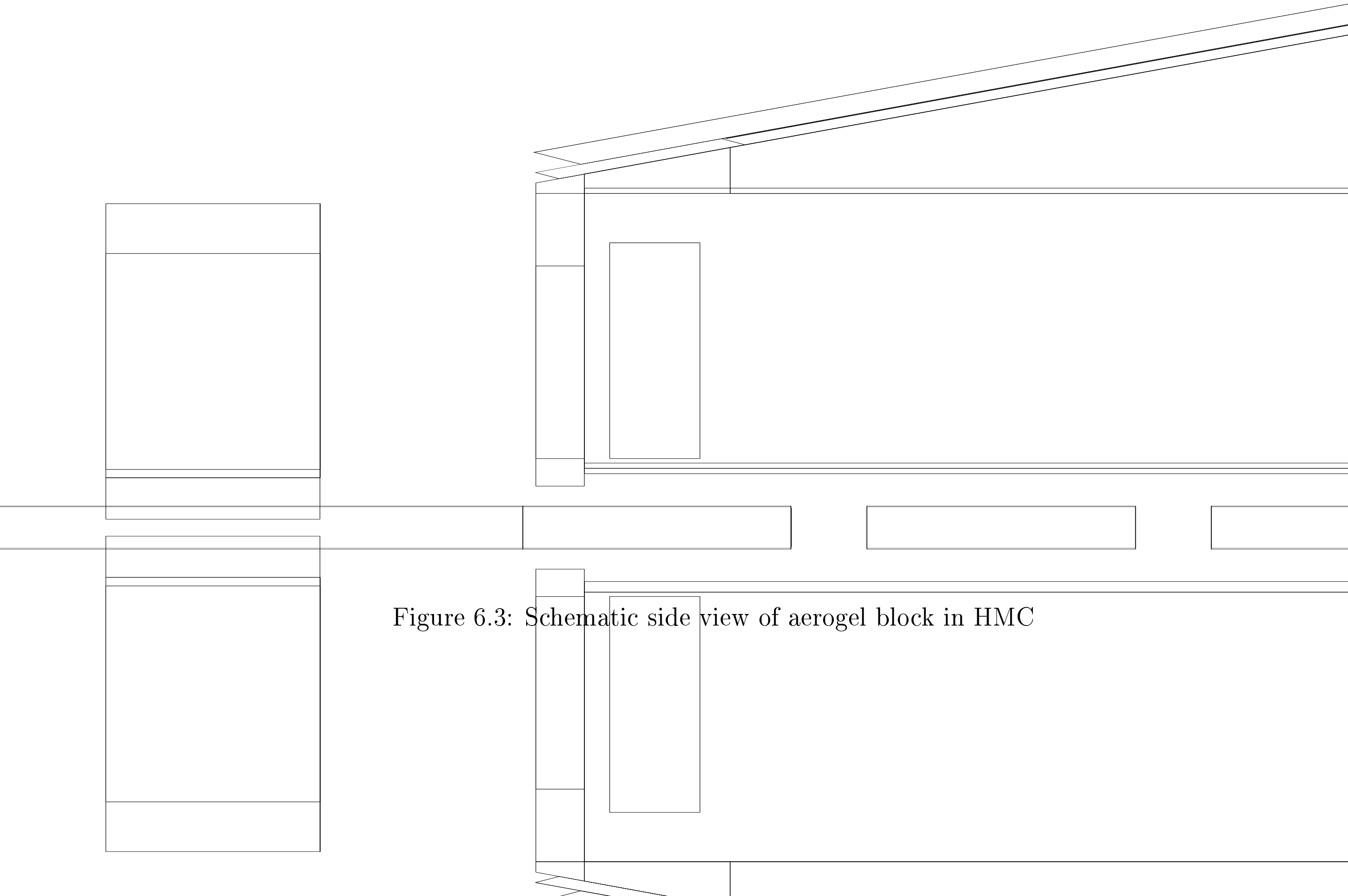

Figure 6.3: Schematic side view of aerogel block in HMC

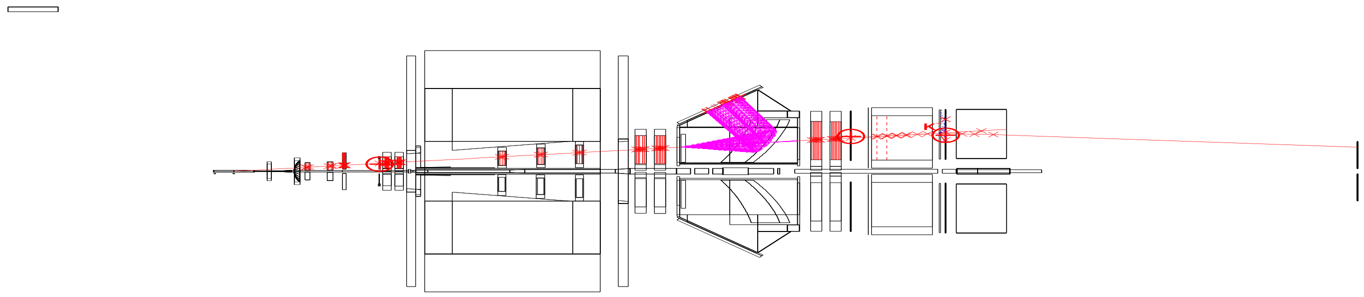

Figure 6.4: Schematic side view of DIS event with aerogel wall

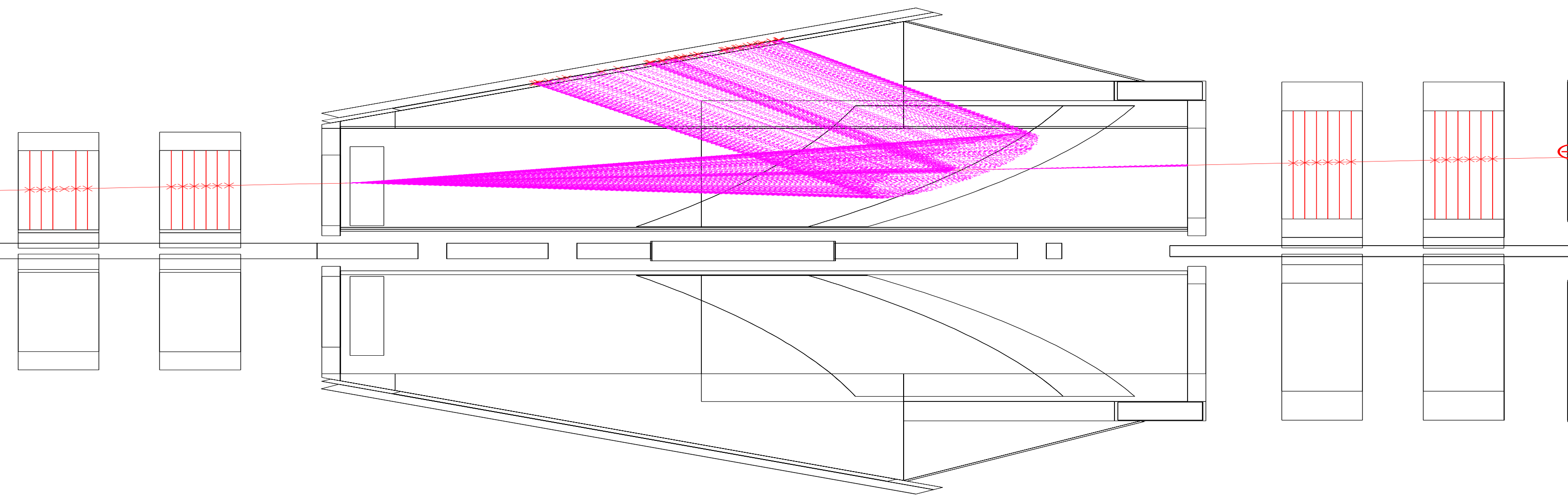

Figure 6.5: Schematic zoomed side view of DIS event with aerogel wall

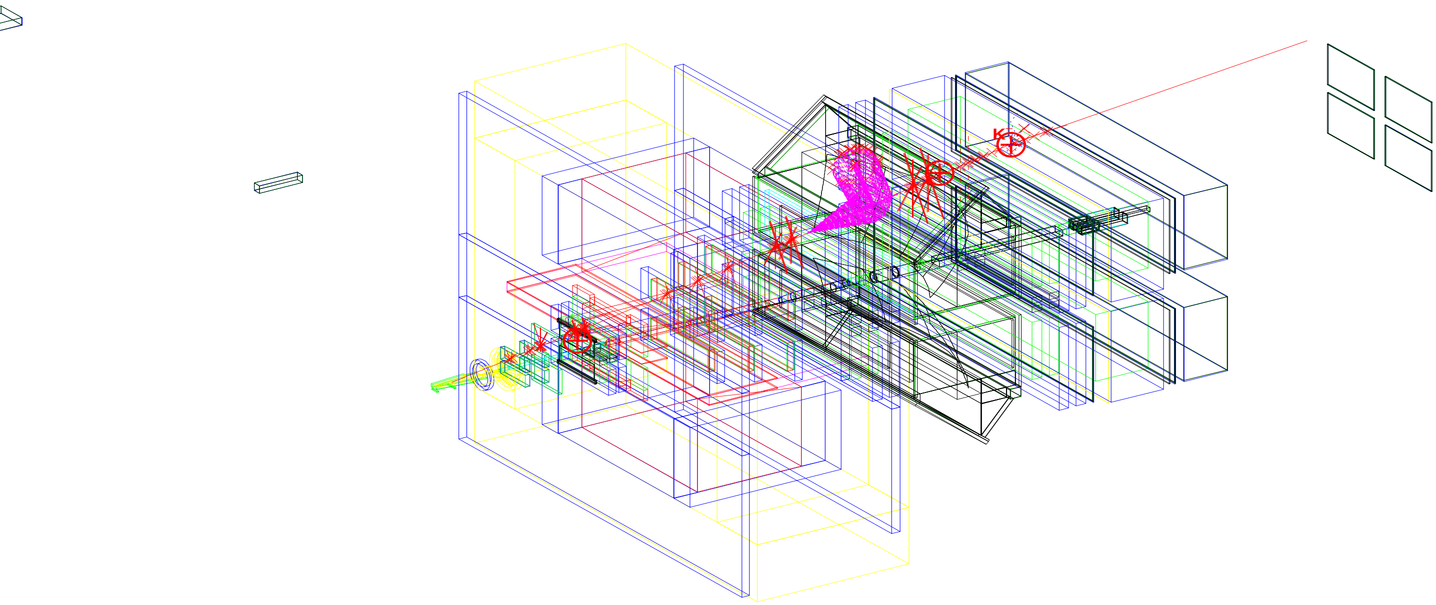

Figure 6.6: Schematic top view of DIS event with aerogel wall

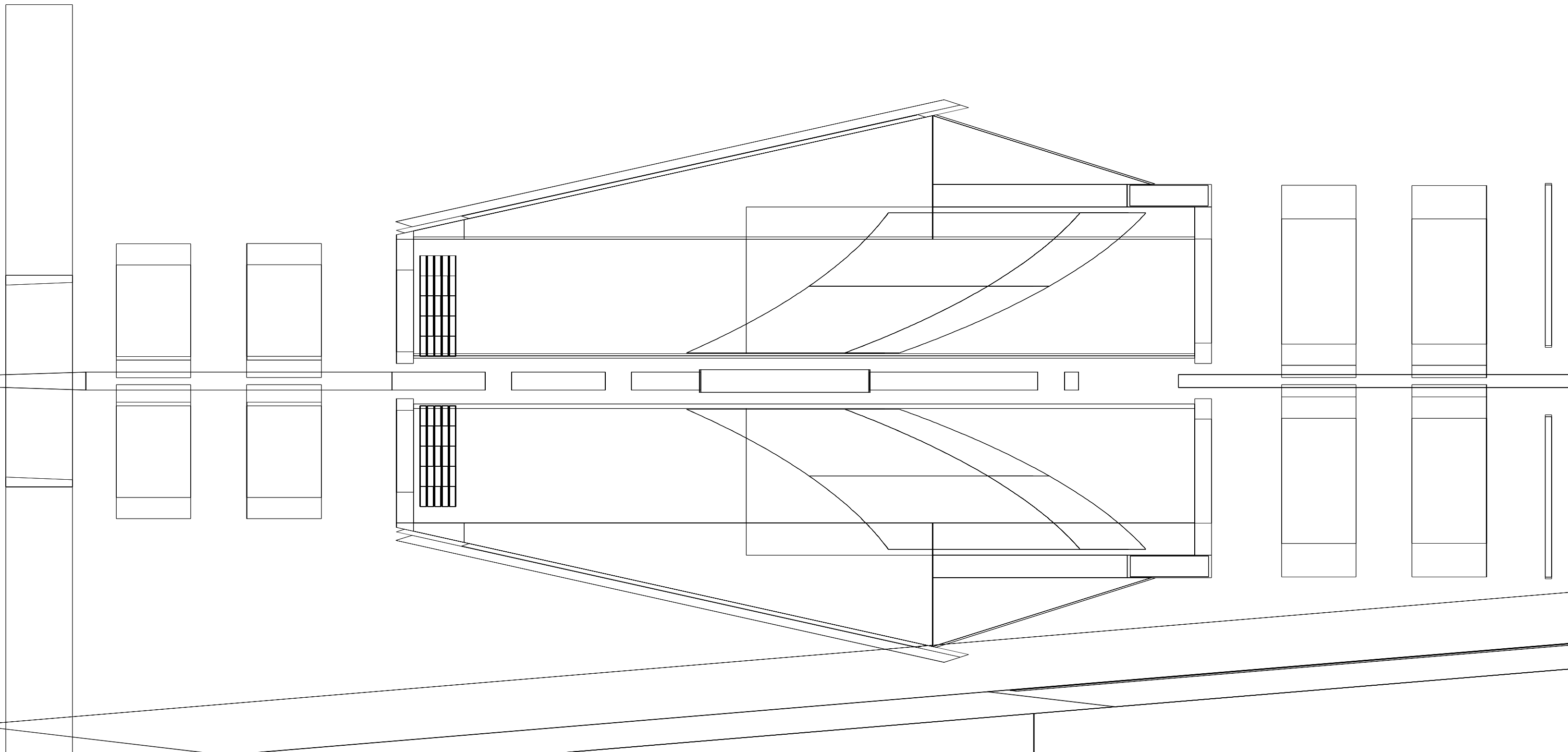

Figure 6.7: Schematic side view of aerogel tiles after the aerogel wall had been updated to aerogle tiles.

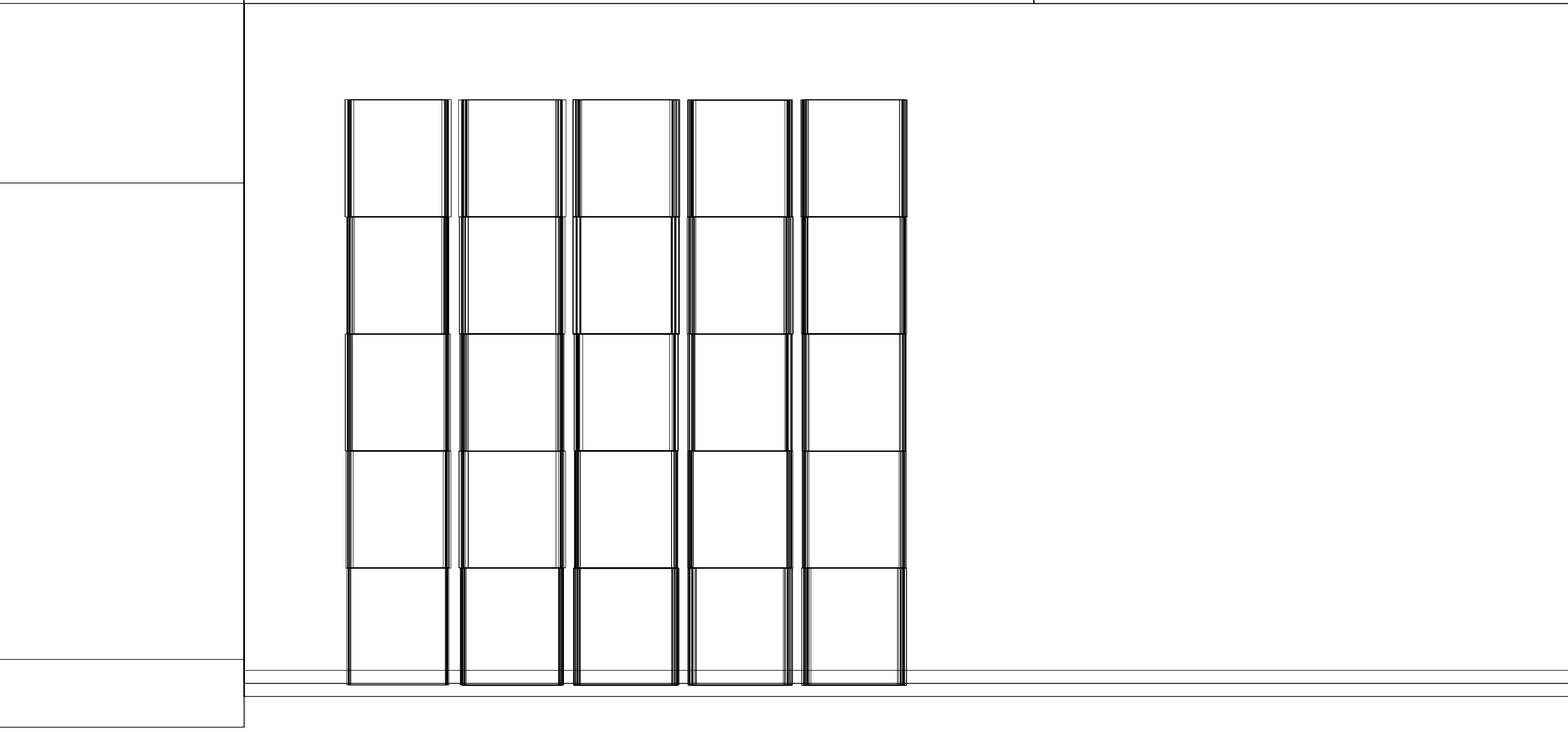

Figure 6.8: Schematic zoomed side view of aerogel tiles after the aerogel wall had been updated to aerogle tiles.

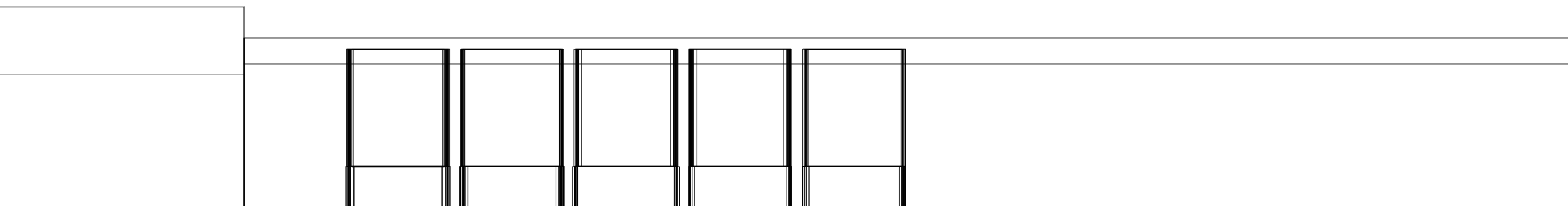

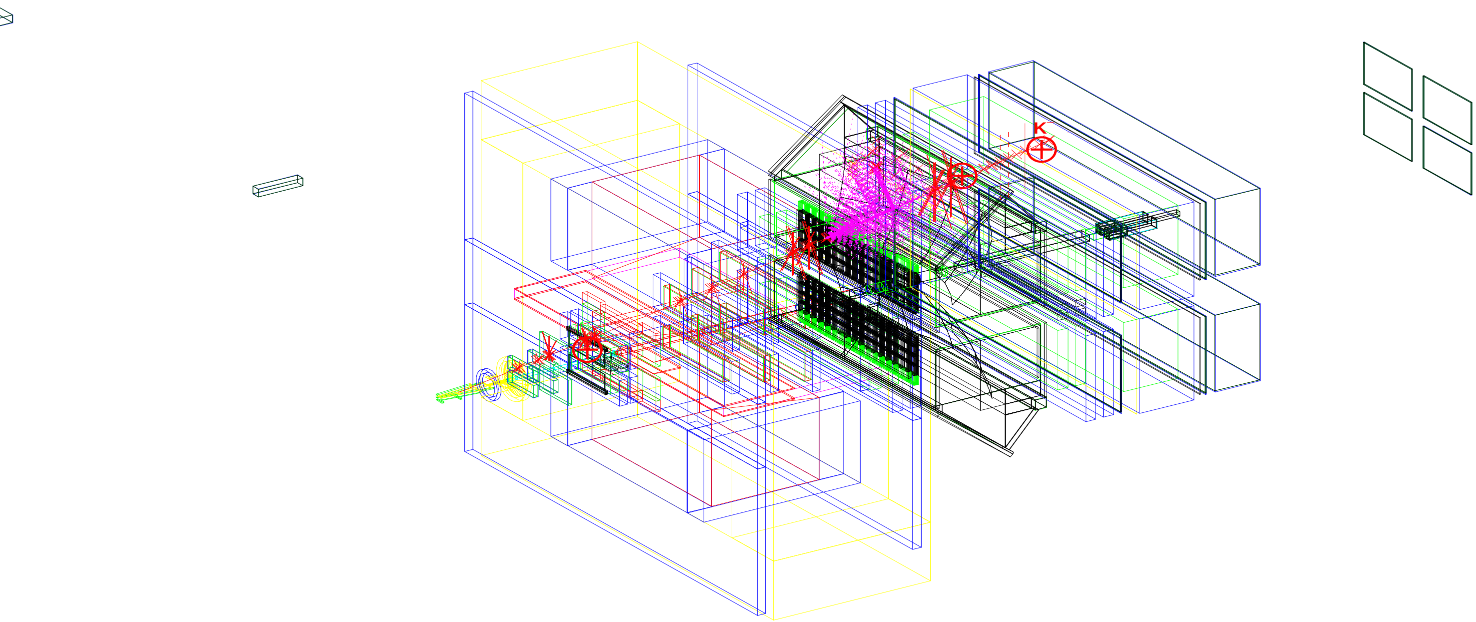

Figure 6.9: Schematic top view of aerogel tiles after the aerogel wall had been updated to aerogle tiles.

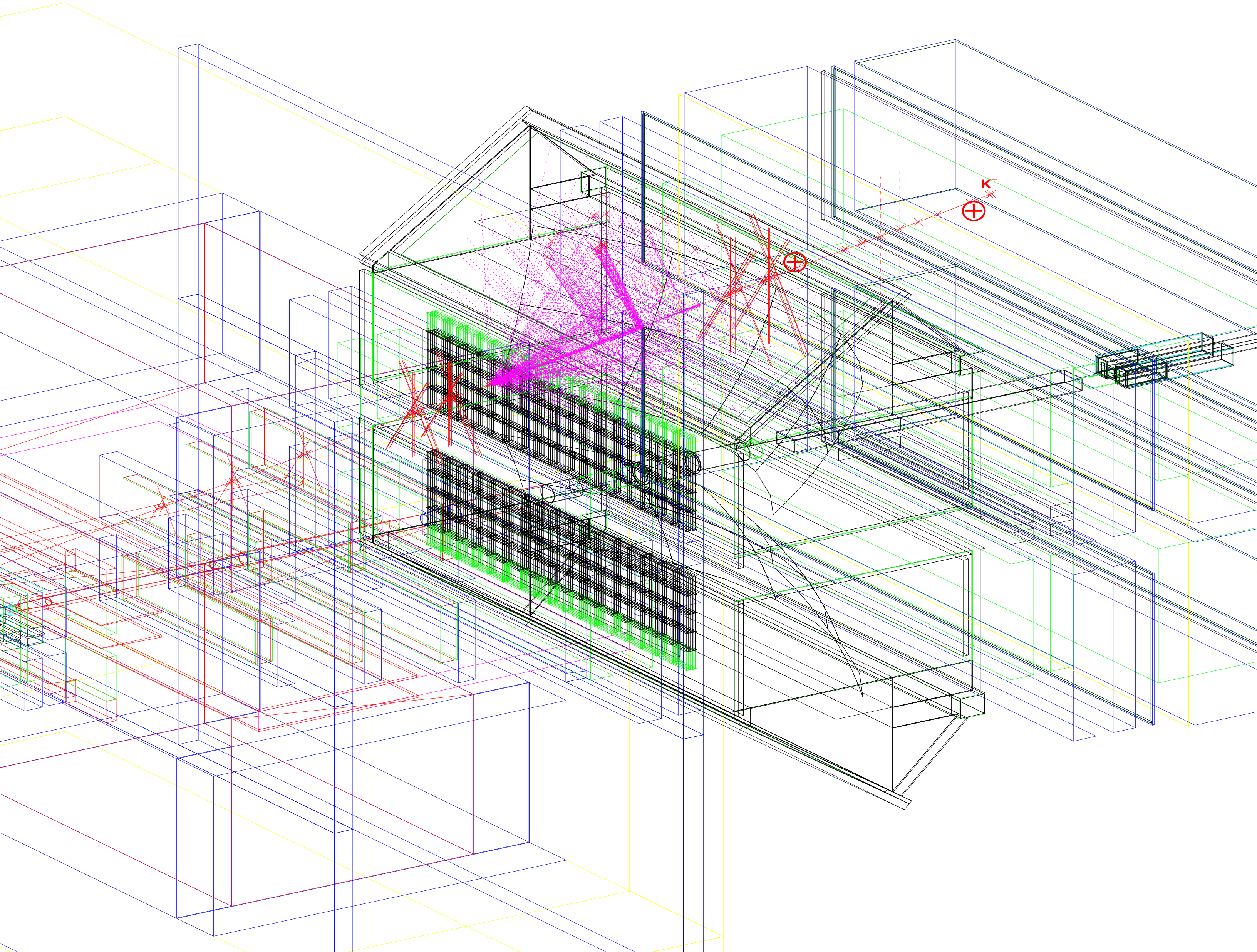

Figure 6.10: Schematic zoomed top view of aerogel tiles after the aerogel wall had been updated to aerogle tiles.

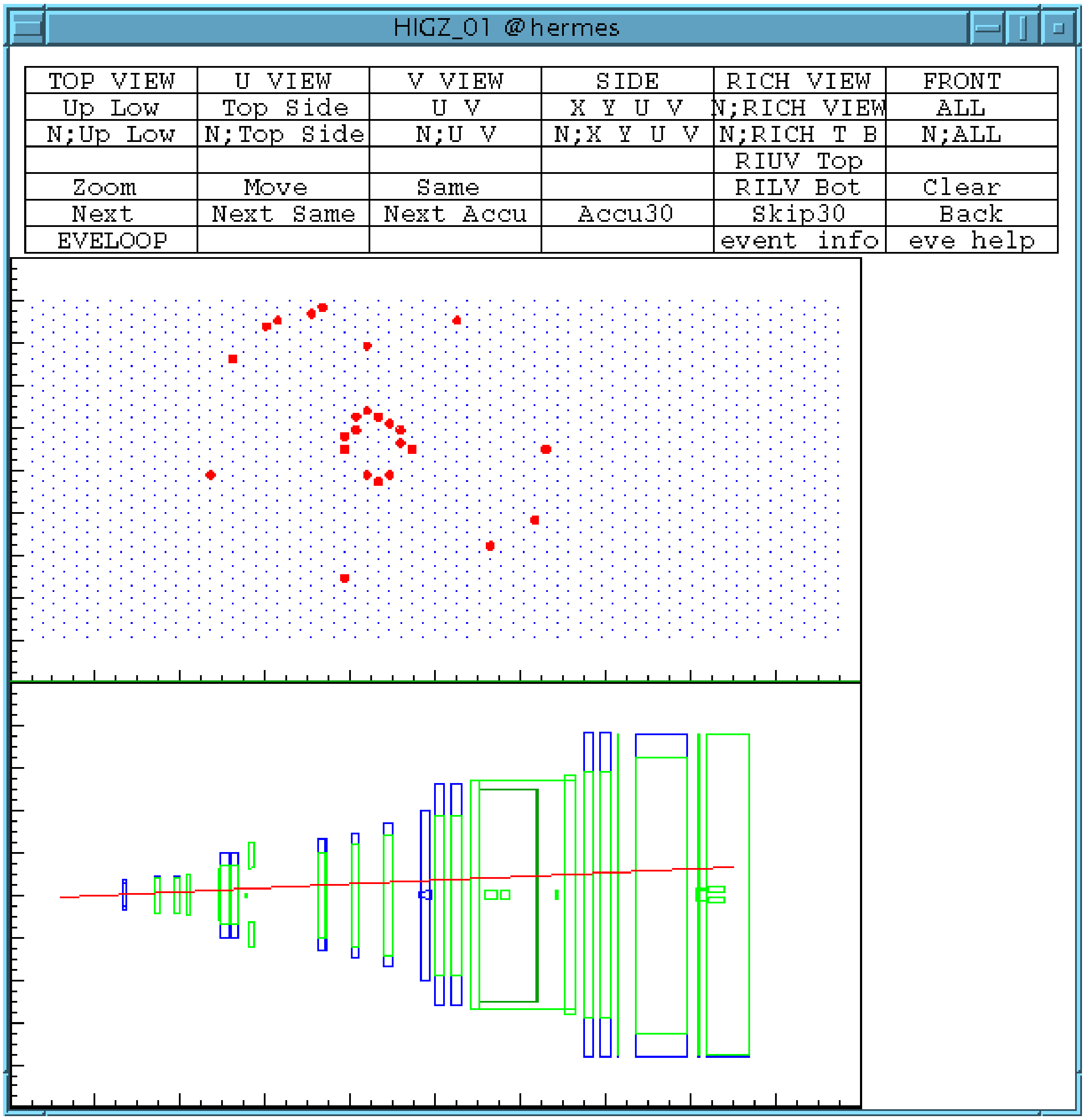

Figure 6.11: Cerenkov Ring of real data from HERMES RICH.

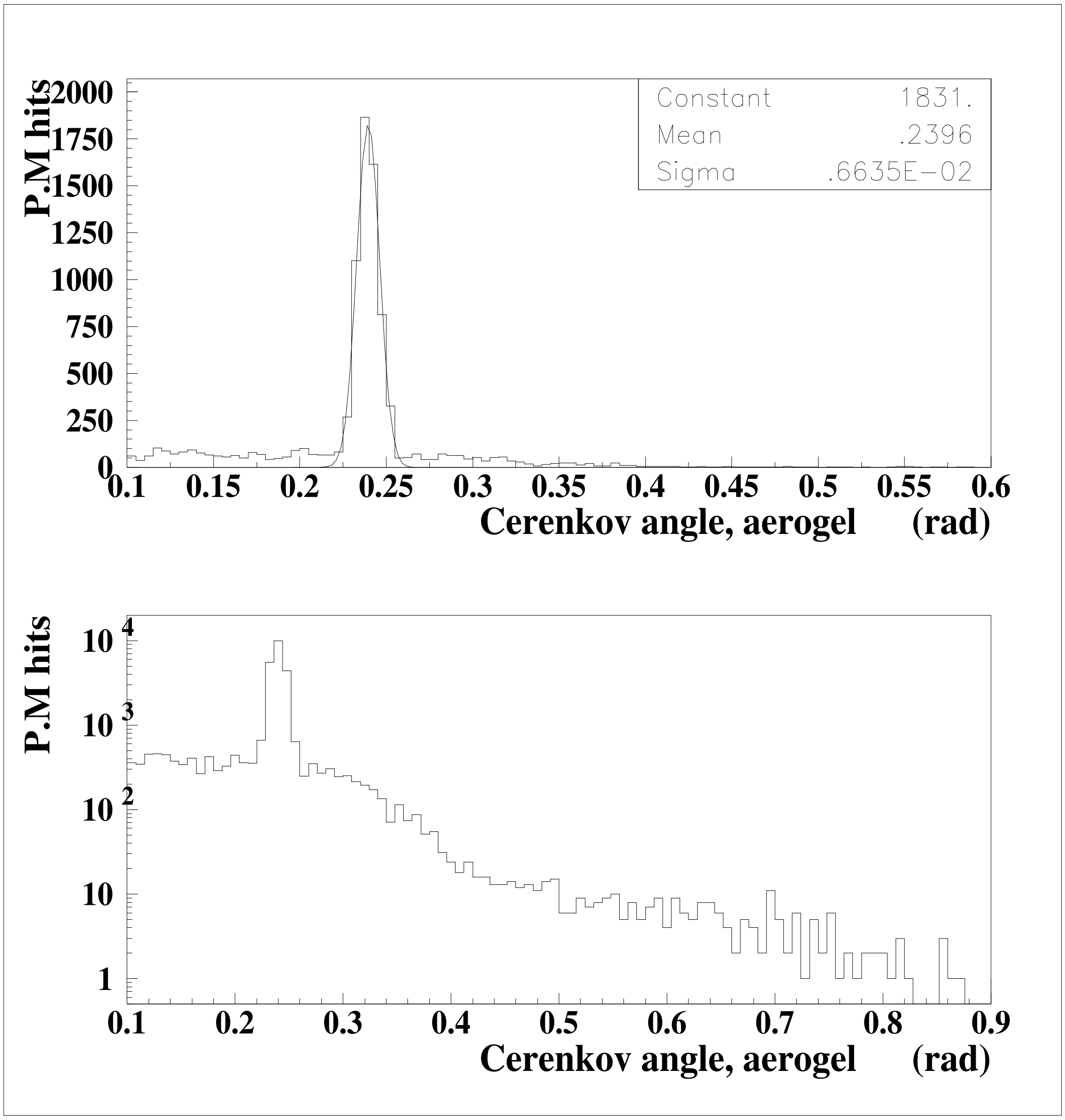

Figure 6.12: Distribution of aerogel angle, by RICH HMC. The upper figure is cut by the aerogel angle from 0.1 to 0.6, while the the lower one is cut by the aerogel angle from 0.1 to 0.9. From the lower one, we can also see the background.

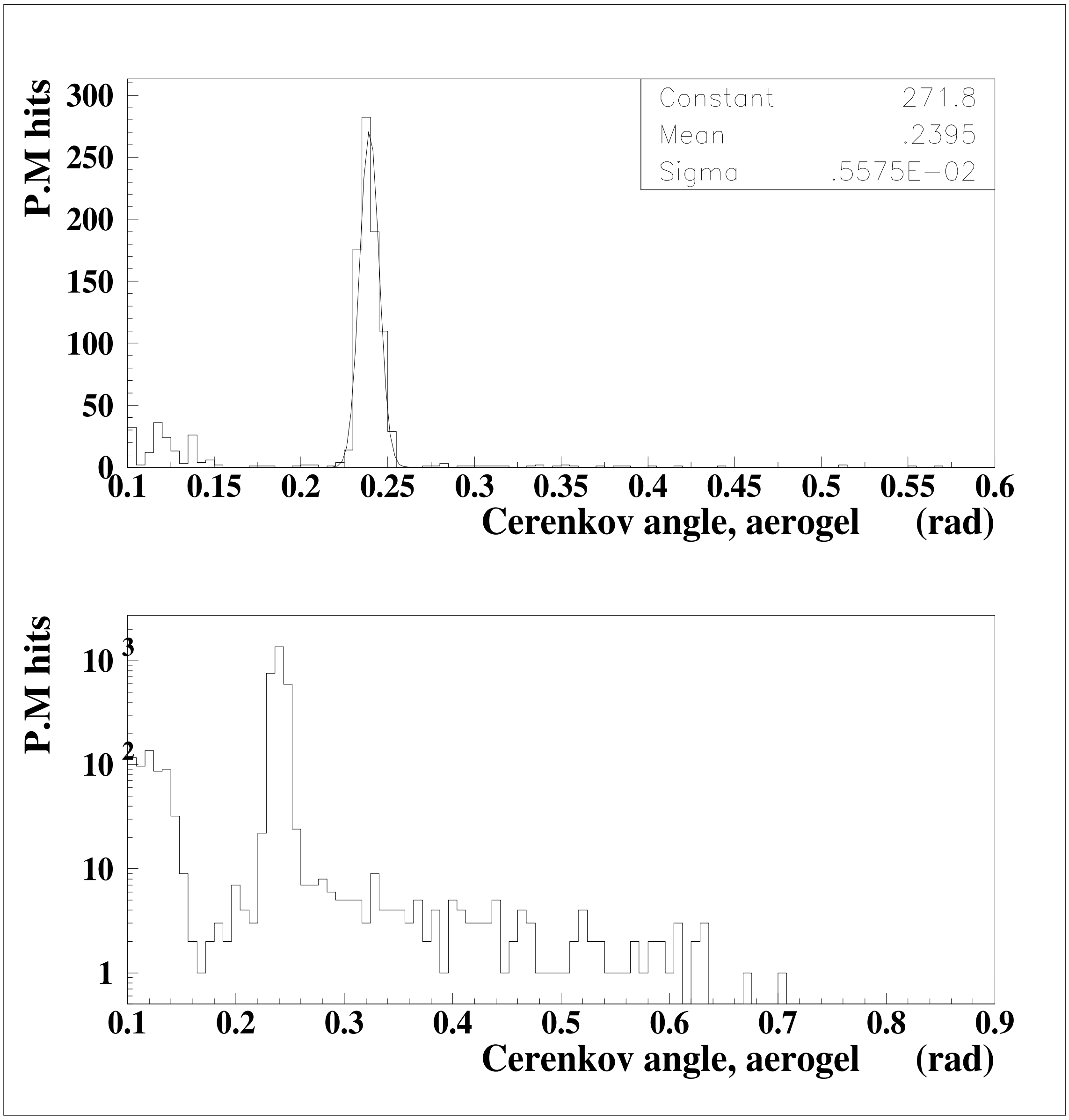

Figure 6.13: Distribution of aerogel angle, by RICH HMC. The upper figure is cut by the aerogel angle from 0.1 to 0.6, while the the lower one is cut by the aerogel angle from 0.1 to 0.9. This figure is also cut by the particle momentum from 10GeV to 12.5 GeV

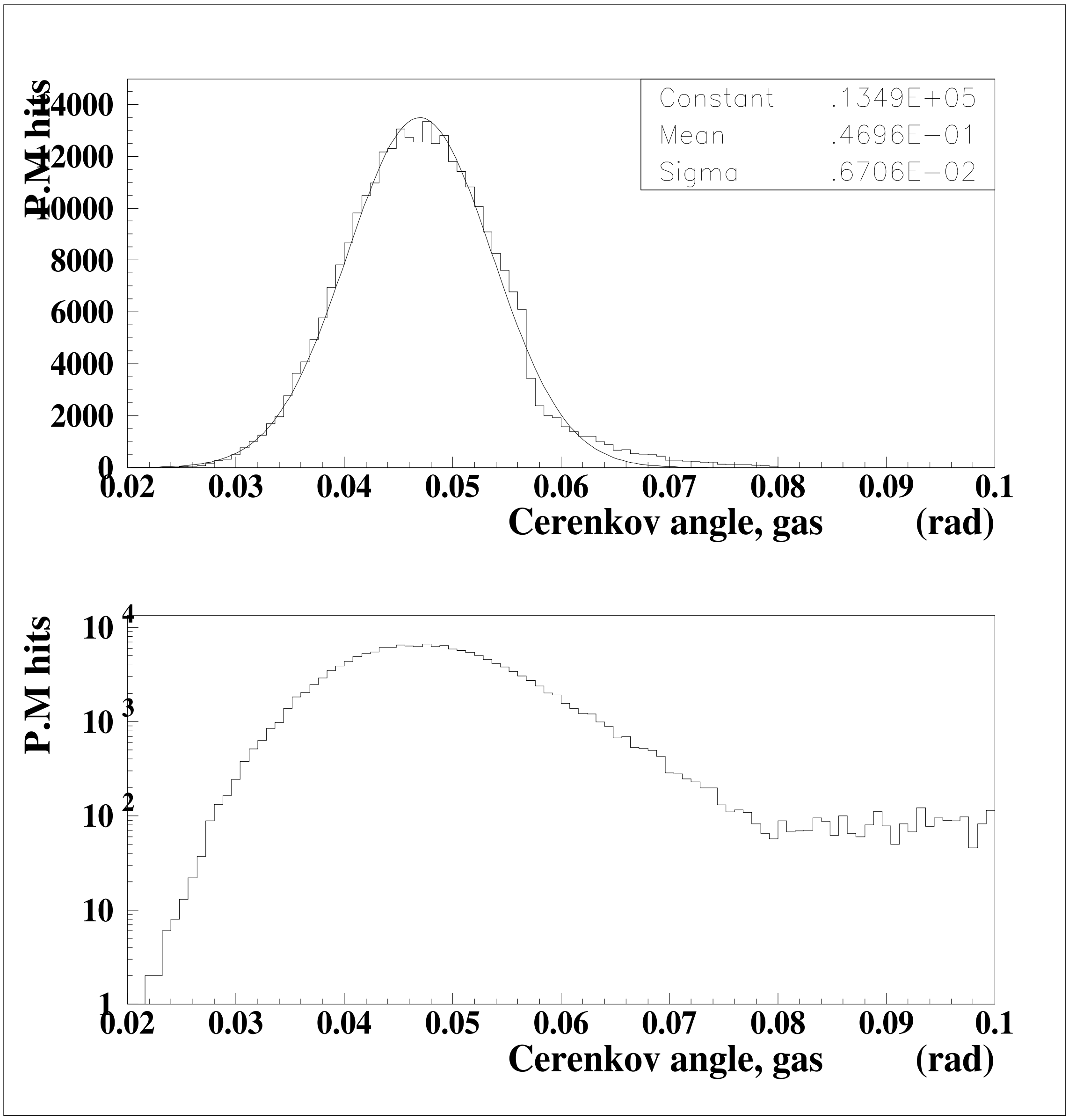

Figure 6.14: Gas angle by RICH HMC

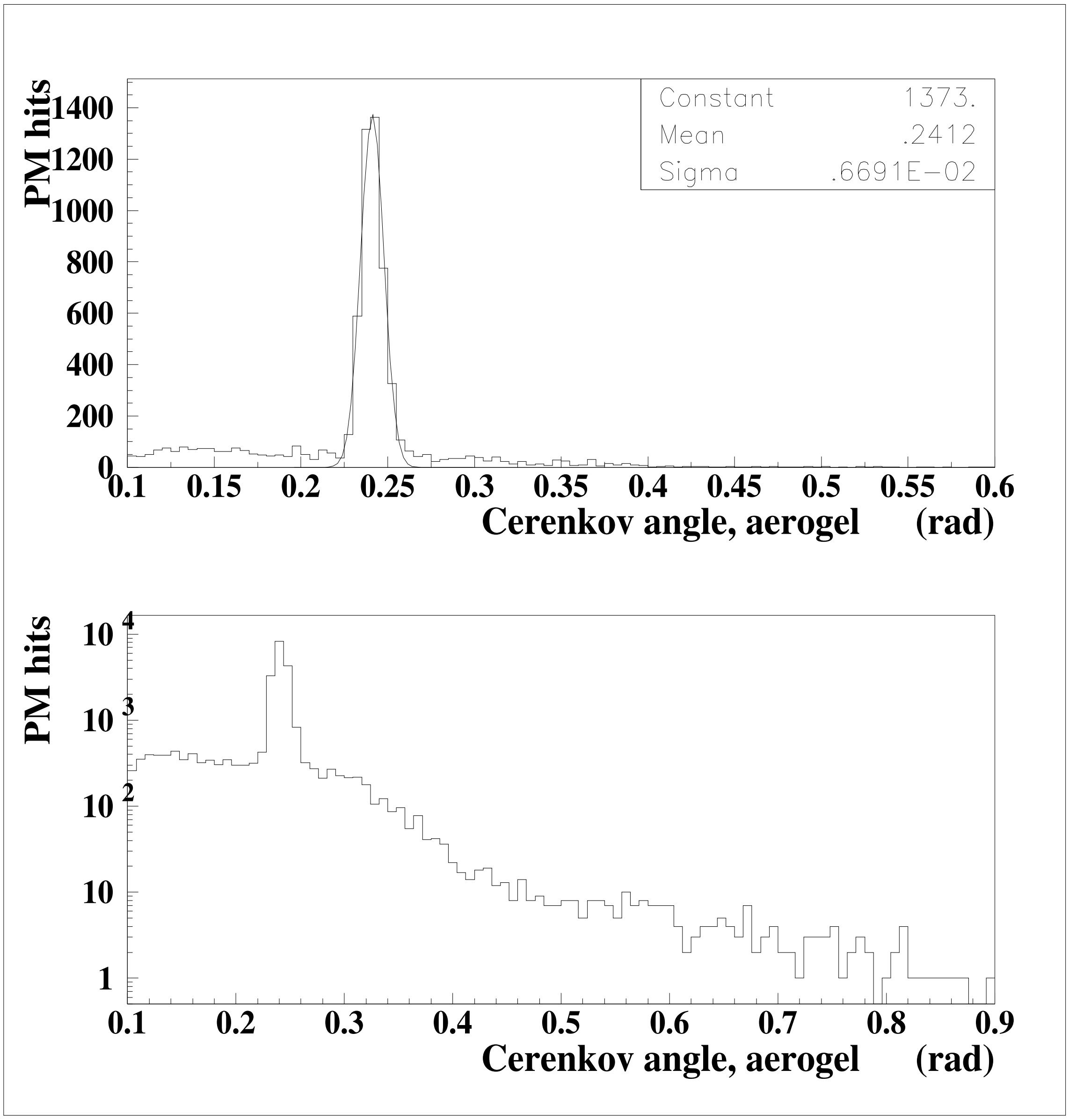

Figure 6.15: Distribution of Aerogel angle, the radiator is aerogel tiles with the same refractive index 1.03, RICH HMC. The upper figure is cut by the aerogel angle from 0.1 to 0.6, while the the lower one is cut by the aerogel angle from 0.1 to 0.9.

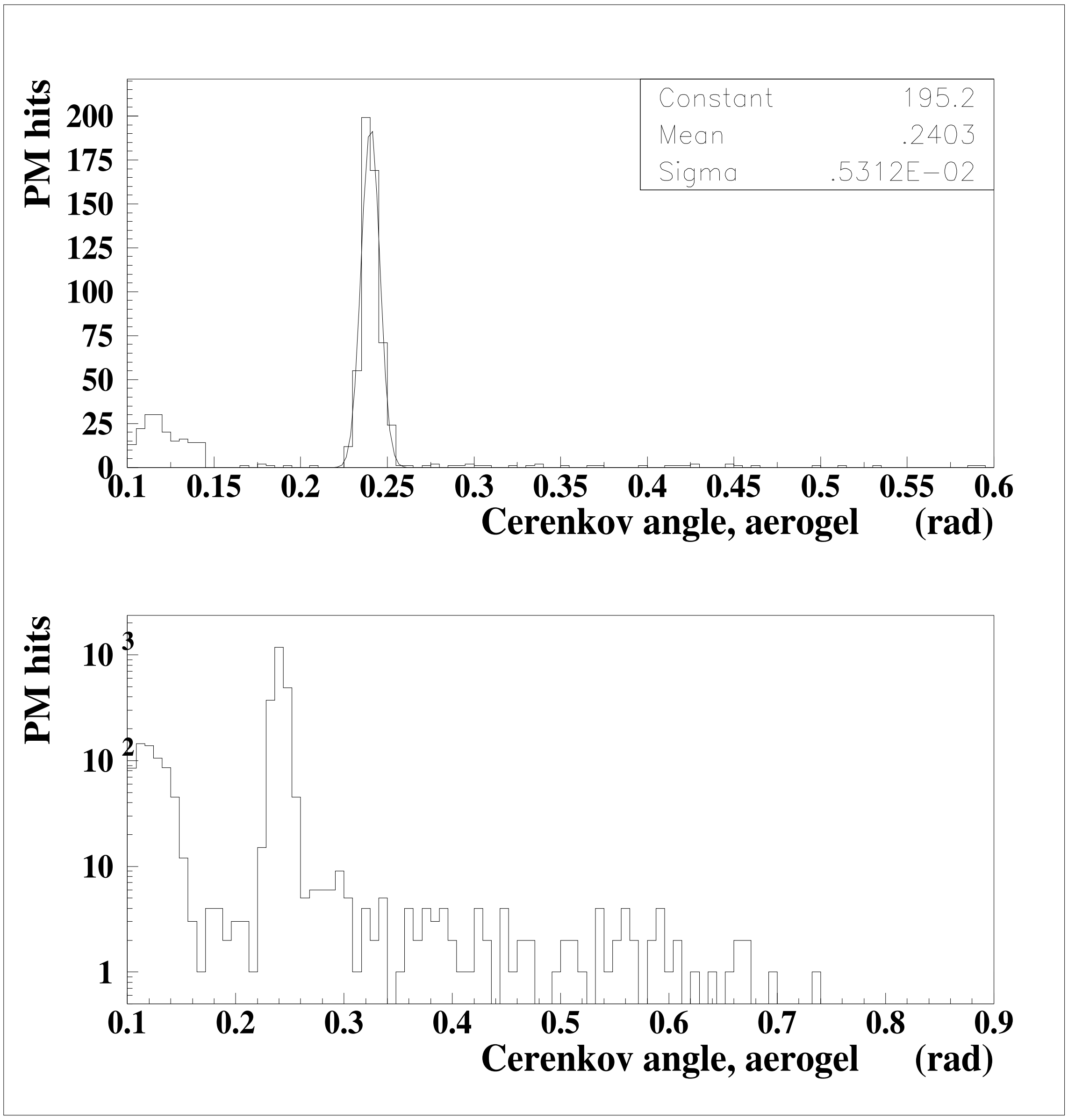

Figure 6.16: Distribution of aerogel angle, the radiator is aerogel tiles with the same refractive index 1.03, RICH HMC. The upper figure is cut by the aerogel angle from 0.1 to 0.6, while the the lower one is cut by the aerogel angle from 0.1 to 0.9. This figure is also cut by the particle momentum from 10GeV to 12.5 GeV

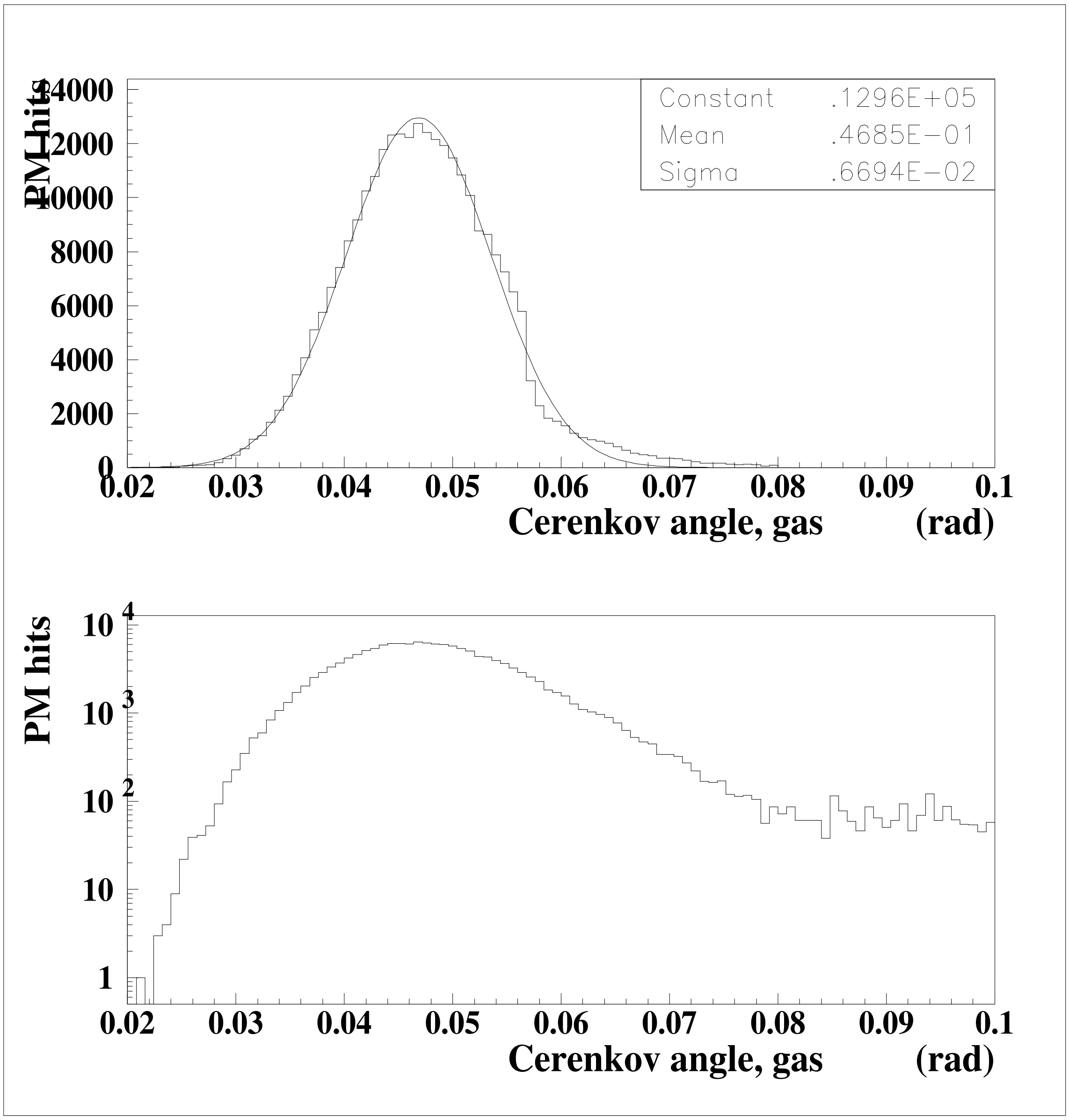

Figure 6.17: Gas angle, tiles with same refractive index, by RICH HMC.

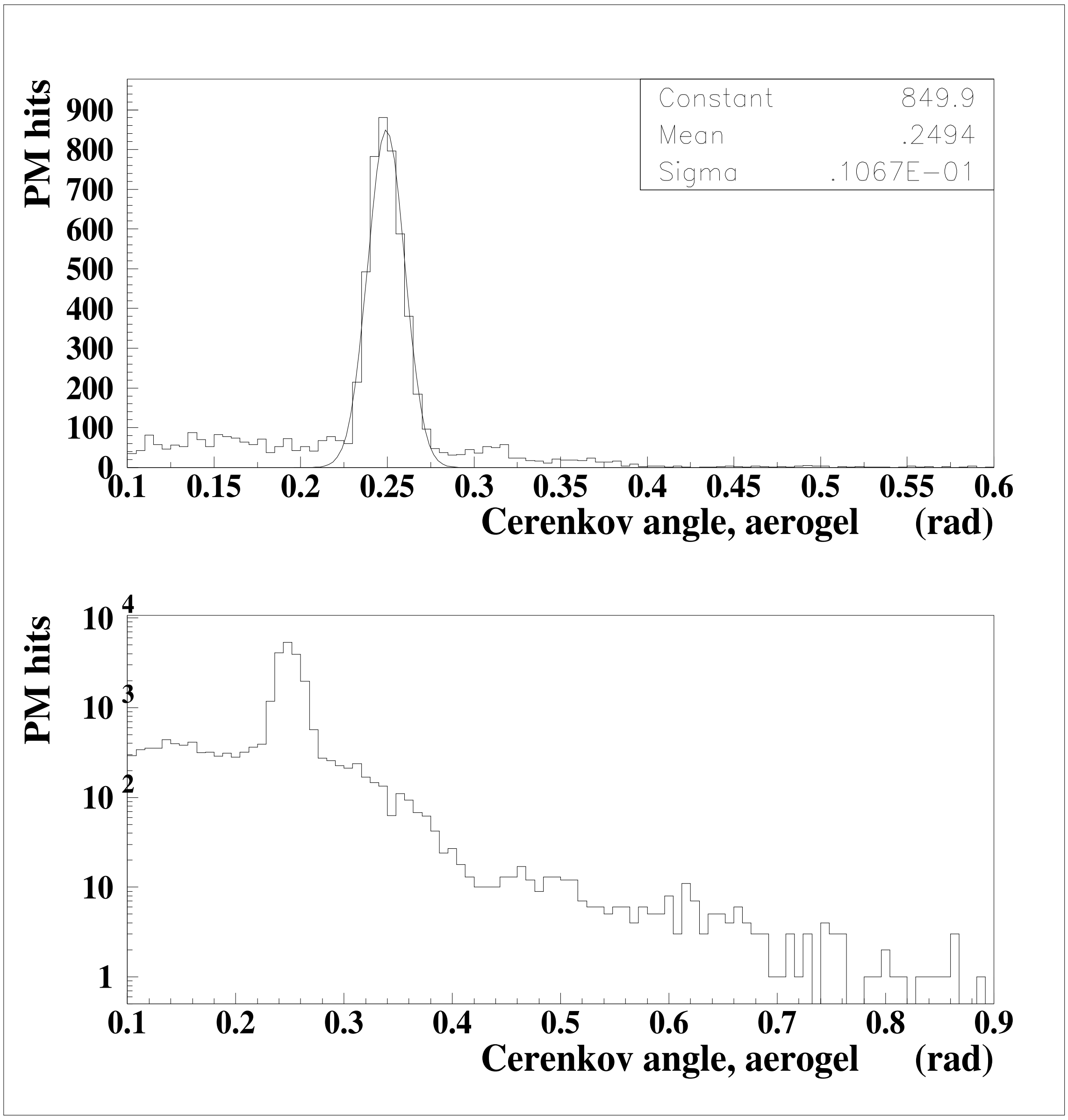

Figure 6.18: Distribution of aerogel angle, the radiator is aerogel tiles with the same refractive index 1.03. Light scattering flag is set to ON, RICH HMC data. The upper figure is cut by the aerogel angle from 0.1 to 0.6, while the the lower one is cut by the aerogel angle from 0.1 to 0.9.

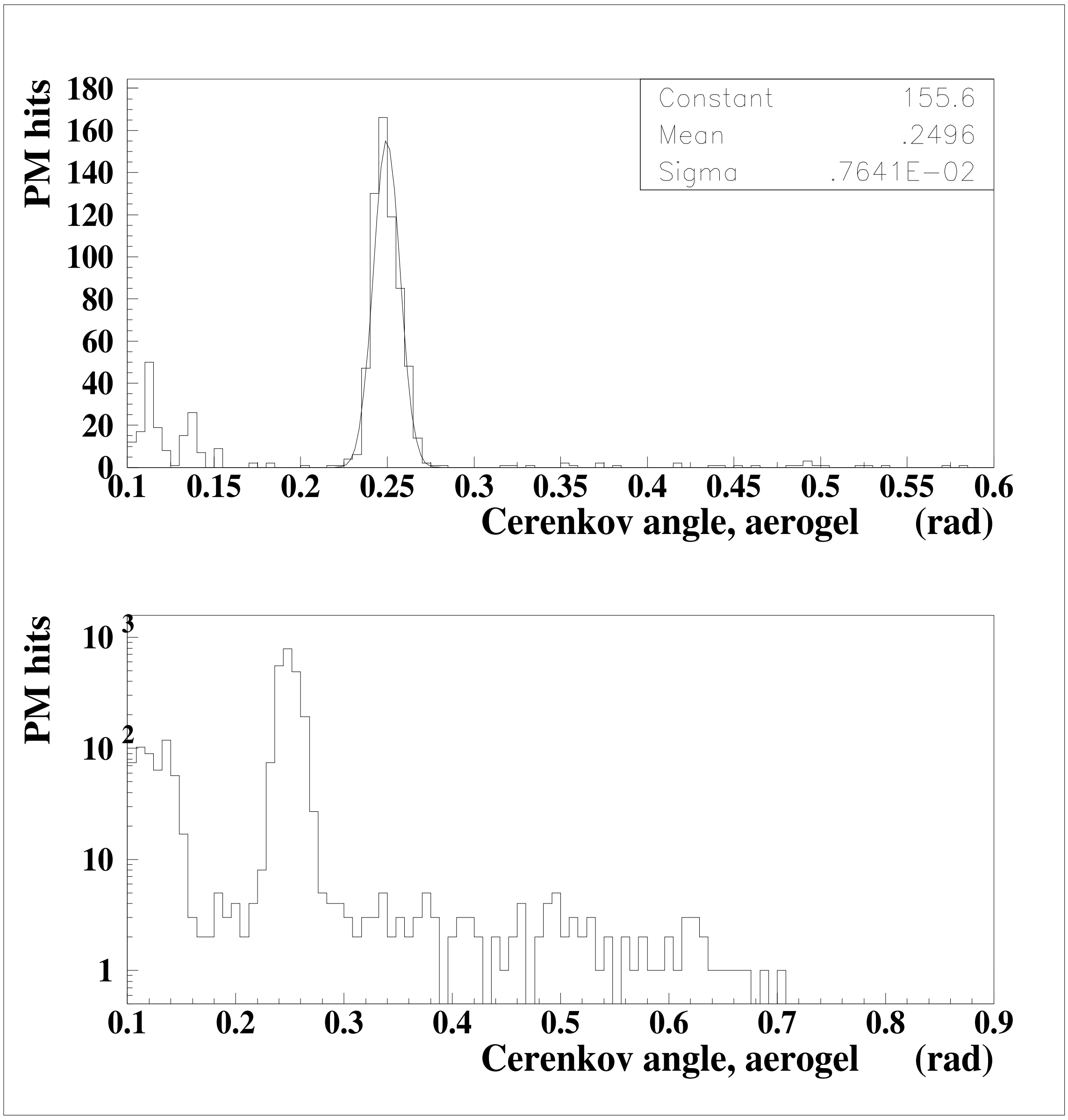

Figure 6.19: Distribution of Aerogel angle, the radiator is Aerogel tiles with the same refractive index 1.03. Light scattering flag is set to ON, RICH HMC. The upper figure is cut by the aerogel angle from 0.1 to 0.6, while the lower one is cut by the aerogel angle from 0.1 to 0.9. This figure is also cut by the particle momentum from 10GeV to 12.5 GeV.

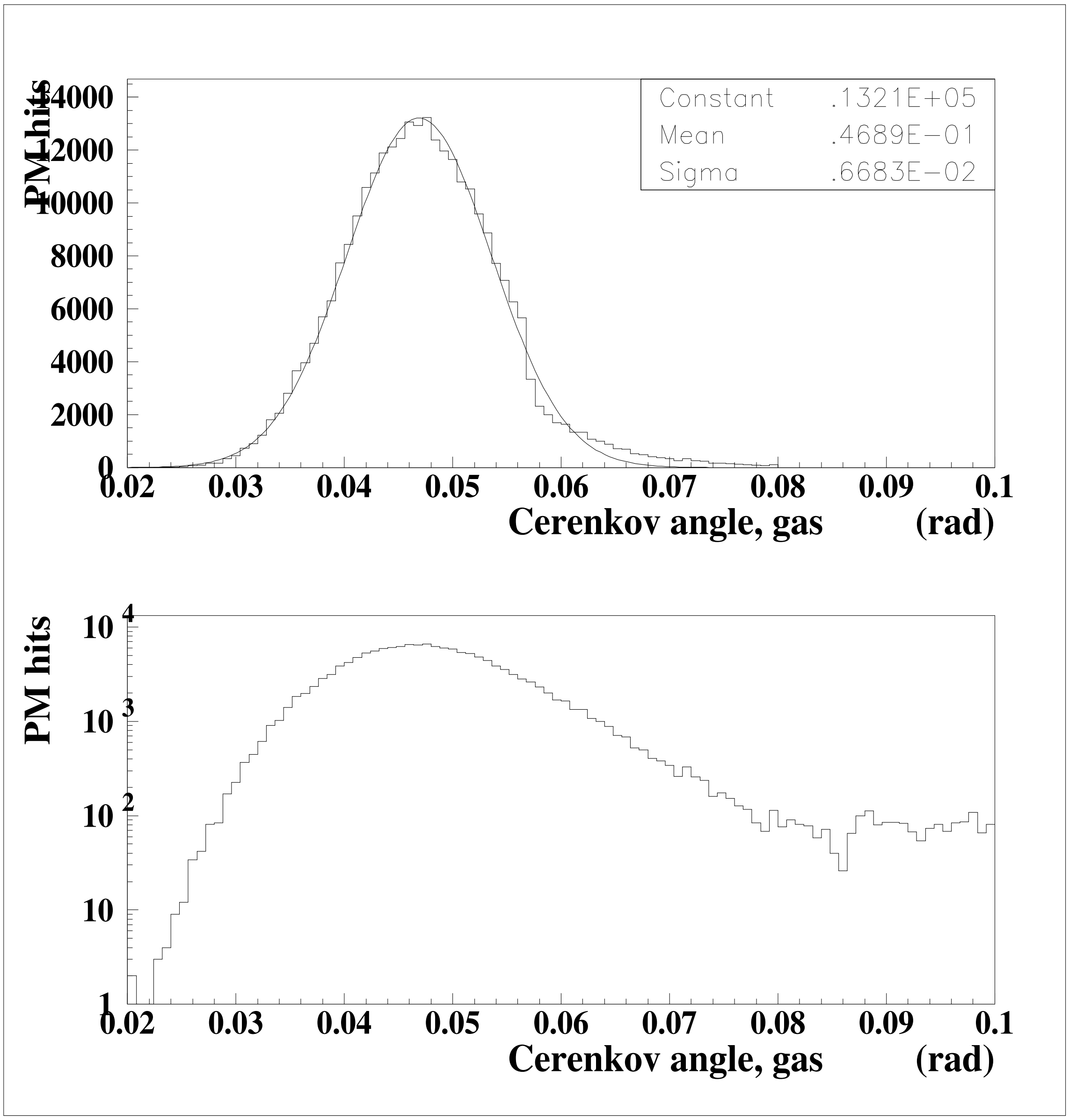

Figure 6.20: Gas ring angle ,same refractive index, light scattering, RICH HMC.

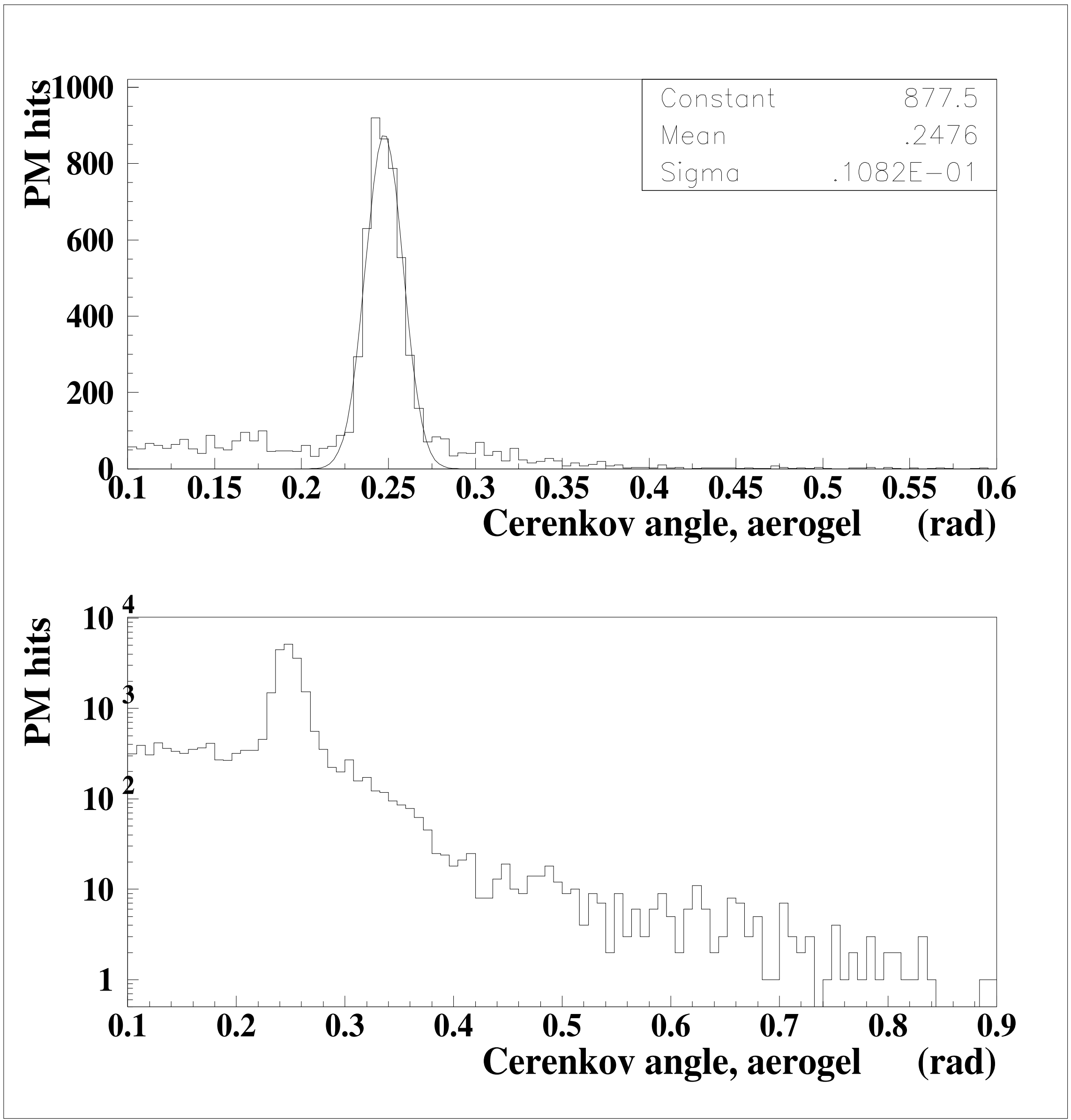

Figure 6.21: Distribution of Aerogel angle, the radiator is Aerogel tiles with real refractive index. Light scattering flag is set to ON , RICH HMC. The upper figure is cut by the aerogel angle from 0.1 to 0.6, while the the lower one is cut by the aerogel angle from 0.1 to 0.9.

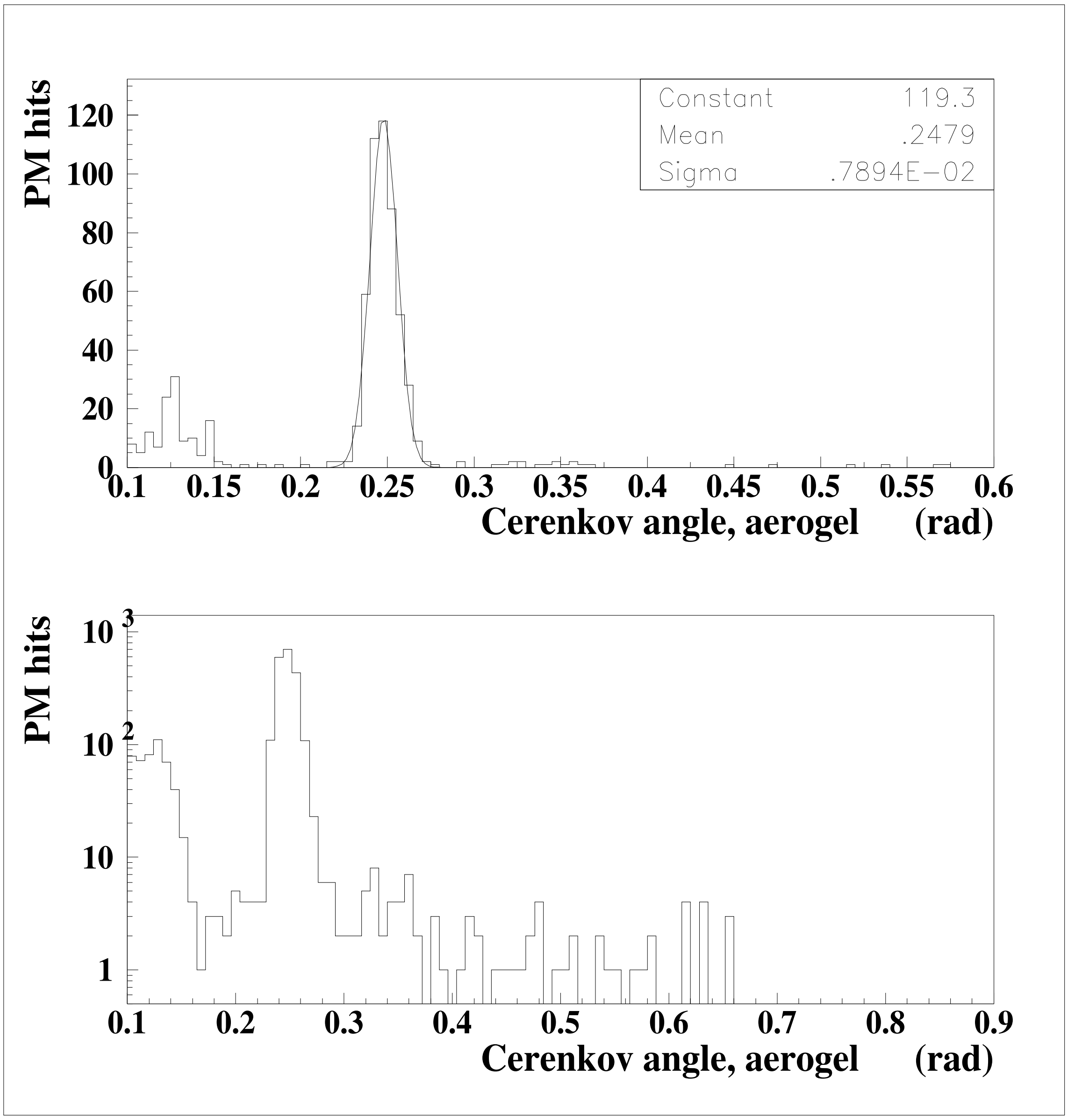

Figure 6.22: Distribution of Aerogel angle, the radiator is Aerogel tiles with real refractive index. Light scattering flag is set to ON, RICH HMC. The upper figure is cut by the aerogel angle from 0.1 to 0.6,while the the lower one is cut by the aerogel angle from 0.1 to 0.9. This figure is also cut by the particle momentum from 10GeV to 12.5 GeV

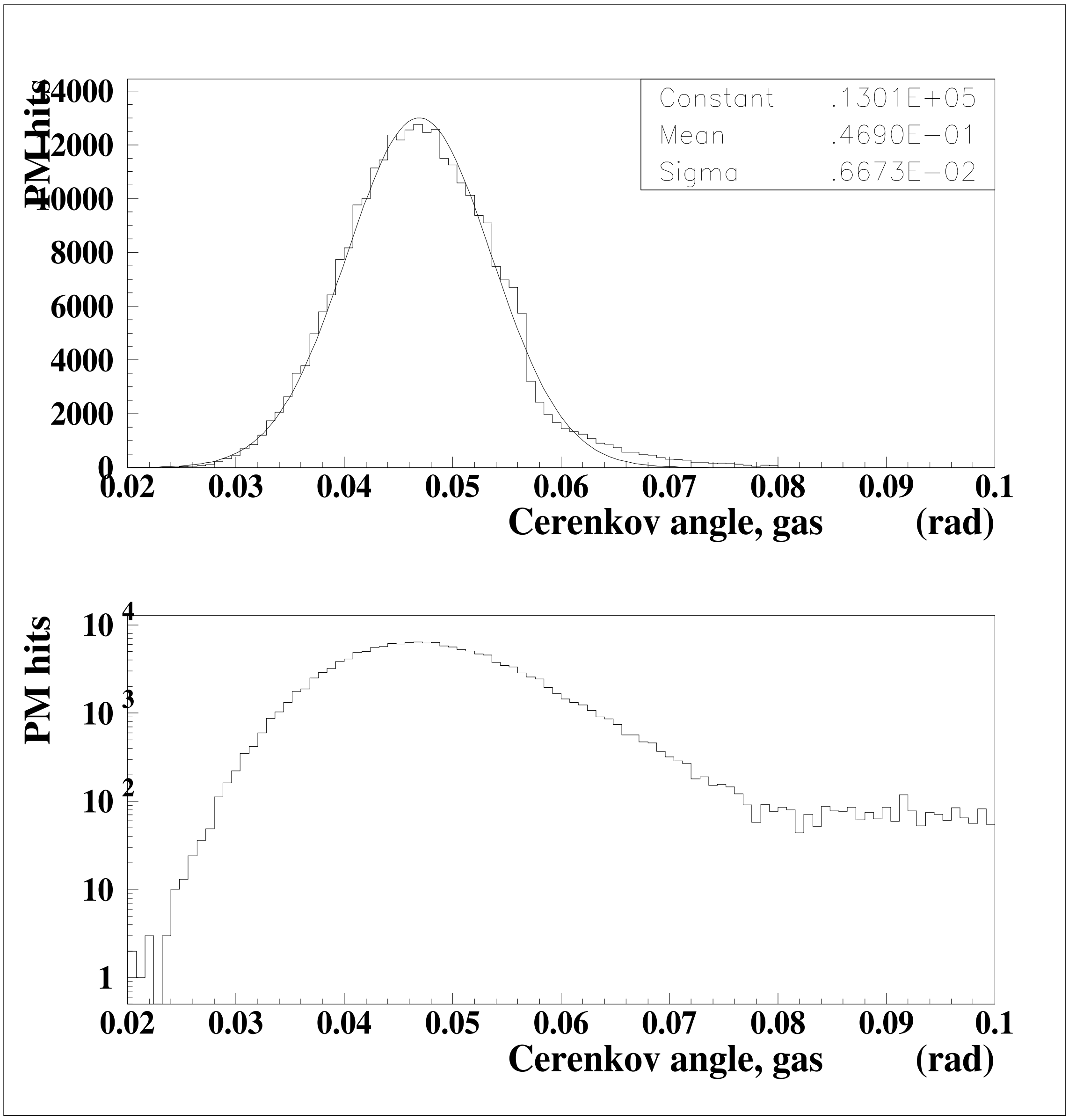

Figure 6.23: Gas ring angle with real refractive index, tefron surroundings and the light scattering flag is set to ON, RICH HMC.

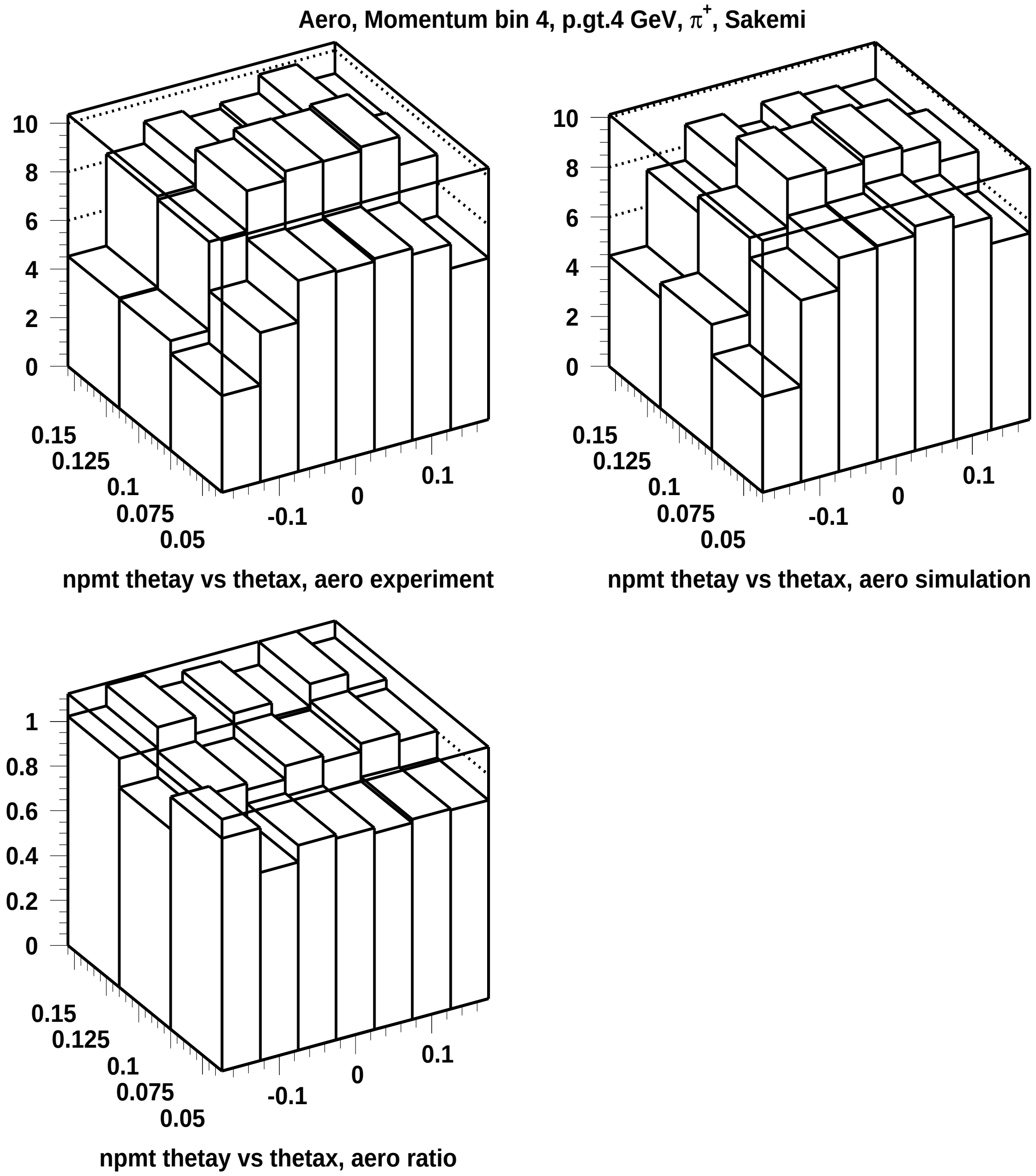

Figure 6.24: Comparison of photo yield of Monte Carlo results with experiment data. The top-left one is the distribution of the experiment photon yield of aerogel vs the scattering angle θ_y and θ_x in HERMES coordinate. The top-right one is the distribution of the Monte Carlo photon yield of aerogel vs the scattering angle θ_y and θ_x. The bottom one is their yield ratio. The particle is π^+. The momentum cut for the plot is $P_\pi \geq 4.0\text{GeV}$

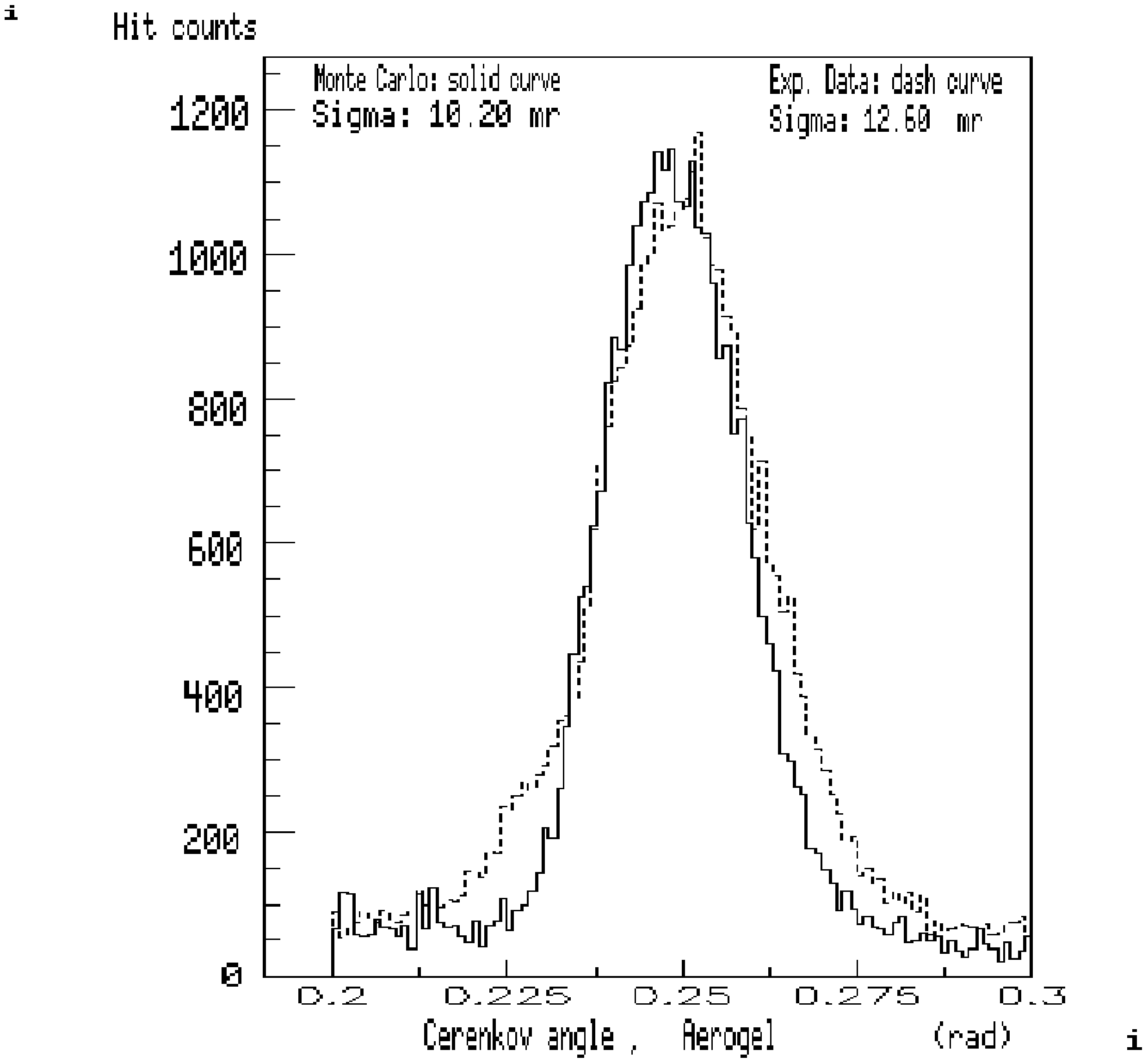

Figure 6.25: Comparison of Monte Carlo results with experiment data

7 Summary

The HERMES experiment was designed to study the spin structure of the nucleon precisely and with a high statistics by inclusive and semi-inclusive measurements of DIS processes. Up to 1997 HERMES used threshold Cerenkov counter, a preshower detector, a transition radiation detector, and a calorimeter to do the particle identification. In the mid of 1998, HERMES converted its threshold Cerenkov counter into a Ring Imaging Cerenkov counter(RICH) which can seperate pion, kaon, proton in all of the HERMES energy region (2GeV to 20Gev). This enables semi-inclusive measurements with very low contaminations due to particle mis-identification.

The Ring Imaging Cerenkov counter of HERMES uses aerogel and C_4F_{10} gas as its radiators. A precise measurement of aerogel properties was carried out and a strict selection of aerogel tiles was done.

In the software, a new program for the RICH detector has been developed. We have successed in including the aerogel tile effects to the HERMES Monte Carlo.

Here are what I have done in my master course:

- I measured refractive index of 1120 pieces of the aerogel tiles and selected 892 pieces for the HERMES RICH.
- I measured the dimensions of all the aerogel tiles as well as tile side reflection and transmission of the light.
- These aerogel tiles were sent to HERMES and have been installed in the new Cerenkov detector.
- I have simulated the new RICH system by Monte Carlo. The Monte Carlo gives a single photon resolution of Cerenkov emission angle about 11mr for the aerogel radiator and 7.5mr for the gas radiator.

It is the first time to use aerogel radiator in the Ring Imaging Cerenkov Counter. The new detector was put into operation, and is successfully taking data since 1998.

Acknowledgements

I would like to thank Professor T.-A. Shibata for giving me a lot of helpful advices and hints, and always best feedback during all the processes of hardware setup such as measurement of aerogel properties. He also helped me in software field for including aerogel effects into the Monte Carlo, comparing with experiment data and other physics discussions etc. All his kindness, physics idea and international sense made me feel my stay in Shibata Lab. of Tokyo Institute of Technology the greatest time beyond the language and culture difference.

I would also like to express my special thanks to Dr. Y. Sakemi for helping me a lot in the long working days. I enjoyed very much in analyzing experimental results, debugging programs and maintaining Laser Alignment System with him either in our office room or in the experiment hall.

I would also like to thank J. Kanesaka, K. Suetsugu, F. Sato who worked with me in the measurement and in the Monte Carlo studies. I was moved by their kindness and cooperation. Furthermore, I learned a lot of Japanese phrases from them.

I would also like to thank the following people:
E.C. Aschenauer(DESY), S. Giani(CERN), T. Harano, T. Ishiwatari, M. Iwasaki, R. Kaiser(DESY), M. Kawamura, H. Kobayashi, T .Sakuma, T. Sumiyoshi(KEK), E. Taniguchi, E. Volk(DESY), H. Yokoyama(Matsushita Electric Works), S. Yoneyama and also other HERMES members who gave me helpful advices.

Bibliography

[EMC88] J. Ashman *et al.* European Collaboration(EMC), 'A Measurement of the Spin Asymetry and Determination of the Structure Function g_1 in Deep Inelastic Muon-Proton Scattering' Phys. Lett. B206(1988) 364

[RICH97] E. Cisbani *et al.* 'Proposal for a Dual Radiator RICH for HERMES' HERMES Internal Note 97-003, January 1997

[TYps94] T. Ypsilantis, J. Seguiot, 'Theory of Ring Imaging Cerenkov counters' Nuclear Instruments and Methods in Physics Research A 343 1994 30-51

[Yoko95] H. Yokogawa, M. Yokoyama, 'Hydrophobic Silica Aerogel' Journal of Non-Crystalline Solids 186(1995)23

[Adachi95] I. Adachi *et al.*, Nucl. Instr. and Meth. A 355 (1995) 390

[Sumi97] T. Sumiyoshi, 'Aerogel Cerenkov Counter', KEK Phys. Dep. Seminar(1997)

[Kane98] J. Kanesaka, L.f. Zhang, Y. Sakemi, K. Suetsugu, F. Sato, and T.-A. Shibata, 'Measurements of the Properties of Silica Aerogel Tiles for HERMES RICH' HERMES Report 98-061 (1998)

[Ralf98] Ralf Kaiser, Dirk De Schepper, 'Particle Identification with the Hermes RICH Detector, Description of the Different Approaches' HERMES Report Note 98-008 (1998)

[NSAK93] N. Sakai,
'Particle Physics', BAIFUKAN(1993)

[KATO94] S. Kato
'Radiation Detection', BAIFUKAN(1994)

[Deleo97] R. De Leo, etc.,
'Electronic detection of focused Cerenkov rings from aerogel'
Nuclear Instruments and Methods in Physics Research A 401 (1997) 187-205

[GEANT93] CERN Program Library Office
GEANT, Detector Description and Simulation Tool
CERN Program Library Long Writeup W5013(1993)

[Cart98] P. Carter,
'The Aerogel Radiator of the HERMES RICH'
proceedings of RICH98 (1998)

[Car98] P. Carter,B.Fillipone,
'Caltech Studies of HERMES RICH Aerogel'
HERMES Report(1998)

[Dele98] R.De Leo, L.Lagamba, E.Nappi, C.Coluzza,
'Optical characterization of n=1.03 aerogel from Matsushita'
HERMES Report(1998)